# A Study on
# Wheeled Inverted Pendulum Robots
# Capable of Climbing Stairs

（階段を昇降できる車輪型倒立振子ロボットに関する研究）

by

Ananta Adhi Wardana

Graduate School of Engineering
Hiroshima University
September, 2020

# Contents

# List of Figures

# List of Tables

# Chapter 1

# Introduction

This chapter explains the problems associated with the mobility of the robot in a human environment. Firstly, the discussion mainly consists of related works on some robots designed to work with human and the method on how the robots can deal with some features that commonly exists in a human environment such as narrow passages, desks, and uneven terrains. Secondly, this chapter discusses some recent developments of inverted pendulum robots, both two-wheeled and single-wheeled, and their potential to be employed in a human environment.

## 1.1 Background

Recently, there is a growing interest in the development of robots that can operate alongside people. This is because most of the robots cannot appropriately work in a human environment. Responding to the human environment is an essential ability for a robot to operate alongside people. This includes climbing stairs unassisted, moving through a congested area, and reaching the top of the desk, as shown in Figure 1.1. Numerous studies have investigated robot mobility to address stairs and narrow passage issues. Multiped walking robots [1, 2, 3, 4], wheel-leg robots [5]-[8], crawler-type rescue robots [9], transformable tracked robots [10, 11], hopping robots [12, 13, 14], and others [15, 16, 17] can traverse narrow passages and stairs. However, most robots have a short structure and thus they cannot reach objects that are typically located on desks.

Humanoid robots are considered ideal for operating in a human environment [18,

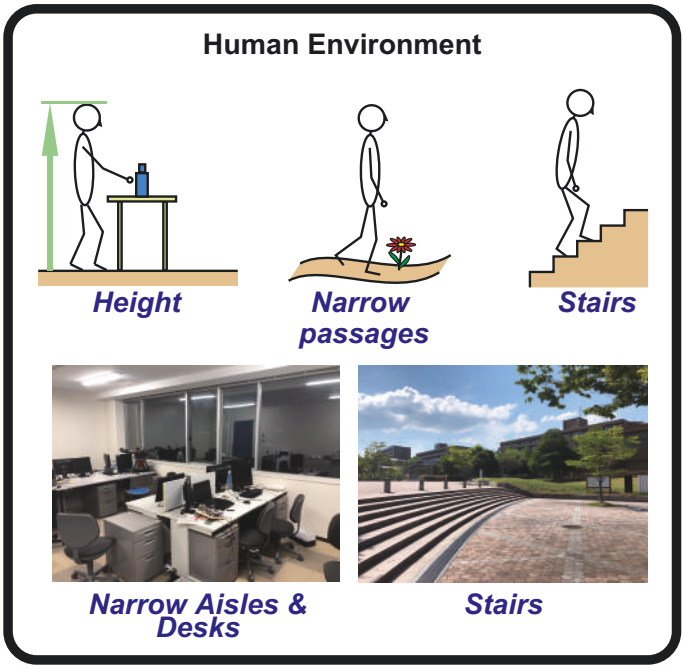


**Figure 1.1: Essential abilities for the robot to move in human environment.**

19, 20]. Humanoid robots can effectively traverse stairs, just like humans, by utilizing biped legs [21, 22] and can also move through narrow passages because they are built to resemble the human physiology. Their legs can provide stability on pitch and roll axes, and therefore, they can move stably across inclined terrain and side slope [23]. The tall body of a humanoid robot aid it to conveniently interact with humans and other objects such as desks or tables. Despite the many advantages offered by humanoid robots, their design is complex and expensive because it requires many actuators and other electronic components. Additionally, it is not necessary for a robot to locomote like humans, to operate in a human environment.

Wheeled mobile robots, compared with legged robots, have a simple design and relatively easy to control. They also have several advantages, such as reduced energy consumption and increased velocity of motion [24]. Traditional four-wheeled mobile robots can easily climb stairs that have deep step treads if they use wheels with diameters that are relatively large compared to the riser of the step. However, these robots should have short body structures because if they have tall body structures, they can roll backward when climbing. There are some examples of four-wheeled mobile robots with tall body struc-


**Figure 1.2: Advantages and disadvantages of a self-balancing inverted pendulum robot.**

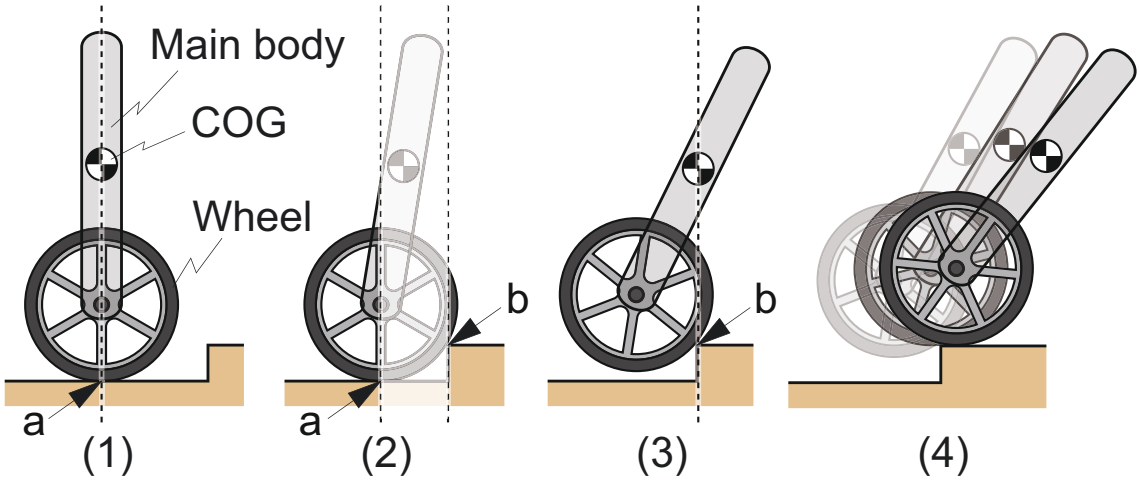


**Figure 1.3: The behavior of a conventional inverted pendulum robot.**

tures but are capable of climbing stairs [25, 26]. These robots use a special mechanism to maintain the center of gravity (COG), and therefore it can prevent them from rolling backward when climbing stairs. However, this mechanism increases the complexity of mobile robots and it requires additional actuators.

## 1.2 Related Works

### 1.2.1 Self-balancing inverted pendulum robot

A mobile robot based on a self-balancing inverted pendulum [27, 28, 29, 30] is a type of robot that is suitable for operation in human environments because it has a long vertical dimension and can travel through narrow passages, as shown in Figure 1.2. As most of them require only one or two contact points to touch the ground, the robots can have a slim build to move through congested human environments. The basic concept

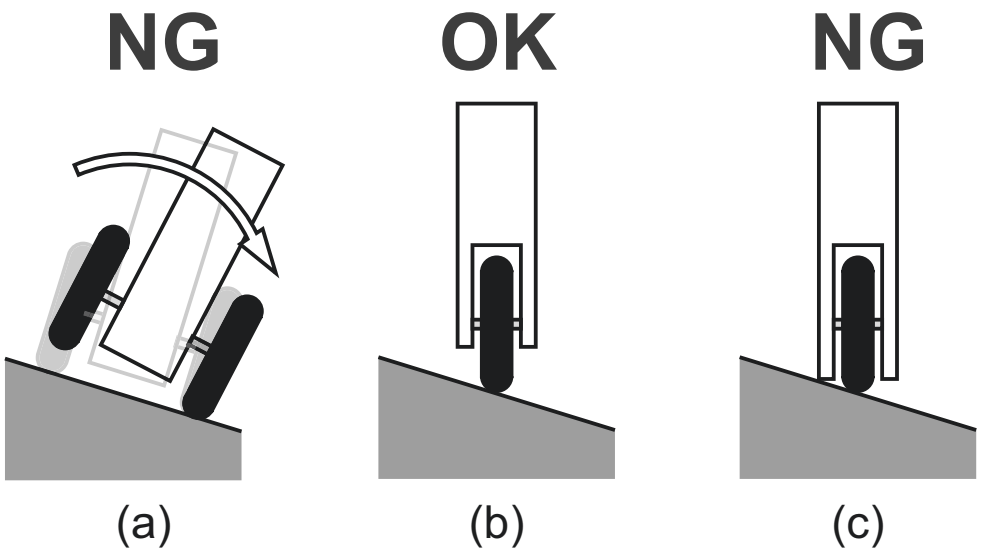


**Figure 1.4: Single-wheeled robot advantage over two-wheeled when moving on a side slope.**

of the inverted pendulum robot to achieve the balance when moving on a flat surface is by controlling the COG above the contact point, as shown in Figure 1.3(1) The inverted pendulum mobile robots fall into three categories: two-wheeled [31], single-wheeled [32, 33], and ballbot [34]. Although considered suitable for operating in a human environment, inverted pendulum mobile robots still need a dedicated mechanism for traversing stairs. This is because, the robot may have a high inclination when attempting to ascend the stair, and thus it is difficult to recover its stability after climbing, as illustrated in Figures 1.3(2), (3), and (4).

### 1.2.2 Single-wheeled inverted pendulum robot

A single-wheeled inverted pendulum robot (hereinafter, single-wheeled robot) is an inverted pendulum robot with a single contact point. This robot is statically unstable because a single wheel only gives one contact point, and thus requires two balancing mechanisms to achieve pitch and roll stability. While the wheel driving mechanism can provide pitch stability, the robot must include a dedicated mechanism to provide roll stability. Generally, there are two methods for providing roll stability. The inertia-

wheel-based single-wheeled robot generates torque on the lateral axis by accelerating or decelerating the inertia wheel [35, 36, 37, 38]. The spinning-flywheel-based single-wheeled robot utilizes a constantly spinning flywheel to maintain stability on the lateral axis [39, 40, 41, 42, 43]. This mechanism also offers an advantage in terms of producing a high balancing torque, compared with that of the inertia-wheel-based single-wheeled robot, but without using a high torque motor [41]. However, this mechanism requires two motors for controlling the flywheel spinning rate and its precession rate. Because lateral balance is actively controlled, it has the advantage of controlling lateral balance when moving on a side slope or turning on slanted terrain [40], as shown in Figure 1.4(b).

### 1.2.3 Inverted pendulum robot capable of climbing stairs

Many studies have investigated the capability of an inverted pendulum robot to climb stairs. Step-ascension modeling for a two-wheeled inverted pendulum robot by considering the center of gravity (COG) was introduced in extent studies [44]. The robot requires movement of the COG beyond the step corner to accomplish a climb. This results in steep inclination during climbing, creating imbalance if there is another step immediately after climbing because the robot requires a wide space to stabilize the longitudinal attitude. Stair-climbing by moving at a high speed was introduced [27]. Nevertheless, the imbalance can occur when a wheel strongly bumps against the step rise. Step traversing of an inverted pendulum robot using a special mechanism was developed in some studies.

Recently, there is a growing interest in the development of stair-climbing inverted pendulum robots using a special mechanism. Strah and Rinderknecht [45] developed a stair-climbing mechanism by using a double inverted pendulum. Although the robot they used had four wheels, it can yaw its body using a set of two wheels installed in the front or rear, and thus the motion is similar to a two-wheeled inverted pendulum robot. The robot employs a state transition between self-balancing using front and rear wheels, and all wheels come in contact with the ground to climb stairs. Ren and Luo [46, 47] developed a stair-climbing mechanism for an inverted pendulum robot using a triangular module of multiple wheels. The robot can rotate a pair of triangular modules on either side to climb

upstairs and maintain balance at the same time. Yang and Bewley [48] developed a two-wheeled robot with a rod-like leg mechanism in which the wheel axle can slide up the rod. The robot can achieve self-balancing by using its wheel as reaction wheels when its rod-like leg comes in contact with the ground. The robot employs a state transition between leg-balancing, wheel-balancing, and self-uprighting to climb up a step. Matsumoto et al., [49] developed the stair-climbing mechanism of inverted pendulum robot by using a biped type leg-wheeled robot. To climb the stairs, the robot uses biped leg-wheeled to climb the stair similar to human behavior traversing stairs. However, the robot has complex structures. Bannwarth et al., [50] developed the inverted pendulum robot with a reaction wheel. The reaction wheel is used to decrease the inclination when the robot climbing stairs. Nevertheless, the experiment results showed that the robot can only climb a low step. Some studies have developed inverted pendulum robots using a wheeled-leg mechanism [49, 51, 52]. This mechanism has the potential to maintain the lateral stability of the robot when it moves on a side slope by controlling the legs of the robot. However, the robot requires a high-torque motor or a high-reduction-ratio gear system to provide enough torque for the leg to support the weight of the robot. Additionally, some of the robots that have been developed [49, 52] have complex structures because they have several joints, and therefore require many actuators.

Takaki et al., [53] developed a stair-climbing inverted pendulum was developed using a planetary mechanism. The mechanism comprises an actuator, an arm, a belt, and a pulley and thus it is extremely simple. The function of the arms corresponds to moving the COG while ascending stairs and thus it can move the COG without showing a steep inclination. Figure 1.5 shows the proposed inverted pendulum robot prototype equipped with a laser-displacement sensor.

Figure 1.6 shows the method used by the author's stair-climbing inverted pendulum robot [53] to climb a step. An arm is provided between a wheel and the body to enable movement of the body. Figure 1.6(1) shows the self-balancing mode via active control wherein the robot shows a contact point (point a) between the wheel and flat ground. The stability is ensured by maintaining the COG above point a. Figure 1.6(2) shows the case when the robot contacts a step corner. The rotation of the wheel is restrained because of

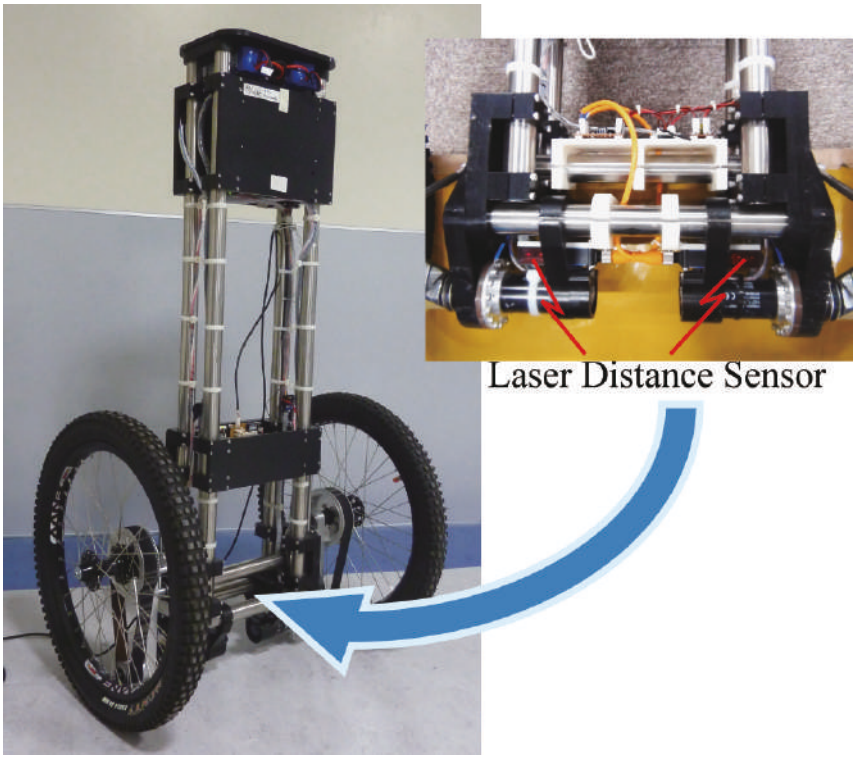


**Figure 1.5: Proposed Inverted Pendulum Robot Prototype Equipped with Laser-Displacement Sensor.**

the contact between the wheel and a step (point b). The robot is stable because the COG remains in between the two contact points (a and b) although the arm is moving. Under this condition, the arm lifts the body while the wheel remains intact with the step, and thus the COG shifts while approaching the step corner. Figure 1.6(3) shows the robot climbing the step when a contact point (point b) exists between the wheel and step corner by rolling the wheel on the step corner. Stability is accomplished by maintaining the COG above point b. Figure 1.6(4) shows the robot completely climbs the step. Balance is maintained in the same manner as described in Figure 1.6(1). The concept facilitates the step-climbing process because it is not necessary for the body to incline while shifting the COG.

## 1.3 Outline of thesis

This thesis is organized into four chapters as follows. In chapter 1, the problems associated with the mobility of the robot in a human environment is discussed, includ-

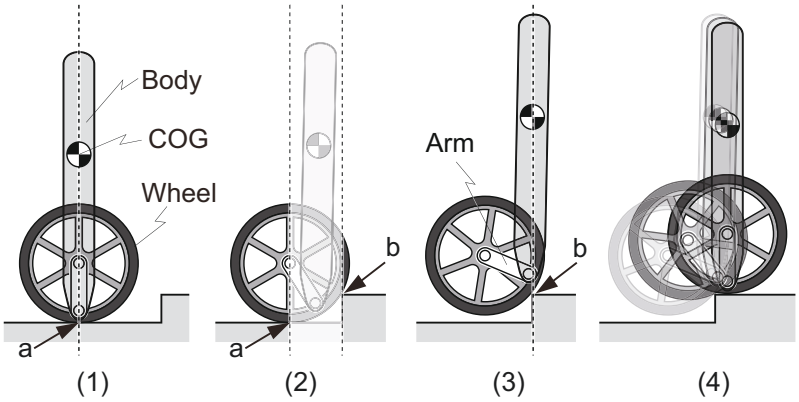


**Figure 1.6: Step-climbing behavior of the proposed stair-climbing inverted pendulum.**

ing the discussion about related works on some robots designed to operate in a human environment and the method on how those robots address some obstacles and objects that commonly exist in a human environment. This chapter also discusses recent developments of inverted pendulum robot and their potential to be employed in a human environment.

In chapter 2, the control method of the proposed stair-climbing robot using a two-wheeled inverted pendulum robot and the method to adjust the control parameters are discussed. The control method and its control parameters are both considered to ensure that the robot can traverse the stair and properly move in normal operation on a flat surface without losing its stability. The control parameters play a vital role to achieve stability both on normal operation and a climbing operation because a simple control method, which is a state-feedback control, is employed in the robot.

In chapter 3, the concept of a single-wheeled robot capable of climbing stairs is proposed. The robot is proposed to address the lateral stability problem on the two-wheeled stair-climbing robot prototype. The new design and arm configuration are proposed to provide a higher ground clearance to address the clearance problem when the robot moving on a lateral slope. The new driving mechanism is also proposed to ensure that a single motor can drive a wheel and the new arm design without any additional actuator. Chapter 4, the final chapter, summarizes the contribution of this study and discusses future works.

# Chapter 2

# Motion analysis of a two-wheeled stair-climbing inverted pendulum robot

In this chapter, the control method of the proposed stair-climbing robot using two-wheeled inverted pendulum robot [53] and the method to adjust the parameter of the controller are explained in detail. The robot uses the control method based on the state-feedback controller with feed-forward constant. Although the control method is simple, it can be used for stabilizing the body while moving on a flat surface and achieving stair-climbing motion. The method to adjust the parameter of the controller is composed by two consideration: the motion on a flat surface and motion on a step. However, the performance of the control method is dependent on the control parameter. As the initial step, the control parameter is determined based on the linearized dynamic model of the robot on a flat surface. On the latter, the compatibility of the control parameter is verified to ensures that it satisfies the condition for climbing. It is observed from the experiment that the robot requires sufficient space for recovering stability after climbing a step. This can cause the robot to fall down when the robot is climbing a stair given a narrow step tread. To address this problem, I apply a constant torque while the robot is climbing. The experiment and simulation results show that this method can reduce the distance for recovering stability after climbing a step.

This study also shows the stability of the stair-climbing motion by analyzing the orbital stability of its limit cycle [55]. The method can be used because stair-climbing motion is considered as a periodic motion. The stability analysis is numerically performed

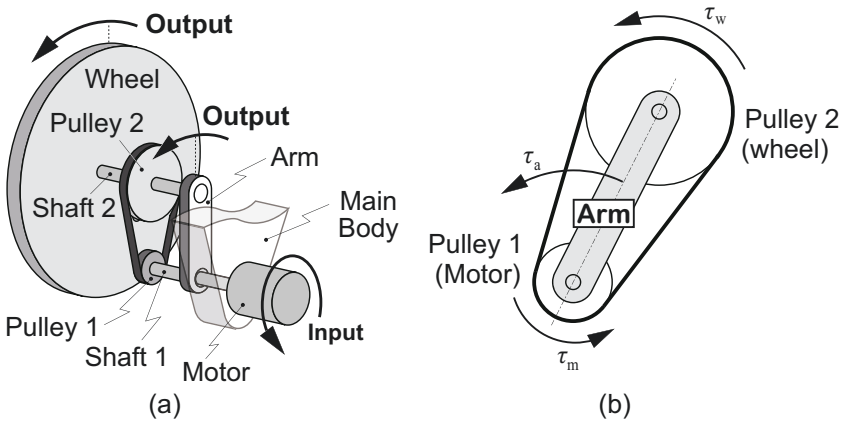


**Figure 2.1: Proposed planetary wheel mechanism**

by simulating the stair-climbing motion. The stability analysis indicates that the limit cycle of the stair-climbing motion is stable.

## 2.1 Two-wheeled stair-climbing inverted pendulum robot prototype

### 2.1.1 Planetary wheel mechanism using differential mechanism

The stair-climbing inverted pendulum robot adopts a differential mechanism principle to transmit power from single actuator into two outputs (i.e. the arm and wheel) and thus the robot is extremely simple because the actuator is decreased. The differential mechanism maintains a balance between the respective applied torques of the three inputs or outputs.

The proposed mechanism is shown in Figure 2.1. As shown in Figure 1.6, the concept is realized by the mechanism that consists of an arm, a belt, pulley 1, pulley 2, shaft 1, shaft 2, and a wheel. Pulley 1 is fixed on shaft 1 and pulley 2 and the wheel are fixed on shaft 2. Shaft 1 and shaft 2 are freely rotated with respect to the arm. Power is generated by a motor that is installed on shaft 1. Power from shaft 1 is transferred to pulley 1 and transmitted to pulley 2 via a belt and thus it rotates the wheel. Let the torques of the motor, arm, and wheel correspond to $\tau_m, \tau_a$, and $\tau_w$, respectively. Specifically, $R$ denotes the reduction ratio between pulley 1 and pulley 2. The relationship between $\tau_m, \tau_a$,and $\tau_w$,

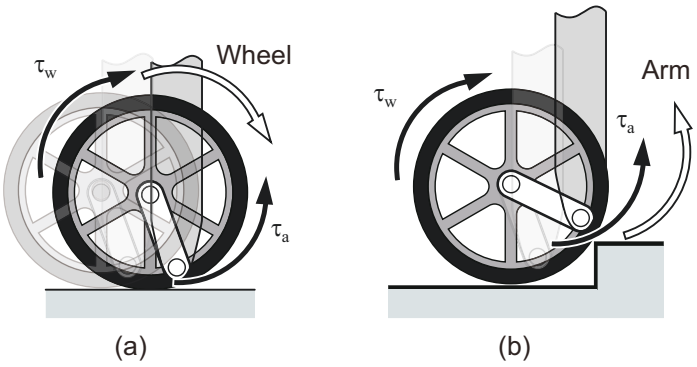


**Figure 2.2: Proposed planetary wheel mechanism**

is as follows [53]:

$$\tau_m = \frac{\tau_a}{R-1} = -\frac{\tau_w}{R}. \tag{2.1}$$

The motion on the flat surface is shown in Figure 2.2(a). In this case, the self-balancing of the inverted pendulum robot is achieved via a low motor torque $\tau_m$. This is possible because the slight inclination of the body is controlled by the small movement of the wheel. Based on Equation (2.1), the low motor torque $\tau_m$ generates low torque on the arm $\tau_a$ and thus it is unable to lift the body because the body is heavy.

The climbing motion is shown in Figure 2.2(b). In this case, the motor torque $\tau_m$ is allowed to become extremely high without inducing a movement on the wheel. This condition is possible because the wheel is restrained by contact with a step corner. When $\tau_m$ increases, $\tau_a$ is also increases until it sufficient to lift the body. The use of this concept enables control of the wheel and the arm via a single actuator by considering the existence of the step. Therefore, the realization of a climbing and traveling motion is extremely simple.

### 2.1.2 Hardware configuration

The robot is driven by two 120 W brushless motors (Maxon, EC 40). The motor is controlled by motor drivers (DES 70/10, manufactured by Maxon) via a controller area

network (CAN) bus from an external laptop computer (CF-T8, manufactured by Panasonic). The robot is equipped with a three-axis attitude sensor (AMU-3002, manufactured by Sumitomo Precision Products Co., Ltd.) and encoders to measure the rotation of each wheel and arm. Two laser sensors are used to measure the stair's riser surface angle relative to the robot. In this system, a SICK DT-10 laser sensor is utilized. The sensor can measures the distances ranging from 50 mm to 500 mm with an accuracy of ±1 mm. The distance between the two sensors is 190 mm. The configuration of these sensors in the robot is shown in Figure 1.5.

## 2.2 Motion on flat surface

This section focuses on the control method and the control parameter adjustment for stabilizing the body while moving on a flat surface and achieving the step-climbing motion. First, I describe the control method and the control parameter adjustment using the linearized dynamic model of the robot on a flat surface. Second, I describe the compatible control parameter condition for achieving a step-climbing motion based on the static balance of the robot on a step. Third, I describe the supplementary torque algorithm for applying constant torque to reduce the stability recovery distance after climbing. Fourth, I describe the control method for controlling the orientation of the robot towards the the stairs. Fifth, I explain the method to implement stabilization control, orientation control, and the supplementary torque for climbing in the robot. The stability of the step-climbing motion realized by the proposed control method is discussed in section 2.2.3.

### 2.2.1 Dynamic model of the robot

The robot consists of three rigid bodies, namely the arm, body, and wheel, as shown in Figure 2.3. To fully describe the motion, I select the generalized coordinates with respect to the global fixed frame $\{N\}$ that consists of the position coordinate $\boldsymbol{P}$ and angle coordinate $\boldsymbol{\theta}$ of each rigid body. Specifically, $\boldsymbol{P}_i = [P_{xi}\ P_{zi}]^T$ denotes the COG position of each rigid body in the $x$ and $z$ axes where index $i$, $(i = 1, 2, 3)$ represents the index of the rigid bodies, namely the body, arm, and wheel, respectively. Furthermore, $\boldsymbol{\theta} = [\theta_1\ \theta_2\ \theta_3]^T$

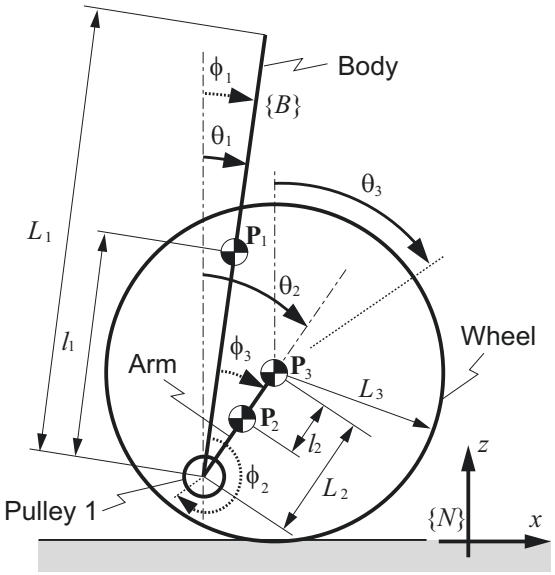


**Figure 2.3: Robot coordinates on flat surface**

consists of the body pitch $\theta_1$, arm angle $\theta_2$, and wheel angle $\theta_3$.

Let $T$, $U$, and $F$ denote the kinetic, potential, and damping energy of the three rigid bodies, respectively, and $\omega_i$ denotes the torque applied to each rigid body. The Lagrangian equation of motion is as follows:

$$\frac{d}{dt}\left(\frac{\partial T}{\partial \dot{\theta}_i}\right) - \frac{\partial T}{\partial \theta_i} + \frac{\partial F}{\partial \dot{\theta}_i} + \frac{\partial U}{\partial \theta_i} = \omega_i. \tag{2.2}$$

where $T$, $U$, and $F$ are as follows:

$$T = \frac{1}{2}\sum_{i=1}^{3}\left(m_i\left(\dot{P_{xi}}^2 + \dot{P_{zi}}^2\right) + I_i\dot{\theta_i}^2\right), \tag{2.3}$$

$$U = \sum_{i=1}^{3} m_i g p_{zi}, \tag{2.4}$$

$$F = \frac{1}{2}\mu_1(\dot{\theta}_2 - \dot{\theta}_1)^2 + \frac{1}{2}\mu_2(\dot{\theta}_3 - \dot{\theta}_2)^2. \tag{2.5}$$

where $m_i$ and $I_i$ denote the mass and inertia moment of the rigid bodies, respectively; $g$ denotes the gravity acceleration; and $\mu_1$ and $\mu_2$ denote the damping friction in shafts 1

and 2, respectively. $\boldsymbol{P}_1$, $\boldsymbol{P}_2$, and $\boldsymbol{P}_3$ are governed by the holonomic constraints as follows:

$$\boldsymbol{P}_1 = \boldsymbol{P}_3 + L_2[-\sin\theta_2 \ -\cos\theta_2]^T + l_1[\sin\theta_1 \ \cos\theta_1]^T, \tag{2.6}$$

$$\boldsymbol{P}_2 = \boldsymbol{P}_3 + l_2[-\sin\theta_2 \ -\cos\theta_2]^T, \tag{2.7}$$

$$\boldsymbol{P}_3 = L_3[\theta_3 \ 1]^T, \tag{2.8}$$

where, $L_1$, $L_2$, and $L_3$ denote the lengths of the body, arm, and radius of the wheel, respectively. Additionally, $l_1$ denotes the COG of the body with respect to shaft 2, and $l_2$ denotes the COG of the arm with respect to $P_3$. The dynamic model of the robot is obtained via expanding Equation (2.2) using Equations (2.3)-(2.8), arranged as follows:

$$\boldsymbol{M}(\boldsymbol{\theta})\ddot{\boldsymbol{\theta}} + \boldsymbol{C}(\boldsymbol{\theta},\dot{\boldsymbol{\theta}})\dot{\boldsymbol{\theta}} + \boldsymbol{D}\dot{\boldsymbol{\theta}} + \boldsymbol{G}(\boldsymbol{\theta}) = \boldsymbol{\omega}, \tag{2.9}$$

where $\boldsymbol{M}(\boldsymbol{\theta}) \in \boldsymbol{R}^{3\times3}$, $\boldsymbol{D} \in \boldsymbol{R}^{3\times3}$, and $\boldsymbol{C}(\boldsymbol{\theta},\dot{\boldsymbol{\theta}}) \in \boldsymbol{R}^{3\times3}$ denote the symmetric inertia, viscosity, and coriolis matrices, respectively, and $\boldsymbol{G}(\boldsymbol{\theta}) \in \boldsymbol{R}^{3\times1}$ and $\boldsymbol{\omega} \in \boldsymbol{R}^{3\times1}$ denote the gravitational force, and torque vectors in generalized coordinates, respectively. The component of each matrix is given as follows:

$$\boldsymbol{M}(\boldsymbol{\theta}) = \begin{bmatrix} M_{11} & M_{12} & M_{13} \\ M_{21} & M_{22} & M_{23} \\ M_{31} & M_{32} & M_{33} \end{bmatrix}, \tag{2.10}$$

$$\boldsymbol{D} = \begin{bmatrix} \mu_1 & -\mu_1 & 0 \\ -\mu_1 & \mu_1+\mu_2 & -\mu_2 \\ 0 & -\mu_2 & \mu_2 \end{bmatrix}, \tag{2.11}$$

$$\boldsymbol{C}(\boldsymbol{\theta}, \dot{\boldsymbol{\theta}}) = \begin{bmatrix} 0 & -m_1 l_1 L_2 c_{1\bar{2}} \dot{\theta}_2 & 0 \\ -m_1 l_1 L_2 c_{1\bar{2}} \dot{\theta}_1 & 0 & 0 \\ -m_1 l_1 L_3 s_1 \dot{\theta}_1 & (m_1 L_2 L_3 + m_2 l_2 L_3) s_2 \dot{\theta}_2 & 0 \end{bmatrix}, \tag{2.12}$$

$$\boldsymbol{G}(\boldsymbol{\theta}) = \begin{bmatrix} -m_1 g l_1 s_1 \\ m_1 g L_2 s_2 + m_2 g l_2 s_2 \\ 0 \end{bmatrix}, \tag{2.13}$$

$$\boldsymbol{\omega} = \begin{bmatrix} \omega_1 \\ \omega_2 \\ \omega_3 \end{bmatrix}. \tag{2.14}$$

The components of the matrix $\boldsymbol{M}$ are expressed as follows:

$$M_{11} = m_1 l_1^2 + I_1, \tag{2.15}$$

$$M_{22} = m_1 L_2^2 + m_1 l_2^2 + I_{2,} \tag{2.16}$$

$$M_{33} = m_1 L_3^2 + m_2 L_3^2 + m_3 L_3^2 + I_3, \tag{2.17}$$

$$M_{12} = M_{21} = -m_1 l_1 L_2 c_{1\bar{2}}, \tag{2.18}$$

$$M_{13} = M_{31} = m_1 l_1 L_3 c_1, \tag{2.19}$$

$$M_{23} = M_{32} = -m_1 L_2 L_3 c_2 - m_2 l_2 L_3 c_2, \tag{2.20}$$

where, $s_i = \sin\theta_i$, $c_i = \cos\theta_i$, $c_{i\bar{j}} = \cos(\theta_i - \theta_j)$.

### 2.2.2 Relationship between torques in global coordinates and local coordinates

The generalized torque $\boldsymbol{\omega}$ expressed in section 2.2.1 represents the torque acting on each element of the robot with respect to the global fixed frame $\{N\}$. However, the robot only uses one motor torque $\tau_m$. To obtain the relationship between $\boldsymbol{\omega}$ and $\tau_m$, I need to

consider the angle vector with respect to the body frame $\{B\}$.

Let $\boldsymbol{\phi} = [\phi_1\ \phi_2\ \phi_3]^T$ denote the angle vector with respect to the body frame $\{B\}$, where $\phi_1$, $\phi_2$, and $\phi_3$ denote the angle of the body, angle of pulley 1 relative to the body, and angle of the arm relative to the body, respectively. As shown in Figure 2.3, I obtain the expression of body pitch angle $\theta_1$ and arm angle $\theta_2$ in local coordinate vectors as follows:

$$\theta_1 = \phi_1, \tag{2.21}$$

$$\theta_2 = \phi_1 + \phi_3. \tag{2.22}$$

The relationship between $\theta_2$, $\theta_3$, $\phi_2$, and $\phi_3$ by considering pulley 1 and wheel rotation with the arm as a reference is as follows:

$$\phi_2 - \phi_3 = R(\theta_3 - \theta_2). \tag{2.23}$$

Additionally, $\theta_3$ is obtained by substituting Equation (2.22) into Equation (2.23) and expressed as follows:

$$\theta_3 = \phi_1 + \frac{1}{R}\phi_2 + \frac{R-1}{R}\phi_3. \tag{2.24}$$

The relationship of $\boldsymbol{\theta}$ and $\boldsymbol{\phi}$ is arranged in a matrix $\boldsymbol{E} \in R^{3\times3}$ form as follows:

$$\boldsymbol{\theta} = \boldsymbol{E}\boldsymbol{\phi}, \tag{2.25}$$

where, the component of the matrix $\boldsymbol{E}$ is obtained by considering Equations (2.21)-(2.24) as follows:

$$\boldsymbol{E} = \begin{bmatrix} 1 & 0 & 0 \\ 1 & 0 & 1 \\ 1 & \frac{1}{R} & \frac{R-1}{R} \end{bmatrix}. \tag{2.26}$$

Let the actual applied torque that acted on the body frame $\{B\}$ be $\boldsymbol{\tau} = [\tau_1\ \tau_2\ \tau_3]^T$.

The relationship between $\boldsymbol{\tau}$ and $\boldsymbol{\omega}$ is obtained through the principle of the virtual work as follows:

$$[\delta\theta_1\ \delta\theta_2\ \delta\theta_3]\boldsymbol{\omega} = [\delta\phi_1\ \delta\phi_2\ \delta\phi_3]\boldsymbol{\tau}. \tag{2.27}$$

From Equation (2.26), the virtual differential displacements $\delta\theta_1$, $\delta\theta_2$, and $\delta\theta_3$ are expressed by $\delta\phi_1$, $\delta\phi_2$, and $\delta\phi_3$ as follows:

$$[\delta\theta_1\ \delta\theta_2\ \delta\theta_3]^T = \boldsymbol{E}[\delta\phi_1\ \delta\phi_2\ \delta\phi_3]^T. \tag{2.28}$$

Based on the configuration of the robot, the motor torque $\tau_m$ is applied on the $\phi_2$ coordinate. Additionally, no torque is applied on the $\phi_1$ and $\phi_3$ coordinates. Therefore $\boldsymbol{\tau} = [0\,1\,0]^T\tau_m$. Subsequently, the relationship between $\boldsymbol{\omega}$ and motor torque $\tau_m$ is obtained from Equations (2.27) and (2.28) as follows:

$$\boldsymbol{\omega} = (\boldsymbol{E}^T)^{-1}[0\ 1\ 0]^T\tau_m. \tag{2.29}$$

### 2.2.3 Control method for body stabilization

In this section, we discuss the state-feedback controller with a feed-forward constant to stabilize the body on a flat surface. I desire stability around its equilibrium point by linearizing Equation (2.9). By substituting Equation (2.29) into Equation (2.9), the linearized dynamic model is obtained as follows:

$$\tilde{\boldsymbol{M}}\ddot{\boldsymbol{\theta}} + \boldsymbol{D}\dot{\boldsymbol{\theta}} + \tilde{\boldsymbol{G}}\boldsymbol{\theta} = (\boldsymbol{E}^T)^{-1}[0\ 1\ 0]^T\tau_m, \tag{2.30}$$

where $\tilde{\boldsymbol{M}} \in \boldsymbol{R}^{3\times3}$ and $\tilde{\boldsymbol{G}} \in \boldsymbol{R}^{3\times3}$ denote the symmetric inertia matrix and gravitational matrix, respectively, wherein

$$\tilde{\boldsymbol{M}} = \begin{bmatrix} \tilde{M}_{11} & \tilde{M}_{12} & \tilde{M}_{13} \\ \tilde{M}_{21} & \tilde{M}_{22} & \tilde{M}_{23} \\ \tilde{M}_{31} & \tilde{M}_{32} & \tilde{M}_{33} \end{bmatrix}, \tag{2.31}$$

$$\tilde{\boldsymbol{G}} = \begin{bmatrix} -m_1 g l_1 & 0 & 0 \\ m_1 g L_2 & m_2 g l_2 & 0 \\ 0 & 0 & 0 \end{bmatrix}, \tag{2.32}$$

where,

$$\tilde{M}_{11} = m_1 l_1^2 + I_1, \tag{2.33}$$

$$\tilde{M}_{22} = m_1 L_2^2 + m_1 l_2^2 + I_2, \tag{2.34}$$

$$\tilde{M}_{33} = m_1 L_3^2 + m_2 L_3^2 + m_3 L_3^2 + I_3, \tag{2.35}$$

$$\tilde{M}_{12} = \tilde{M}_{21} = -m_1 l_1 L_2, \tag{2.36}$$

$$\tilde{M}_{13} = \tilde{M}_{31} = m_1 l_1 L_3, \tag{2.37}$$

$$\tilde{M}_{23} = \tilde{M}_{32} = -m_1 L_2 L_3 - m_2 l_2 L_3. \tag{2.38}$$

It is difficult to determine the position of the robot from the wheel angle $\theta_3$ when the shape of the ground is complicated because of the steps or when the wheel slips. Furthermore, as shown in the dynamic model Equation (2.30), the components of $\tilde{\boldsymbol{M}}$, $\boldsymbol{D}$ and $\tilde{\boldsymbol{G}}$ are independent from $\theta_3$. This implies that $\theta_3$ does not contribute to the stability of the robot. Therefore, I select $\boldsymbol{x} = [\theta_1\ \theta_2\ \dot{\theta}_1\ \dot{\theta}_2\ \dot{\theta}_3]^T$ as the control variables. The control law is designed as follows:

$$\tau_m = -\boldsymbol{K}\boldsymbol{x} + K_v, \tag{2.39}$$

where $\boldsymbol{K} = [K_1\ K_2\ K_3\ K_4\ K_5]$ denotes the feedback control gain and $K_v$ denotes the feed-forward constant for providing the reference input speed of the robot. The linearized dynamic model is expressed in a state-space form as follows:

$$\dot{\boldsymbol{x}} = \boldsymbol{A}\boldsymbol{x} + \boldsymbol{B}\tau_m. \tag{2.40}$$

$\boldsymbol{A}$ and $\boldsymbol{B}$ are described as follows:

$$\boldsymbol{A} = \left( \begin{array}{c|c} \boldsymbol{O}^{2\times 2} & \boldsymbol{A}_{12} \\ \hline \boldsymbol{A}_{21} & \boldsymbol{A}_{22} \end{array} \right), \tag{2.41}$$

$$\boldsymbol{B} = \left( \begin{array}{c} \boldsymbol{O}^{1\times 2} \\ \hline \boldsymbol{b} \end{array} \right). \tag{2.42}$$

The matrices $\boldsymbol{A}_{12} \in \boldsymbol{R}^{3\times 2}$, $\boldsymbol{A}_{21} \in \boldsymbol{R}^{2\times 3}$, $\boldsymbol{A}_{22} \in \boldsymbol{R}^{3\times 3}$, and $\boldsymbol{b} \in \boldsymbol{R}^{1\times 3}$ represent the system. The elements of the system matrices are described as follows:

$$\boldsymbol{A}_{12} = \begin{bmatrix} 1 & 0 & 0 \\ 0 & 1 & 0 \end{bmatrix}, \tag{2.43}$$

$$\boldsymbol{A}_{21} = -(\tilde{\boldsymbol{M}})^{-1}\tilde{\boldsymbol{G}} \begin{bmatrix} 1 & 0 \\ 0 & 1 \\ 0 & 0 \end{bmatrix}, \tag{2.44}$$

$$\boldsymbol{A}_{22} = -(\tilde{\boldsymbol{M}})^{-1}\boldsymbol{D}, \tag{2.45}$$

$$\boldsymbol{b} = \tilde{\boldsymbol{M}}^{-1}(\boldsymbol{E}^T)^{-1}[0\ 1\ 0]^T. \tag{2.46}$$

The linearized closed-loop dynamic is as follows:

$$\dot{\boldsymbol{x}} = (\boldsymbol{A} - \boldsymbol{B}\boldsymbol{K})\boldsymbol{x} + \boldsymbol{B}K_v. \tag{2.47}$$

To stabilize the robot, I use the pole-placement method to obtain $\boldsymbol{K}$ by ensuring all real parts of the eigenvalues of $\boldsymbol{A} - \boldsymbol{B}\boldsymbol{K}$ are negative. From the system parameters that are listed in Table 2.1, I use the heuristic method to select the pole as follows:

$$\boldsymbol{\iota} = [-2.53 \pm 12.93i\ \ -3.85 \pm 5.62i\ \ -5.71]. \tag{2.48}$$

Subsequently, I obtain $\boldsymbol{K}$ as follows:

$$\boldsymbol{K} = [60.833 \ -2.500 \ 20.584 \ -2.916 \ 3.999]. \tag{2.49}$$

The next issue is $K_v$. The addition of $K_v$ will affect the steady state solution of the closed-loop dynamics of Equation (2.47). It can be used to control the velocity of the robot which is represented by the velocity of the wheel $\dot{\theta}_3$. To use $K_v$ as a velocity controller, let $K_v$ be $G^d\dot{\theta}_3$, where $G$ and ${}^d\dot{\theta}_3$ denote the feed-forward gain for compensating the steady state of the wheel velocity and the desired wheel velocity, respectively. The steady state of the closed loop system $\boldsymbol{x}(\infty)$ is given by the following:

$$\boldsymbol{x}(\infty) = (\boldsymbol{A} - \boldsymbol{BK})^{-1}\boldsymbol{B}G^d\dot{\theta}_3. \tag{2.50}$$

The relationship between the steady state of the wheel velocity $\dot{\theta}_3(\infty)$ and $\boldsymbol{x}(\infty)$ is as follows:

$$\dot{\theta}_3(\infty) = \boldsymbol{C}\boldsymbol{x}(\infty). \tag{2.51}$$

where $\boldsymbol{C} = [0\ 0\ 0\ 0\ 1]$ denotes the output matrix to obtain the state of $\dot{\theta}_3$. To satisfy $\dot{\theta}_3(\infty) = {}^d\dot{\theta}_3$, $G$ must be chosen as follows [54]:

$$G = -1/(\boldsymbol{C}(\boldsymbol{A} - \boldsymbol{BK})^{-1}\boldsymbol{B}), \tag{2.52}$$

It must be noted that the result of $(\boldsymbol{C}(\boldsymbol{A} - \boldsymbol{BK})^{-1}\boldsymbol{B})$ is scalar. Using Equations (2.41), (2.42), and (2.49) in Equation (2.52), I obtain $G$ as 0.31.

### 2.2.4 Control method for controlling the orientation towards the step

In this subsection, I describe the control design for the $xy$-plane, which is utilized for controlling the orientation of the robot. I consider two areas at which the robot attempts to climb the stair. Area I is the area before climbing the stair and Area II is the area after climbing the stair. Figure 2.5 illustrates the desired trajectory for climbing the

**Table 2.1: System Parameters**

| | | |
|---|---|---|
| Mass | $m_1$ | 13.20 kg |
| | $m_2$ | 0.87 kg |
| | $m_3$ | 3.56 kg |
| Inertia | $I_1$ | 2.44 kgm$^2$ |
| | $I_2$ | 0.01 kgm$^2$ |
| | $I_3$ | 0.12 kgm$^2$ |
| Length | $L_1$ | 1.12 m |
| | $L_2$ | 0.19 m |
| | $L_3$ | 0.25 m |
| | $l_1$ | 0.56 m |
| | $l_2$ | 0.08 m |
| | $l_3$ | 0.25 m |
| Reduction Ratio | $R$ | 3 |

stair with the different angles for the different steps by considering the target area.

**Before ascending step:** The robot encounters difficulties if it climbs the step without adjusting its orientation towards the step. Moreover, The robot encounters difficulties with respect to changing its orientation when the wheels make contact with the corners of the steps. In contrast, if the wheels contact only the ground, it is easy to change the orientation. Therefore, the robot needs to adjust the orientation before making contact with the step. This requirement can be achieved by controlling its orientation by using a laser-distance sensor that detects the angle of the step that is in the desired range. The defined ranged of detection extends from 200 mm to 500 mm. Area I, which is shown in Figure 2.5, illustrates the operating area needed for adjusting the robot's orientation towards the step. The equation employed to obtain the stair's riser surface angle is derived as follows. To do so, I must consider a robot platform in the $xy$-plane, which is shown in Figure 2.4. Let $\delta\psi$ denotes the angle of the robot relative to the normal vector of stair's riser surface. The distances between the robot and the stair's riser surfaces, which are acquired from the right and left sensors, are denoted by $d_r$ and $d_l$, respectively. The distance between the two sensors is denoted by $l$. Then, the angle of the robot relative to the stair's riser surface can be determined as follows:

$$\delta\psi = \tan^{-1}(\frac{d_l - d_r}{l}). \tag{2.53}$$

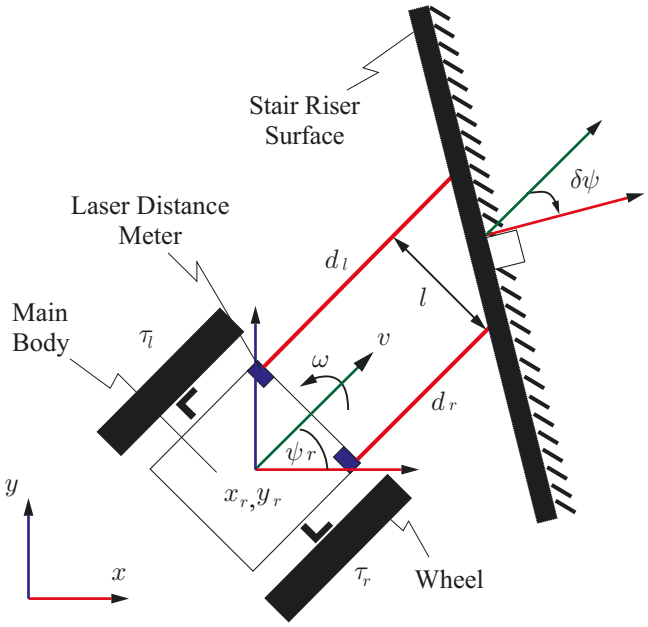


**Figure 2.4: Orientation Control Schematic.**

**After ascending step:** After climbing the step, The robot's orientation varies because of the climbing maneuvers. Nevertheless, the robot encounters difficulty while adjust its orientation towards the next step if widths of the step are narrow. In addition, there are several possibilities where the laser sensor cannot detect the angle of the next step. To deal with this problem, the robot's orientation must be controlled to be the same as in a previous step angle after successful ascension. This condition can be achieved by minimizing the orientation error between the robot's orientation and the angle of the climbed step. The angle of the climbed step is defined as the desired orientation $\psi_d$, which is illustrated in Figure 2.5. The desired orientation can be obtained from the last recording of the robot orientation while adjust the robot orientation towards the step.

**Control law:** Figure 2.5 shows an example of desired trajectory for climbing the stair with steps having different angles. The robot detects each step and adjust its orientation towards it. This first condition area is shown in Area I in Figure 2.5. After successfully climbing the step, the robot then adjust its orientation towards the desired orientation $\psi_d$, which is obtained from the robot orientation after successfully adjusting

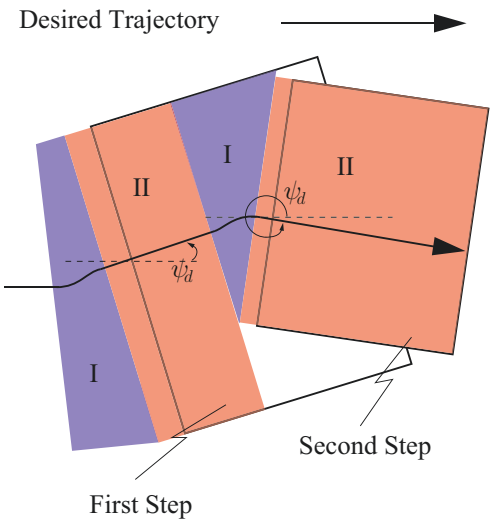


**Figure 2.5: Desired trajectory for climbing the stair with an orientation error between the robot and step.**

its orientation towards the step. The second condition area is shown in Area II in the first step aisle, which is shown in Figure 2.5. Then, the robot continues to adjust its orientation towards the next step, as illustrated in Area I. After adjusting the orientation towards the step, the robot again adjust its orientation towards the desired orientation, as illustrated in Area II in the second step aisle. In order to satisfy the desired trajectory, I design the control law as follows. The torque $\tau_{xy}$ that is needed to minimize the orientation error $e$ is calculated as follows.

$$\tau_{xy} = K_{\psi} e + K_{\dot{\psi}} \dot{e}, \tag{2.54}$$

where $K_{\psi}$ and $K_{\dot{\psi}}$ are the proportional and derivative control parameter, respectively. $e$ is designed as follows.

$$e = \begin{cases} \delta\psi, & \text{if } 200\,mm < dr, dl < 500\,mm. \\ \psi_r - \psi_d, & \text{otherwise,} \end{cases} \tag{2.55}$$

The states of the body pitch ($\phi_1$, $\dot{\phi}_1$) can be obtained directly from the three-axis

attitude sensor. However, the pulley rotation angle and the arm angle cannot be obtained directly because the robot has two arms and two wheels, on the left and right sides.

For this robot, the angle and rotational velocity of each arm and motor are measured separately by each encoder. These data are denoted by $\phi_{2r}$, $\phi_{2l}$, $\phi_{3r}$, and $\phi_{3l}$. The subscripts of 2 and 3 indicate the arm and wheel, respectively, while the subscripts of $l$ and $r$ indicate the left side and right sides, respectively: e.g., $\phi_{2r}$ is the angle of the right arm. In order to implement the control law described in section 2.2.3, $\phi_2$ and $\phi_3$ are defined as follows.

$$\phi_2 = \frac{1}{2}(\phi_{2l} + \phi_{2r}), \tag{2.56}$$

$$\phi_3 = \frac{1}{2}(\phi_{3l} + \phi_{3r}), \tag{2.57}$$

I assume that the motion of the robot is composed of two motions. The first is the robot motion in the $xz$-plane, which affects its body attitude. The second is the robot motion in the $xy$-plane, which moves the robot to the desired position and orientation in the $xy$-plane. The following equations (2.58) and (2.59) are assumed to implement the control laws in the $xz$-plane and $xy$-plane, respectively.

$$\tau_r = \frac{1}{2}\tau_{xz} + \frac{L}{2R}\tau_{xy}, \tag{2.58}$$

$$\tau_l = \frac{1}{2}\tau_{xz} - \frac{L}{2R}\tau_{xy}, \tag{2.59}$$

where $\tau_r$ and $\tau_l$ are the torques that are applied for the right and left wheels, respectively, $R$ is the radius of the wheel and $L$ is the distance between the two wheels.

## 2.3 Motion on a step

Considering that the system has been stabilized when moving on a flat surface by the controller discussed in section 2.2.3, the step-climbing motion can be realized by making the robot move forward towards the step if the control parameter is correctly adjusted. However, if I determine the control parameter merely based on the motion on a flat surface, often the motor torque $\tau_m$ is not sufficient to force the wheel to climb over the

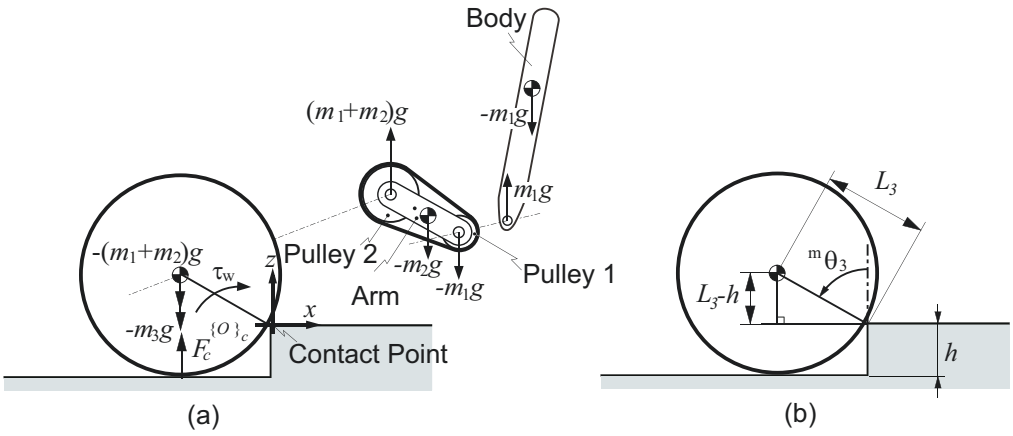


**Figure 2.6: Requirement torque to climb a step**

step and/or lift the body before the wheel climbs over the step. Therefore, in this section I discuss a compatible control parameter condition for realizing step-climbing motion.

### 2.3.1 Required Torque for Climbing a Step

This section discusses a required torque ${}^r\tau$ to climb a step. Under this condition, the wheel has two contact points; the contact point between the wheel and step corner $O_c$ and the contact point between the wheel and the base of the step, as shown in Figure 2.6(a). I assume that the axis rotation of the wheel while climbing over a step is located at $O_c$. This assumption holds if no slippage occurs in the contact point $O_c$.

Before I derive ${}^r\tau$, I need to consider the normal force $F_c$ and angle ${}^m\theta_3$ between the wheel and base of the step, as shown in Figures 2.6(a) and (b). From the free body diagram of the wheel shown in Figure 2.6(a), there are two forces acting on the wheel: the gravitational force $(m_1 + m_2 + m_3)g$ that acts on the axle of the wheel and $F_c$. Under a static condition, the torque equilibrium of the wheel with respect to the corner of the step $O_c$ is expressed as follows:

$$(F_c - (m_1 + m_2 + m_3)g)L_3 \sin {}^m\theta_3 = \tau_w, \tag{2.60}$$

where $\tau_w$ denotes the torque of the wheel. It must be noted that if the wheel is in contact with the base of the step ($F_c \neq 0$), $\tau_w$ is equal to zero. Additionally, $\tau_w$ is considered as

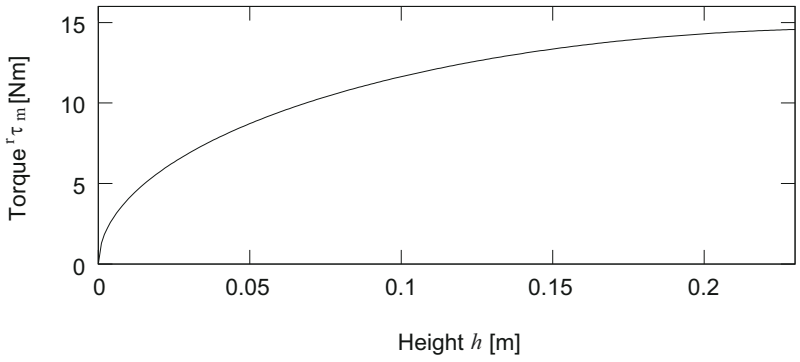


**Figure 2.7: Relationship between $h$ and $^r\tau_m$**

the torque to rotate the wheel with respect to $O_c$. From Figure 2.6(b), $^m\theta_3$ is obtained as follows:

$$^m\theta_3 = \cos^{-1}\frac{L_3 - h}{L_3} \tag{2.61}$$

where $h$ denotes the height of the step.

Here, $^r\tau$ is considered as $\tau_w$ immediately before the wheel lift-off from the base of the step, in which $F_c$ approaches zero. By considering Equations (2.60) and (2.61), $^r\tau$ is obtained as follows:

$$^r\tau = (m_1 + m_2 + m_3)g\sqrt{2L_3h - h^2}, \tag{2.62}$$

Notably, $^r\tau$ exists if $h$ is less than $L_3$. In the case where $h > L_3$, the wheel cannot climb over the step.

Equation (2.62) means that if $\tau_w$ exceeds $^r\tau$, the wheel starts to climb a step. For simplicity, I define $^r\tau_m$ as the motor torque $\tau_m$ required to climb a step. Given the reduction ratio $R$, $^r\tau_m$ is obtained by considering Equations (2.1) and (2.62) as follows:

$$^r\tau_m = \frac{(m_1 + m_2 + m_3)g\sqrt{2L_3h - h^2}}{R}. \tag{2.63}$$

Figure 2.7 shows the relationship between $h$ and $^r\tau_m$.

### 2.3.2 Required Torque for Lifting The Body by The Arm

To analyze the required motor torque $\tau_m$ to lift the body, I analyze the torque equilibrium of the arm and body. In this analysis, I assume that the wheel is restricted by a step and thus $\tau_m$ is distributed to the arm and body. Figure 2.8 shows the free body diagram of the arm and the body. I define $\tau_m$ and $\tau_a$ at the torque equilibrium as ${}^{eq}\tau_m$ and ${}^{eq}\tau_a$, respectively. Let equilibrium angle $\theta_1$ and $\theta_2$ be ${}^{eq}\theta_1$ and ${}^{eq}\theta_2$, respectively. Under the static condition, by considering the ${}^{eq}\tau_m$ and ${}^{eq}\tau_a$ in Figure 2.8, the following equations are obtained.

$$l_1 m_1 g \sin {}^{eq}\theta_1 - {}^{eq}\tau_m = 0, \tag{2.64}$$

$$(l_2 m_2 + L_2 m_1) g \sin {}^{eq}\theta_2 + {}^{eq}\tau_a = 0. \tag{2.65}$$

Therefore, as given in Equations (2.1), (2.64) and (2.65), the relationship among ${}^{eq}\tau_m$, ${}^{eq}\tau_a$, ${}^{eq}\theta_1$, and ${}^{eq}\theta_2$ can be obtained as follows:

$${}^{eq}\theta_1 = \sin^{-1} \frac{{}^{eq}\tau_m}{l_1 m_1 g}, \tag{2.66}$$

$${}^{eq}\theta_2 = \sin^{-1} \frac{-{}^{eq}\tau_m (R-1)}{(L_2 m_1 + l_2 m_2) g}. \tag{2.67}$$

To simplify the representation of ${}^{eq}\theta_1$ and ${}^{eq}\theta_2$, I represent them as the equilibrium angle of ${}^{eq}\phi_3$, which is illustrated in Figure 2.8. ${}^{eq}\phi_3$ is given as follows:

$${}^{eq}\phi_3 = {}^{eq}\theta_2 - {}^{eq}\theta_1. \tag{2.68}$$

Figure 2.9 shows the relationship between ${}^{eq}\tau_m$, ${}^{eq}\theta_1$, ${}^{eq}\theta_2$, and ${}^{eq}\phi_3$.

To assess the compatibility of the control parameter to lift the body, I compare the motor torque $\tau_m$ generated by the controller to the motor torque equilibrium ${}^{eq}\tau_m$ for lifting the body. To simplify, I perform the analysis under a static condition which means all acceleration and velocity terms are neglected. Additionally, I use the state of equilibrium angles ${}^{eq}\theta_1$ and ${}^{eq}\theta_2$ to determine the motor torque $\tau_m$. Therefore, the magnitude of the

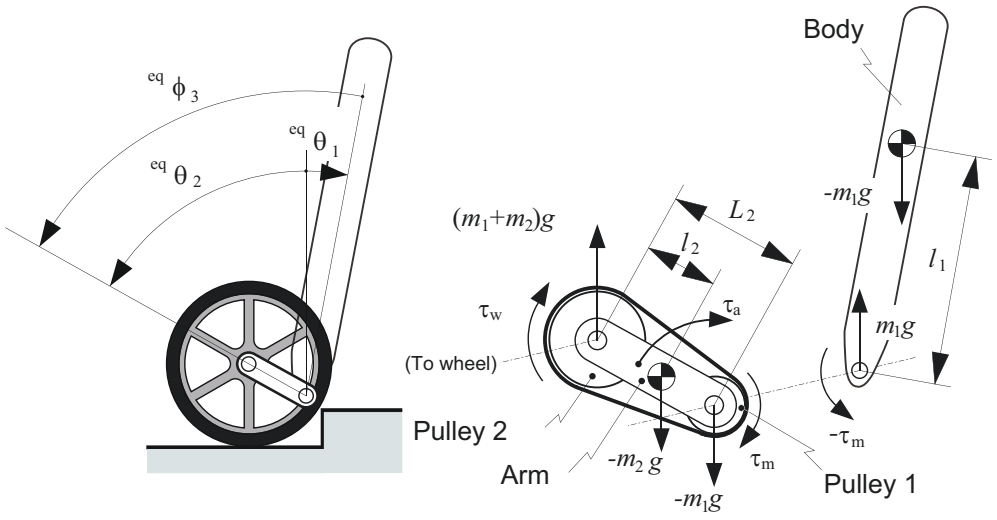


**Figure 2.8: Torque required to climb a step**

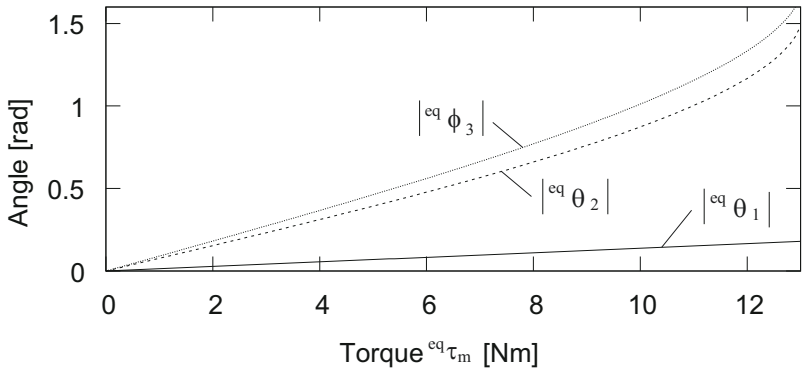


**Figure 2.9: Relationship between $\tau_m$, ${}^{eq}\theta_1$, ${}^{eq}\theta_2$ and ${}^{eq}\phi_3$**

motor torque $\tau_m$ used in this analysis obtained from Equation (2.39) is as follows.

$$\tau_m = -K_1^{eq}\theta_1 - K_2^{eq}\theta_2 + K_v, \tag{2.69}$$

Here, I consider the case where the robot climbs a step with a height of $h = 120$ mm. As shown in Figure 2.7, the required torque ${}^{r}\tau_m$ to climb the step corresponds to 12.4 Nm. Figure 2.10 shows the relationship between ${}^{eq}\phi_3$, $\tau_m$ and ${}^{eq}\tau_m$. In Figure 2.10, I use ${}^{eq}\phi_3$ to simplify the representation of ${}^{eq}\theta_1$ and ${}^{eq}\theta_2$.

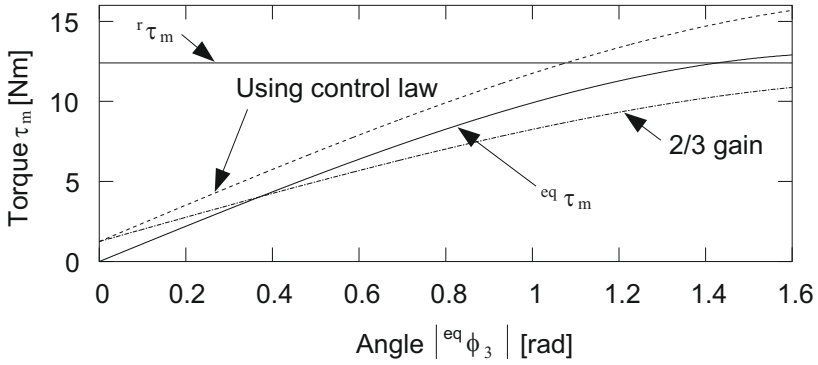


**Figure 2.10: Relationship between $\phi_3$ and $\tau_m$**

When the controller uses the control parameter described in Equation (2.49) and $K_v$ is set to 1.25 Nm, $\tau_m$ is illustrated in the dashed line in Figure 2.10. It is observed that the arm lifts up the body because $\tau_m$ always exceeds $^{eq}\tau_m$. This means, the $\tau_m$ generated by the controller using this control parameter is sufficient to lift the body. For reference, because the arm continues to rotate, as shown in Figure 2.10, $\tau_m$ will exceed $^r\tau_m$ at $^{eq}\phi_3 = 1.1$ rad. Thus, when the arm reaches this condition, the wheel also will start to lift-off from the base of the step.

For comparison, as shown in Figure 2.10, the dash-dotted line is observed when the robot uses 2/3 of the control parameter described in Equation (2.49). From the stability analysis using the dynamic model described in section 2.2.1, by using this control parameter, the robot can achieve the stable body attitude when moving on a flat surface. However, as shown in Figure 2.10, by using this control parameter, $\tau_m$ is lower than $^{eq}\tau_m$ when $\phi_3$ is greater than 0.37 rad. This means that the arm will stop to rotate after $\phi_3$ reaches the equilibrium point when $^{eq}\phi_3$ is 0.37 rad. As shown in Figure 2.10, in this condition, $\tau_m$ cannot exceeds $^r\tau_m$, and thus the step-climbing motion cannot be realized. This example shows that although I already select the stable control parameters for the motion on the flat surface, these control parameters cannot satisfy the parameter condition to realize the climbing motion.

### 2.3.3 Supplementary Torque for Climbing Stairs

By using the control method described in section 2.2.3, the robot can climb a step and return to the stable attitude if there is a sufficiently wide space after the robot climbs a step, as shown in Figure 2.11(a), because the body is slightly inclined when the robot climbs a step. In a human environment, a stair typically has a step with a narrow tread. In this case, the robot has difficulty recovering to the stable attitude after climbing.

To address this problem, I consider applying a constant torque while climbing the stair [53]. By adding the constant torque, the stability recovery distance $l$ is expected to decrease because, as described in free body diagram shown in Figure 2.8, the motor torque $\tau_m$ generates a counter torque to force the body to incline backward.

I consider applying the constant torque to the robot immediately after the wheel contacts the step. In this case, as shown in Figure 2.11(c), the body is inclining backward and thus the robot is unable to climb the step. Therefore, the timing for applying the constant torque is very important.

I consider applying the constant torque between the timing shown in Figures 2.11(a) and (c), as illustrated in Figure 2.11(b). Thus, when the arm reaches an appropriate angle, constant torque is applied to the motor. In this case, it is expected that the body inclination while climbing decreases, and thus the robot can reach the stable attitude within a shorter distance. I define the supplementary torque $\tau_s$ algorithm as the addition of the constant torque in this timing. To include $\tau_s$ in the control method, Equation (2.39) is modified as follows:

$$\tau_m = -\boldsymbol{K}\boldsymbol{x} + K_v + \tau_s \ \wedge \ |\tau_m + K_s| > |{}^r\tau_m|. \tag{2.70}$$

Notably, after the addition of constant torque, $\tau_m$ must be higher than ${}^r\tau_m$.

I introduce three variables to apply the supplementary torque $\tau_s$ algorithm, namely the magnitude of the supplementary torque $K_s$, top threshold $\phi_t$, and bottom threshold $\phi_b$ [53]. The sequences of the supplementary torque algorithm $\tau_s$ are described as follows. $\tau_s$ is set to $K_s$ when the arm angle $\phi_3$ reaches $\phi_t$. Under this condition, motor torque $\tau_m$ abruptly increases after $K_s$ is included and it is expected that the robot climbs a step. After

the robot successfully climbs a step, $\phi_3$ is expected to decrease. As $\phi_3$ reaches $\phi_b$, $\tau_s$ is set to zero. Therefore, $\tau_s$ has the following update rule:

$$\begin{aligned} \text{if} \quad & \tau_s = 0 \wedge |\phi_3| \geq |\phi_t| \quad \text{then} \quad \text{update} \ \tau_s \ \text{to} \ K_s. \\ \text{if} \quad & \tau_s = K_s \wedge |\phi_3| \leq |\phi_b| \quad \text{then} \quad \text{update} \ \tau_s \ \text{to} \ 0. \\ \text{else} \quad & \text{do not update } \tau_s. \end{aligned} \tag{2.71}$$

It is difficult to analytically determine $K_s$, $\phi_t$, and $\phi_b$ because I did not derive the dynamic model of the robot while climbing the step in this study. Therefore, we use a heuristic method to determine compatible $K_s$, $\phi_t$, and $\phi_b$ values for climbing a stair. I will show the effectiveness of $\tau_s$ by describing the relationship of $K_s$ with the stability recovery distance $l$ using the simulation. Additionally, I will show the effectiveness of $\tau_s$ via the experiment described in section 2.5. To show the effectiveness of the supplementary torque $\tau_s$ algorithm, I compare the relationship between the magnitude of the supplementary torque $K_s$ with the stability recovery distance $l$. The stability recovery distance $l$ is defined as the distance required for the robot to achieve a stable attitude after climbing with respect to a step corner. To obtain $l$, I simulate the robot climbing a single step with a height of 12 cm. The simulation of stair-climbing of inverted pendulum robot is built in an Open Dynamics Engine environment, as shown in Figure 2.12. The relationship of $l$ with the magnitude of the supplementary torque $K_s$ is plotted in Figure 2.13. From Figure 2.13, it can be understood that the $\tau_s$ algorithm can minimize the stability recovery distance $l$. The trend of Figure 2.13 shows that as $K_s$ increase, $l$ tends to decrease. However, at some $K_s$, the value of $l$ contradicts the trend of Figure 2.13.

To show the effectiveness of the $\tau_s$ algorithm on climbing the stair, I compare the stair-climbing simulation with and without the $\tau_s$ algorithm. In the simulation with the $\tau_s$ algorithm, I select the magnitude $K_s$ as 7.2 $Nm$. The comparison is completed by simulating the robot to climb stairs consisting of 10 steps with the height of the step as 12 cm and various lengths of step tread. I qualitatively compare the data by indicating whether the robot can climb the stair or not as shown in Figure 2.14. Figure 2.14 shows the result that with the $\tau_s$ algorithm the robot can climb the narrower step tread compared

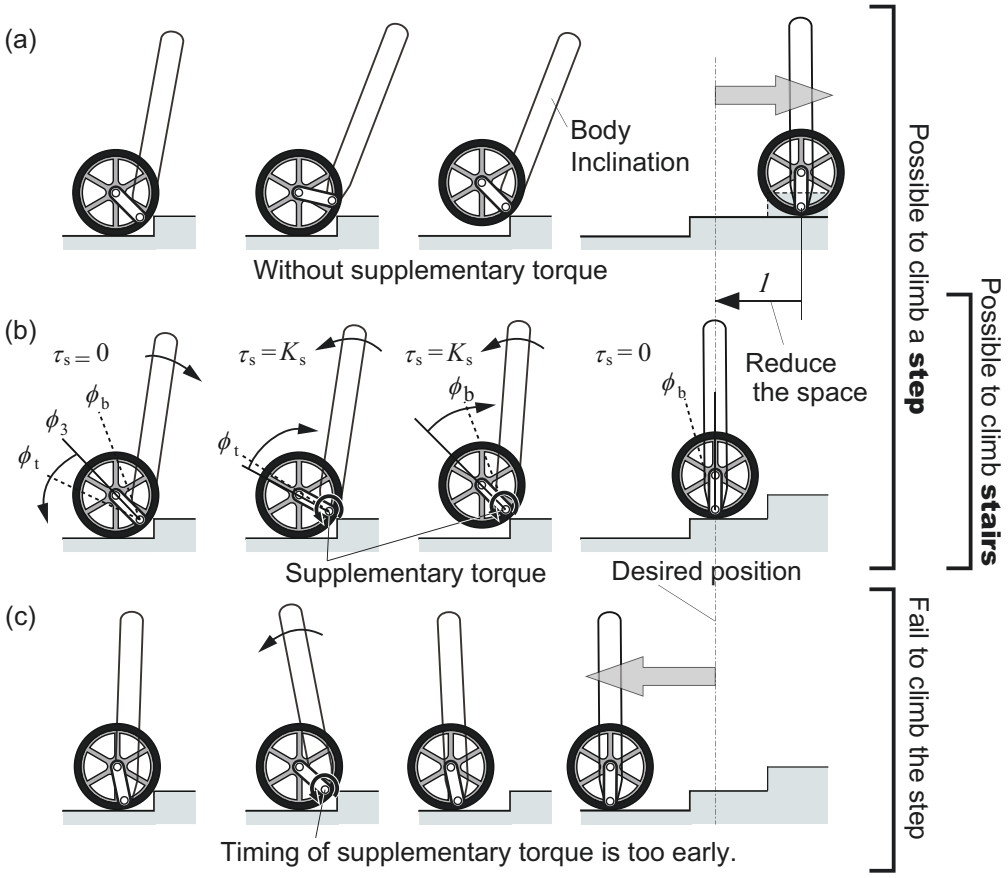


**Figure 2.11: Motion of climbing a step with the supplementary torque**

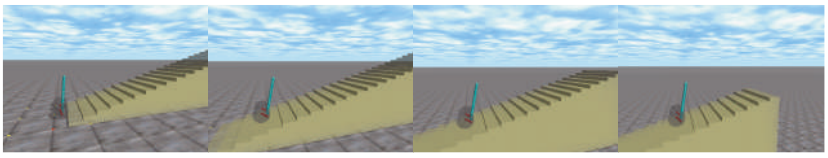

**Figure 2.12: Simulation of the robot in Open Dynamics Engine (ODE) environment.**

to the result without the $\tau_s$ algorithm.

## 2.4 Stability analysis of climbing stairs

Goswami et al. showed the method to analyze the stability of the cyclic motion of a nonlinear system by studying the fixed point stability in the Poincaré map [55]. The method is suitable for analyzing the stability of stair-climbing motion because it is consid-

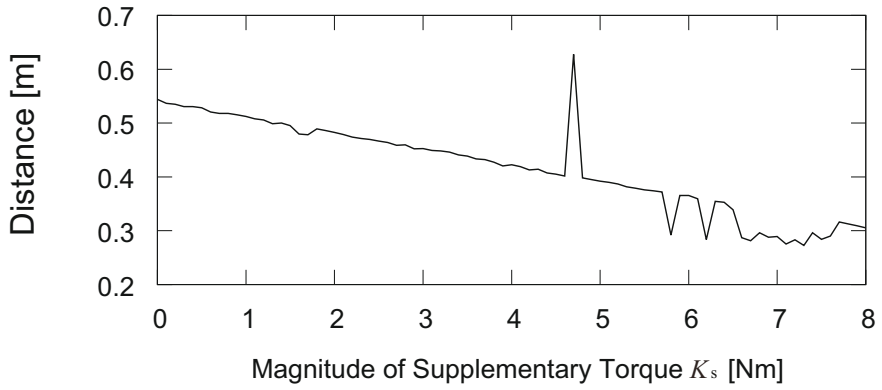


**Figure 2.13: Relationship of the magnitude of supplementary torque $K_s$ and the stability recovery distance $l$.**

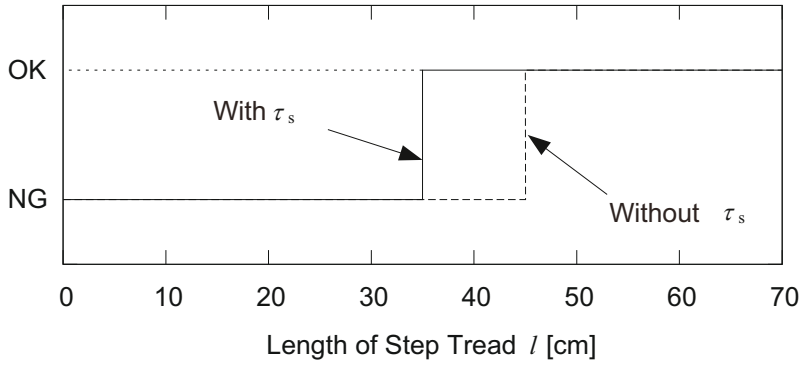


**Figure 2.14: Relationship of supplementary torque $\tau_s$ algorithm with the step tread.**

ered a cyclic motion. The climbing motion is stable if the robot can return to the original cycle trajectory even if the perturbation is included in the motion. This implies that the solution of $y(t)$ and the next periodic solution $y(t+\delta)$ on the same maneuver are near each other.

In this analysis, I define the Poincaré section $\Sigma$ as the state of the recurrence motion when the axle of the wheel is in line with the step corner as shown in Figure 2.15(a). Let $\boldsymbol{y}_k$ and $\boldsymbol{y}_{k+1}$ define the state vector of the robot in the Poincaré section $\Sigma$ at $k$-th and $k+1$-th step corner, respectively. By defining the function $\boldsymbol{L}(x)$ as the mapping function of the recurrence motion on the Poincaré section $\Sigma$, I can define the state vector of $\boldsymbol{y}_{k+1}$ as

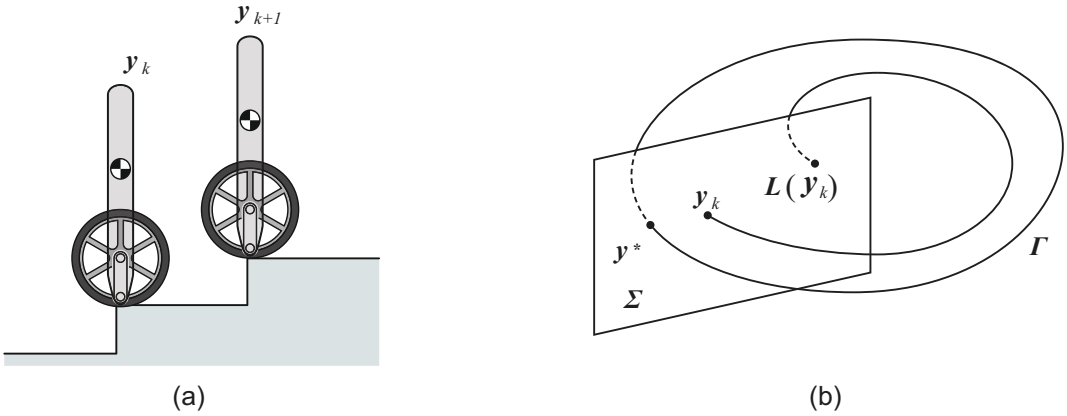


**Figure 2.15: (a) Considered state in limit cycle analysis and (b) Poincaré mapping.**

follows:

$$\boldsymbol{y}_{k+1} = \boldsymbol{L}(\boldsymbol{y}_k), \tag{2.72}$$

where $\boldsymbol{y} = \{\phi_1, \phi_3, \dot{\phi}_1, \dot{\phi}_2, \dot{\phi}_3\}$ denotes the state vector of the robot.

The limit cycle $\Gamma$ is defined as the whole step-climbing motion sequence where the trajectory of $\boldsymbol{y}_{k+1}$ will return near the vicinity of $\boldsymbol{y}_k$. For simplicity, I define the recurrence of the state vector $\boldsymbol{y}_k$ in the limit cycle $\Gamma$ at the Poincaré section $\Sigma$ as fixed point $\boldsymbol{y}^*$, which is shown in Figure 2.15(b). Thus, Equation (2.72) is expressed as follows:

$$\boldsymbol{y}^* = \boldsymbol{L}(\boldsymbol{y}^*). \tag{2.73}$$

The stability analysis of a limit cycle $\Gamma$ can be completed by perturbing $\Delta\boldsymbol{y}^*$ on a fixed point $\boldsymbol{y}^*$. The mapping function $\boldsymbol{L}$ with a perturbation $\Delta\boldsymbol{y}^*$ can be expressed using Taylor expansion series as follows:

$$\begin{aligned} \boldsymbol{L}(\boldsymbol{y}^* + \Delta\boldsymbol{y}^*) &= \boldsymbol{L}(\boldsymbol{y}^*) + \nabla\boldsymbol{L}\Delta\boldsymbol{y}^* \\ &\approx \boldsymbol{y}^* + \nabla\boldsymbol{L}\Delta\boldsymbol{y}^*, \end{aligned} \tag{2.74}$$

where $\nabla\boldsymbol{L}$ denotes the first-order partial derivatives of the mapping function $\boldsymbol{L}$. The cyclic mapping of $\boldsymbol{L}$ is considered as stable if the return map of the perturbed state converges

to the fixed point $\boldsymbol{y}^*$. This condition is mathematically satisfied by ensuring that the eigenvalues of $\nabla \boldsymbol{L}$ at fixed point $\boldsymbol{y}^*$ are strictly less than one. It is difficult to analytically obtain $\nabla \boldsymbol{L}$ and thus it is numerically obtained. To do so, we use a simulation of the robot climbing stairs composed of 25 steps with a width of 40 cm and a height of 12 cm. I use the same control parameter described in section 2.2.3 with the magnitude of the supplementary torque $K_s$ being 7.2 $Nm$.

The first step of the stability analysis is to determine the fixed point $\boldsymbol{y}^*$ of the stair-climbing motion in the simulation. From the simulation, I found that each value of the state vector of $\boldsymbol{y}_3$ and $\boldsymbol{y}_4$ are similar. Thus, I select the state vector of $\boldsymbol{y}_3$ as the fixed point $\boldsymbol{y}^*$. From the simulation, the $\boldsymbol{y}^*$ is obtained as follows:

$$\boldsymbol{y}^* = [0.118 \ -0.947 \ 1.160 \ -15.635 \ -2.554]^T. \tag{2.75}$$

The second step of the stability analysis is to perturb $\boldsymbol{y}^*$ to observe the mapping of the perturbed state $\boldsymbol{L}(\boldsymbol{y}^* + \Delta\boldsymbol{y}^*)$. Because I select the state vector of $\boldsymbol{y}_3$ as the fixed point, I add a small perturbation to the state of the robot when the axle of the wheel is in line with the third step corner. In one simulation, I add a small perturbation to a single state of $\boldsymbol{y}_3$. Because $\boldsymbol{y}^*$ consists of five states, I repeat this procedure five times to perturb each state. The perturbed state $\boldsymbol{L}(\boldsymbol{y}^* + \Delta\boldsymbol{y}^*)$ is obtained from the state vector of $\boldsymbol{y}_4$. Let $\Delta\boldsymbol{y}^* = [\Delta\phi_1 \Delta\phi_3 \Delta\dot{\phi}_1 \Delta\dot{\phi}_2 \Delta\dot{\phi}_3]$ where $\Delta\phi_1, \Delta\phi_3, \Delta\dot{\phi}_1, \Delta\dot{\phi}_2$, and $\Delta\dot{\phi}_3$ are the perturbation state variable $\phi_1, \phi_3, \dot{\phi}_1, \dot{\phi}_2$, and $\dot{\phi}_3$, respectively. I selected $\Delta\boldsymbol{y}^*$ that added in the simulation as $\Delta\boldsymbol{y}^* = [-0.5 \ -0.5 \ -0.5 \ -0.5 \ -0.5]$. To find $\nabla \boldsymbol{L}$ using this method, Equation (2.74) can be modified as follows:

$$\nabla \boldsymbol{L}\boldsymbol{\Omega} = \boldsymbol{\Psi}, \tag{2.76}$$

where

$$\boldsymbol{\Omega} = \Delta\boldsymbol{y}^* \boldsymbol{I}, \tag{2.77}$$

$\boldsymbol{I} \in \boldsymbol{R}^{5\times5}$ and $\boldsymbol{\Omega} \in \boldsymbol{R}^{5\times5}$ denote the identity matrix and perturbed matrix, respectively, in

which diagonal entries represent the perturbation of the state variables $\Delta \boldsymbol{y}^*$. The entry data of the $i$-th column of $\boldsymbol{\Psi} \in \boldsymbol{R}^{5\times5}$ represent the differences between the state vector $\boldsymbol{y}_3$ and $\boldsymbol{y}_4$ at the $i$-th simulation. For example, in the first simulation, I only perturb one state by adding the perturbation $\Delta\phi_1$ to state $\phi_1$. The entry data of the first column of $\boldsymbol{\Psi}$ represent the subtraction of $\boldsymbol{y}_4$ by $\boldsymbol{y}_3$ ($\boldsymbol{y}_4 - \boldsymbol{y}_3$) obtained from the first simulation. Assuming that $\boldsymbol{\Omega}$ is non-singular, $\nabla \boldsymbol{L}$ is obtained as $\nabla \boldsymbol{L} = \boldsymbol{\Psi}\boldsymbol{\Omega}^{-1}$. From the simulation, I obtain $\nabla \boldsymbol{L}$ as follows:

$$\nabla \boldsymbol{L} = \begin{bmatrix} 0.002 & 0.006 & 0.008 & 0.006 & 0.002 \\ -0.068 & -0.466 & -0.256 & -0.437 & -0.439 \\ 0.106 & 0.199 & 0.168 & 0.175 & 0.239 \\ -0.746 & -2.337 & -1.132 & -0.832 & -3.367 \\ 0.146 & 0.537 & 0.124 & 0.279 & 0.670 \end{bmatrix}, \tag{2.78}$$

with eigenvalues $\boldsymbol{\epsilon} = [-0.683 \; 0.396 \; 0.009 \; -0.09+0.059i \; -0.09-0.059i]^T$. The eigenvalues are plotted in Figure 2.16. Their absolute values correspond to 0.683, 0.396, 0.009, 0.597, and 0.597, which are less than 1. From these eigenvalues, I can conclude that the step-climbing motion cycle is stable because the finite perturbation along the state reduces to a zero perturbation in the first return map.

Using the same procedure, I performed stability analysis in the simulation without using the supplementary torque algorithm. The absolute eigenvalues correspond to 5.524, 1.151, 0.800, 0.047, and 0.009. Two of the absolute eigenvalues are greater than 1 and thus I can conclude that the simulation without the using of supplementary torque algorithm is unstable.

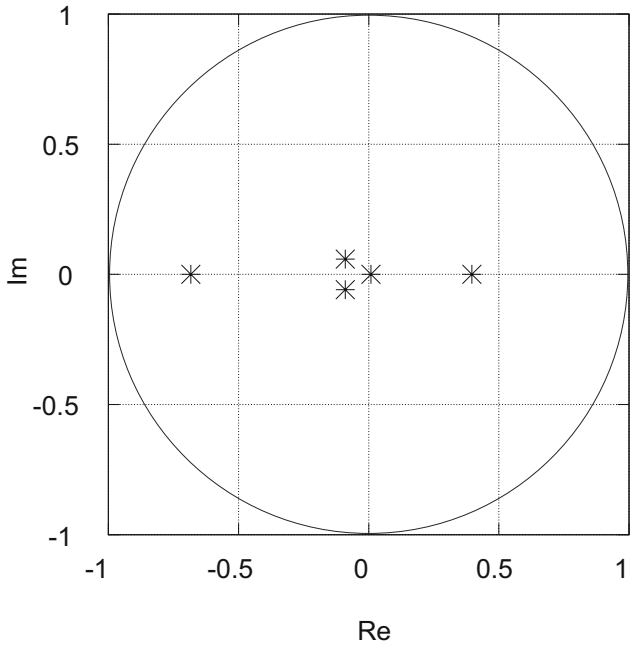


**Figure 2.16: Eigenvalues of $\nabla L$**

## 2.5 Experiment

### 2.5.1 Climbing Stairs with and without Supplementary Torque

This section presents the experimental results of the robot climbing the stairs. I conducted two experiments, with and without the supplementary torque $\tau_s$ algorithm, to verify the robot's performance in climbing the stairs. During the experiment, I used the same robot as that in [53], and it was made to climb a stair replica that consisted of four steps. The tread width and riser height of each step was 40 cm and 12 cm, respectively. Snapshots from the footage of the robot climbing the stair replica with and without $\tau_s$ are shown in Figures 2.17(a) and (b), respectively.

First, I discuss the experiment result of the robot climbing the stair with $\tau_s$ as shown in Figure 2.18(a). Figure 2.18(a1), (a2), (a3), and (a4) shows the motor torque $\tau_m$, body pitch angle $\phi_1$, pulley 1 velocity $\dot{\phi}_2$, and arm angle $\phi_3$, respectively, for the robot during the experiment.

Highlight I: It shows the states of the robot while attempting to climb the stairs. As shown in Figure 2.18(a1), the motor torque $\tau_m$ increased. Additionally, as shown in Figure

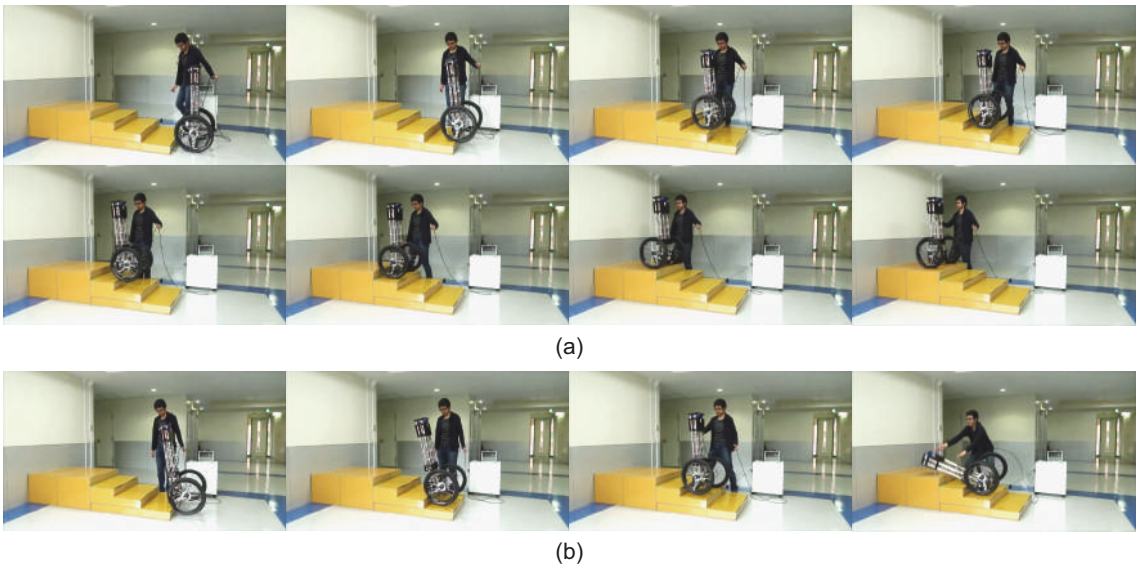

(a)

(b)

**Figure 2.17: Snapshots of the stair-climbing inverted pendulum robot ascending the stair**

2.18(a4), the arm lifts the body because the arm angle $\phi_3$ increases. Furthermore, notably, the body pitch angle $\phi_1$ is maintained at less than 0.15 rad as shown in Figure 2.18(a2). Therefore, it is possible to move the position of the COG without the occurrence of high tilting of the body.

Highlight II: It shows the application of the supplementary torque $\tau_s$ algorithm. During this period, $\tau_s$ is set to $K_s$ when the arm angle $\phi_3$ reaches the top threshold $\phi_t$. As shown in Figure 2.18(a1), an abrupt change is observed in the motor torque $\tau_m$. When the robot successfully climbs the step, $\phi_3$ returns to the initial condition until it reaches the bottom threshold $\phi_b$. At this point, $\tau_s$ was set to zero.

Highlight III: It shows the period of the robot when the body pitch angle $\phi_1$ and the arm angle $\phi_3$ return to the state prior to climbing the step. Fig 2.18(a) shows that the proposed control method enables the robot to climb the stair replica. The time required for climbing a single step is approximately 1.8 s.

Next, I discuss Figure 2.18(b) where (b1), (b2), (b3), and (b4) show comparisons of $\tau_m$, $\phi_1$, $\dot{\phi}_2$, and $\phi_3$, respectively, between the experiments with and without $\tau_s$. The dotted line denotes the experimental data without $\tau_s$. The results indicate that the robot successfully climbed two steps before it failed to climb the third step.

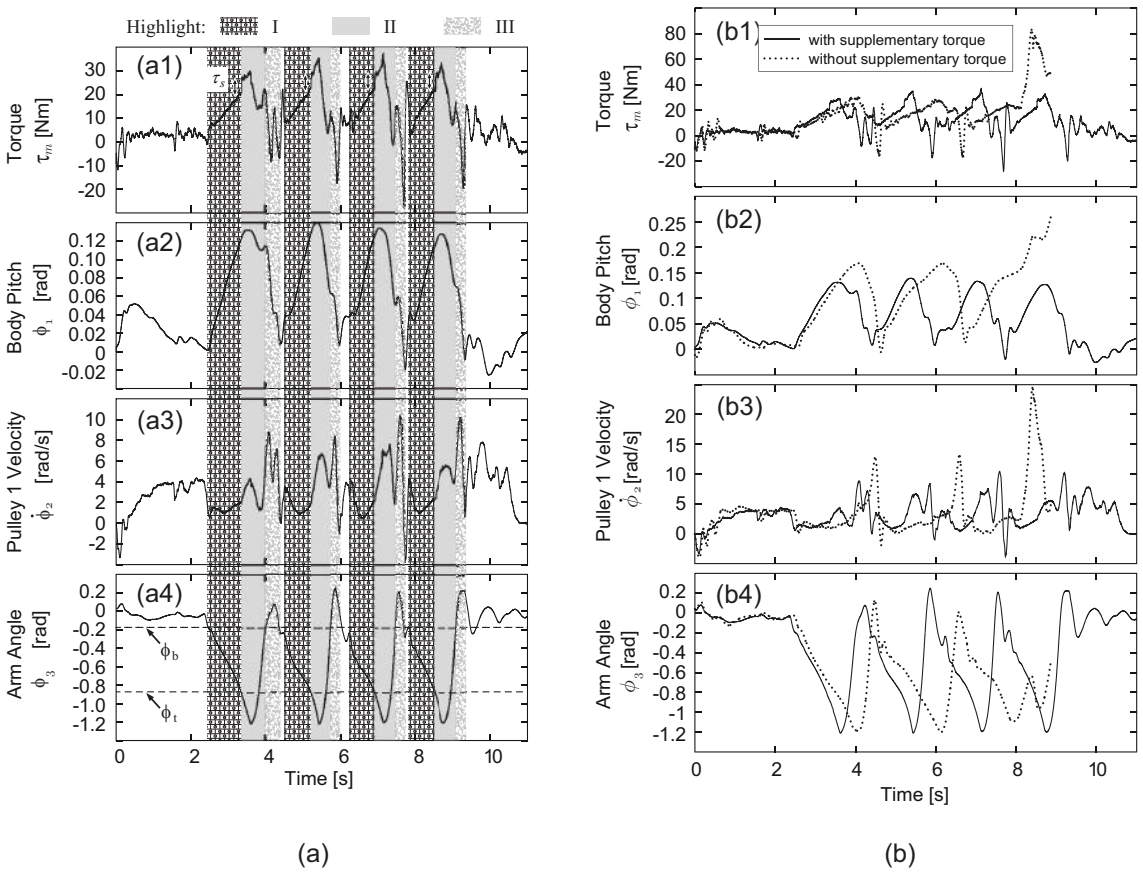


**Figure 2.18: Experimental results when the robot ascended the stair.**

From (b1), it is observed that the maximum torques $\tau_m$ during climbing are similar. Therefore, the arm lifts up the body as shown in (b4). However, as shown in (b2), the maximum body pitch $\phi_1$ without $\tau_s$ is 0.17 rad while it is 0.13 rad when $\tau_s$ is used.

In (b3) without $\tau_s$, the velocity $\dot{\phi}_2$ is higher than that during the experiment with $\tau_s$ because of the high inclination of the body pitch $\phi_1$ that remained after climbing, which caused the robot to move forward at a high speed. This condition caused the robot to bump toward the next step and this occasionally caused it to fall as shown when the robot climbed the second step.

As a reference, readers are invited to view the video of the experiment. This comparison indicates the effectiveness of the proposed supplementary torque $\tau_s$ approach for climbing narrow steps. The supplementary torque $\tau_s$ reduces the body pitch inclination while climbing and this reduces the needed space for stabilizing after climbing.

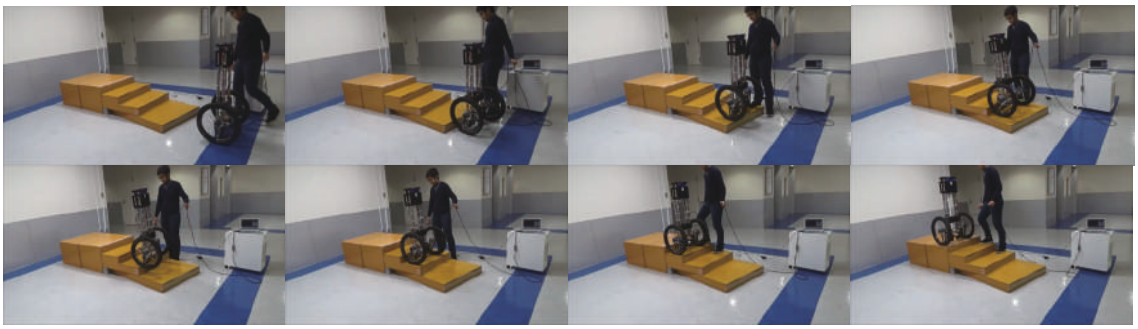

**Figure 2.19: The snapshots of the robot climbing a curved staircase.**

### 2.5.2 Climbing Curved Stairs

The inverted pendulum robot is required to ascend four steps with a curved staircase at the first two steps. The height of step riser is 12 cm. The snapshots of the robot climbing configuration of the staircase is shown in Figure 2.19.

The yellow and red highlights in Figures 2.20(a), (b), and (c) show the robot's condition when controlling its orientation angle and ascending the steps, respectively. As shown by the red highlights in Figures 2.20(a) and (b), the inclination and arm angle of the robot increased when the robot ascending the stair and return to its stable attitude after ascending it. This implies that the robot can manage to climb the curved staircase without losing its stability. As shown by the yellow highlights in Figure 2.20(c), the robot controlled its orientation, indicated by red line, to the desired orientation that is indicated by blue line. The desired orientation was obtained from the laser sensor installed in the robot. From this experiment, I can conclude that the robot can ascend the curved staircase with the proposed control method.

## 2.6 Concluding Remarks

This study presented the control of a two-wheeled stair-climbing motion for stabilizing the body while moving on a flat surface and achieving step-climbing motion. The control method is designed based on a state-feedback controller with a feed-forward constant. Although the control method is simple, it can stabilize the body and also achieve step-climbing motion. The effectiveness of control method is dependent on the control parameter. I used the dynamic model of the robot on a flat surface as an initial step

to determine the control parameter. The control parameter determined from the initial step must satisfy the compatible condition for climbing which is obtained from the static balance of the robot on a step. The supplementary torque algorithm is used to reduce the stability recovery distance. Numerical limit cycle analysis is performed to analyze the stability of the robot performing a step-climbing motion using the proposed control method. The result indicated that the step-climbing motion completed by the robot using the proposed control method is stable. Two experiments, with and without supplementary torque, were performed to verify the performance of the robot climbing the stairs. During the experiment without supplementary torque, the robot fell down after climbing two steps. In the experiment with supplementary torque, the robot successfully climbed four steps with the climbing rate of single step is approximately 1.8 s.

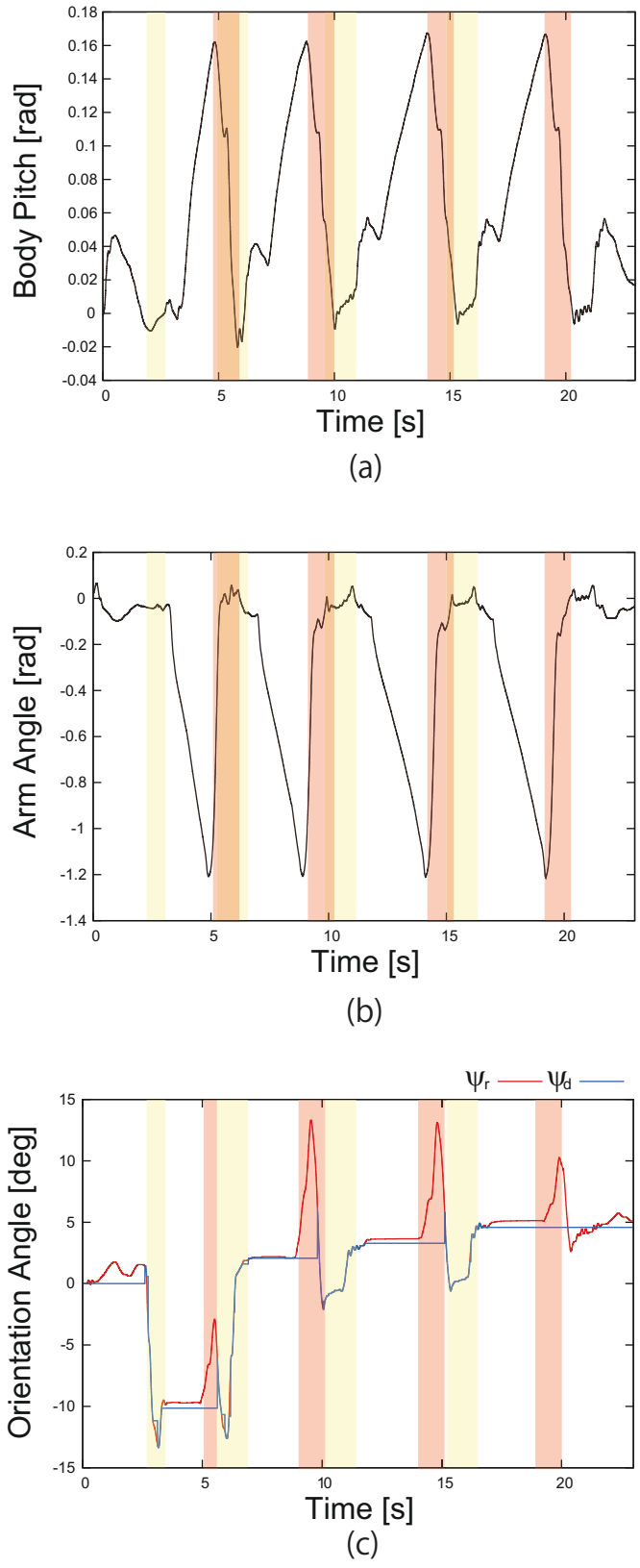


**Figure 2.20: Experimental results of (a) pitch angle, (b) arm angle, and (c) orientation angle of the robot climbing a curved staircase.**

# Chapter 3

# Development of a single-wheeled robot capable of climbing stairs

In this chapter, I explain the concept of the proposed stair-climbing robot using a single-wheeled inverted pendulum robot platform. The climbing mechanism is inspired by the mechanism used on a two-wheeled stair-climbing robot [53], which employed a wheel and an intermediate arm that enable the robot to climb stairs while maintaining a stable attitude. However, this climbing mechanism provides a lower ground clearance, which can influence the movement of the robot on a side slope. Therefore, I design the new configuration of a climbing mechanism for a single-wheeled inverted pendulum robot that provides a higher ground clearance.

Most of the stair-climbing robots require additional actuators to drive a dedicated mechanism for climbing stairs. So, I propose the use of a differential mechanism to drive the dedicated mechanism for climbing, using only a single actuator that drives the wheel of the robot. With this mechanism, the robot can self-distribute the torque, both on the wheel and intermediate arm, depends on the topography of the ground. Thus, the robot can automatically move the intermediate arm when climbing the step without using additional actuator and control method. The mechanism is simple, comprised of a belt-pulley mechanism and a harmonic drive. The mechanism offers advantages in reducing the cost of manufacturing, and also reducing the complexity of the structure and control method.

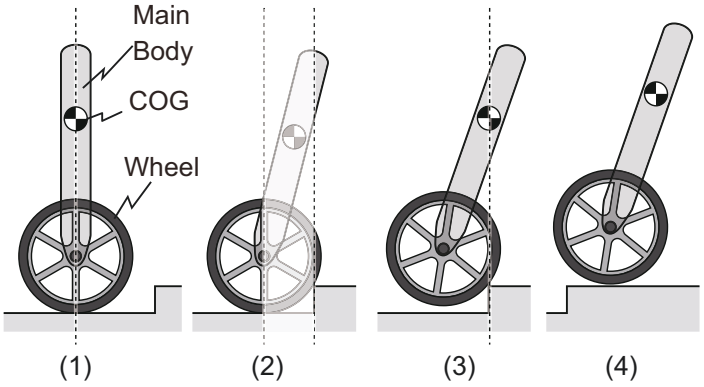


**Figure 3.1: The step-climbing behavior of a conventional inverted pendulum robot.**

## 3.1 Step-climbing motion of inverted pendulum robot

Takaki et al. [53] described the step-climbing behavior of an inverted pendulum robot. It consists of four stages, as described in Figure 3.1. The first stage is the behavior of moving on flat ground while maintaining stability. The method to achieve this behavior has been well-developed in recent years. The second stage is the condition where the wheel rotation is restricted at the base of the step. The third stage is the climbing condition where the wheel is lifting off from the base of the step. At this stage, the robot is required to incline in a specific configuration [44] for shifting its COG above the step corner to maintain a stable attitude while climbing. The fourth stage is the condition where the robot has to recover its stability after climbing. At this stage, in most of the cases, the robot fails to recover its stability because it inclines at a high angle during the third stage.

Takaki et al. [53] proposed a mechanism for shifting the COG of the robot using an intermediate arm. The proposed robot uses the arm to lift the main body towards a step corner. By lifting the main body using the arm, the robot can reduce the inclination angle before climbing, as shown in Figure 3.2(a). Thus, the robot can easily recover its stability after climbing a step, unlike the conventional inverted pendulum robot, which requires a high inclination angle for climbing, as shown in Figure 3.1. However, this configuration is not suitable for a single-wheeled robot because it has low ground clearance, as shown

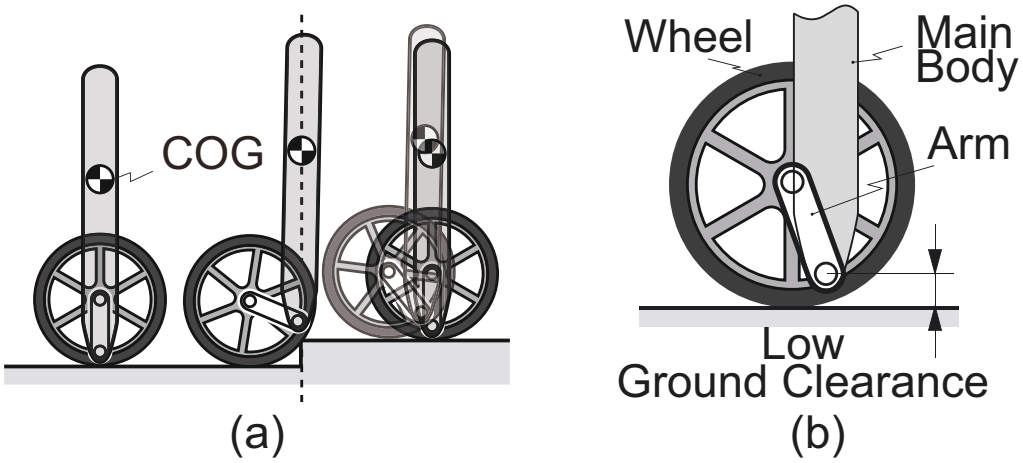


**Figure 3.2: The stair-climbing inverted pendulum robot proposed by Takaki et al.**

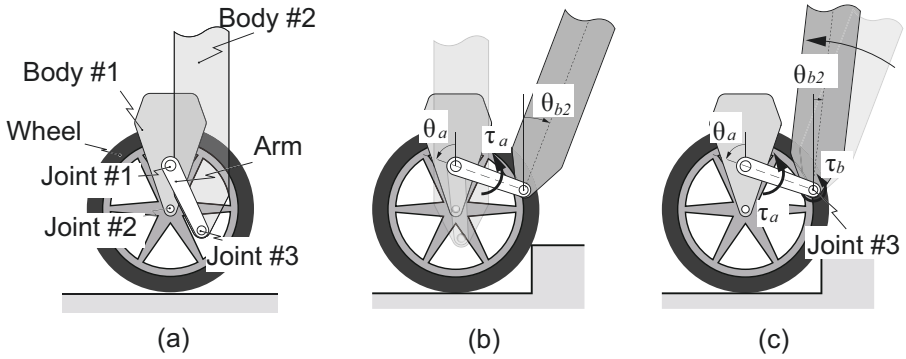


**Figure 3.3: Design of arm and body with a single arm.**

in Figure 3.2(b). Therefore, I design a new configuration of a robot with an intermediate arm that provides high ground clearance that is suitable for a single-wheeled robot. The configuration is discussed in detail in the next section.

## 3.2 The configuration of the robot with an intermediate arm

To provide high ground clearance, I consider the configuration of the robot shown in Figure 3.3(a), which consists of two bodies, a wheel, and a single intermediate arm.

This configuration provides high ground clearance because, unlike the previous robot [53], the arm joint (joint #1) is located higher than the wheel axle (joint #2). With this configuration, the robot requires at least two actuators to drive the wheel and the arm to realize the step-climbing motion. However, if the robot uses two actuators, the attitude of body #2 must be actively controlled by the motion of the arm because body #2 can rotate freely rotate on joint #3. This problem is similar to the pendubot control problem, which can be resolved by using a linear state-feedback controller [56].

Here, I consider the motion of the robot while lifting body #2, as shown in Figure 3.3(b). According to Sponge et al. [56], as the arm angle $\theta_a$ approaches $(1/2)\pi$, controlling body #2's attitude becomes more difficult because the balancing range of body #2 is reduced. Therefore, the possibility of body #2 rotating at joint #3 is increasing while the arm is lifting it. The simple method to cope with this problem is by installing the actuator to control the attitude of body #2, as shown in Figure 3.3(c). However, this increases the complexity of the robot's structure and its manufacturing cost

To solve the previous problem I consider the use of two arms, with an identical length of $L_a$, to form a single-parallelogram linkage between bodies #1 and #2, as shown in Figure 3.4(a). Arm #1 is driven by the actuator to lift body #2, as shown in Figure 3.4(b). Arm #2 is a passive arm which connects two revolute joints, joint #2 and joint #4, on bodies #1 and #2, respectively. The lengths between arm joints, $L_p$, in bodies #1 and #2 are identical. With this configuration, the robot does not require the additional regulatory control or actuator to control body #2 ' s attitude because it is not possible to rotate freely on joint #3. However, this arm configuration has singularity when arm #1 and arm #2 are aligned. Here, I consider a problem where the robot with a singularity configuration is inclining as shown in Figure 3.4(c). Because the robot has a tall dimension, the COG of body #2 is considered high. Thus, when the robot is slightly inclining, gravitational force can cause body #2 to rotate at joint #4. To understand this problem, I consider the torque equilibrium of body #2 with joint #4 as a pivot point, as shown in Figure 3.4(d). The torque acted on body #2 $\tau_b$, with joint #4 as a pivot point, is obtained from static torque

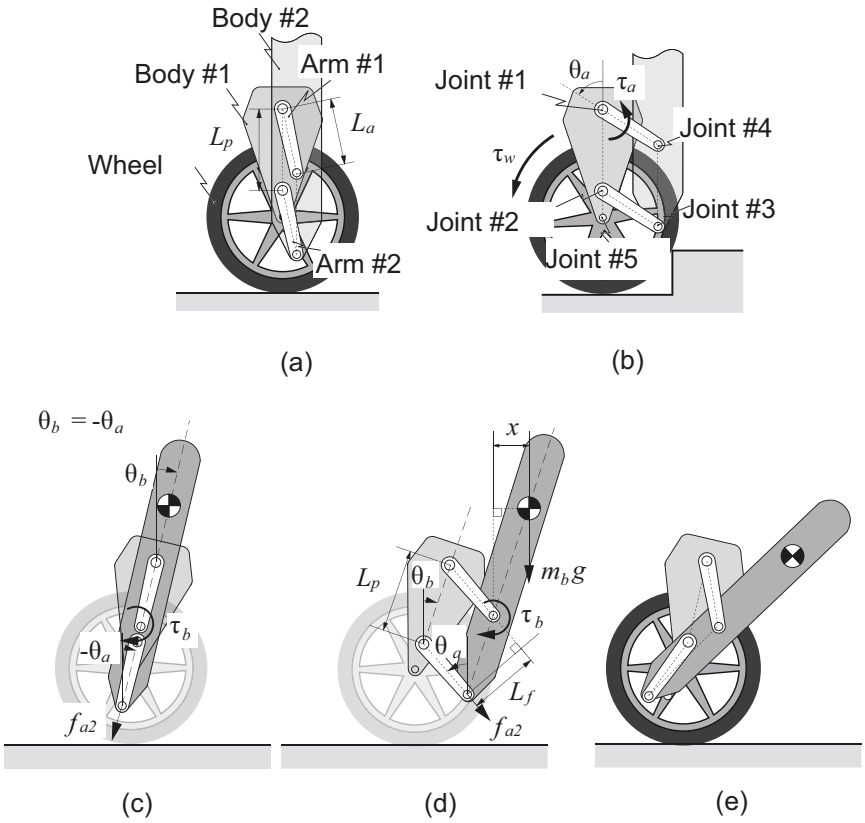


**Figure 3.4: Design of arm and body with two arms.**

analysis as follows:

$$\tau_b = m_b g x - f_{a2} L_f, \tag{3.1}$$

where, $m_b$, $g$, and $x$ denote the mass of body #2, the gravity acceleration, and the moment arm of the gravitational force applied on body #2, respectively, and $f_{a2}$ and $L_f$ denote the internal force on joint #3 and the moment arm of $f_{a2}$, respectively. The moment arm $L_f$ is defined as $L_f = -L_p \sin(\theta_a + \theta_b)$, where angle $\theta_a$ and $\theta_b$ denote the arm angle and inclination angle of the robot, respectively. From the definition, in the case where the

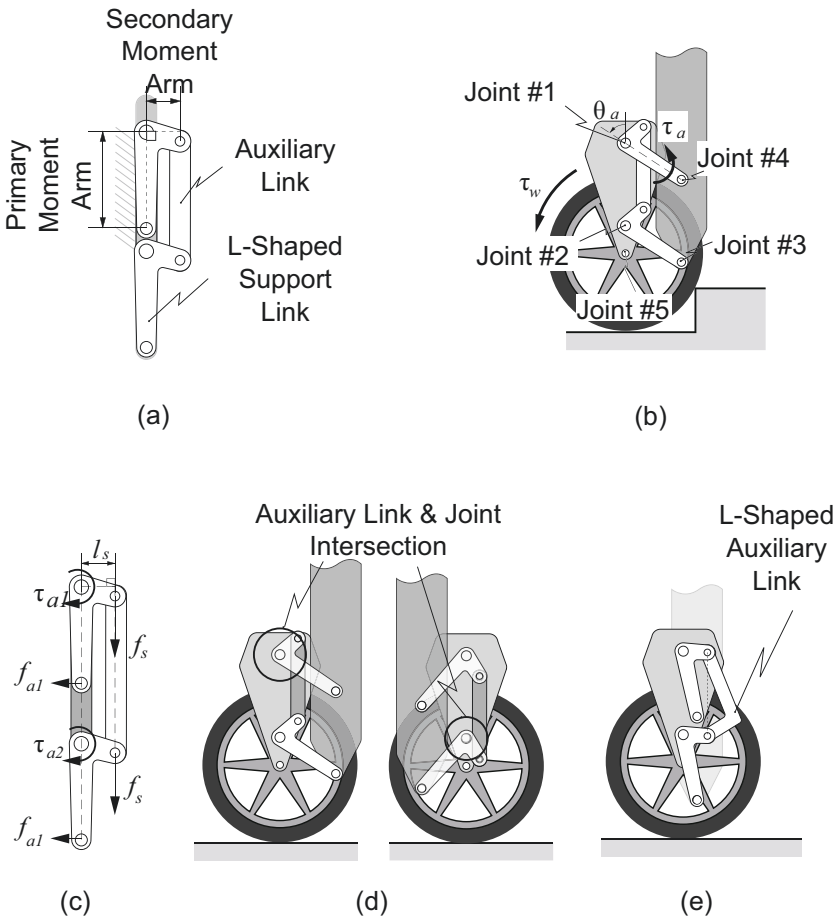


**Figure 3.5: Design of arm and body with two L-shaped arms and auxiliary link.**

robot is inclining, as shown in Figure 3.4(c), the moment arm $L_f$ becomes zero because $\theta_a$ is equal to $-\theta_b$. In this case, body #2 can rotate on joint #4 because $f_a$ cannot provide the support to counter the torque induced by the gravitational force on body #2. If this problem emerges, the configuration of the parallelogram linkage can change into an anti-parallelogram, as shown in Figure 3.4(e).

To address this problem I consider modifying the arm configuration into a double-parallel-linkage configuration. Here, I modify the shape of arm #1 and arm #2 into an L-shaped arm, which provides two moment arms perpendicular to each other. The form of a double-parallel-linkage configuration can be constructed by connecting the secondary moment arm, in both arms, with the auxiliary link, as shown in Figure 3.5(a). Figure

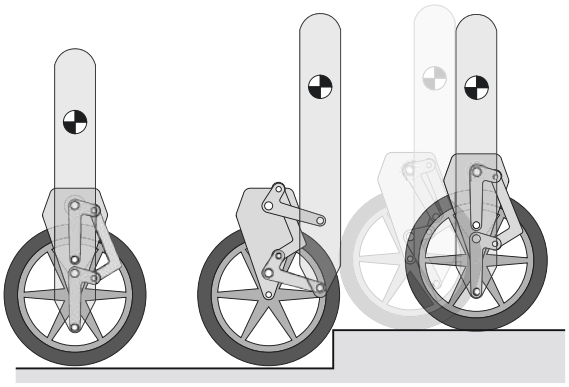

**Figure 3.6: Climbing motion using proposed arm configuration.**

3.5(b) shows the robot configuration with a double parallel linkage arm. With this configuration, the rotations of arm #1 and arm #2 are always synchronous though they are not aligned. This is because the auxiliary link can provide a torque distribution on both arms when the primary moment arms on both arms are aligned, as shown in Figure 3.5(c). Therefore, the arm and body configuration can be maintained in a parallel configuration.

The arm configuration with an auxiliary link has a limited rotation range because, as shown in Figure 3.5(d), the auxiliary link intersects with joint #1 or joint #2. This problem may cause the auxiliary link to hit the shaft on joint #1 and joint #2. To increase the rotation range of the arm configuration, I modified the shape of the auxiliary link into an L-shaped support link, as shown in Figure 3.5(e).

The motion of the robot climbing a step using the proposed parallel arm linkage configuration is shown in Figure 3.6. With this configuration, the robot is required to drive the wheel and the parallel arm to achieve a step-climbing motion. If the robot utilizes two actuators for driving the wheel and the parallel arm, the robot becomes more complex and expensive. To overcome this problem, I propose a driving mechanism in which a single actuator can drive both the wheel and the parallel arm to achieve a step-climbing motion. The structure of the proposed driving mechanism applied to the robot will be discussed in section 3.3.

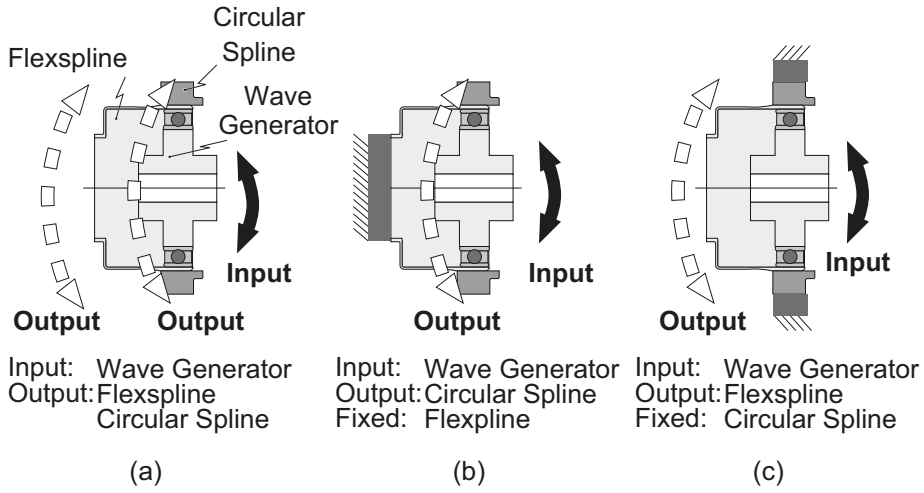


**Figure 3.7: The three operation modes of a harmonic drive.**

## 3.3 Differential driving mechanism

The differential mechanism can resolve one input into two outputs by maintaining the balance of applied force or torque, depending on the external constraints and loads [57]. Based on this terminology, I design the proposed driving mechanism using the differential mechanism for driving the wheel and parallel arm with a single actuator. Next, I describe the structure and design of the proposed driving mechanism using the differential mechanism.

### 3.3.1 Structure of driving mechanism

The proposed driving mechanism uses the harmonic drive as the primary component of the differential mechanism in a gear-based form. The harmonic drive consists of three input/output ports: the wave generator, the flex spline, and the circular spline as shown in Figure 3.7. In the proposed driving mechanism, the differential mechanism is constructed by configuring the harmonic drive as a floating differential gearing with the wave generator as the input port, and the flex spline and circular spline as the output ports. With this configuration, the harmonic drive has three operation modes [58] as shown in Figure 3.7.

Figure 3.8 shows the composition diagram of the proposed driving mechanism.

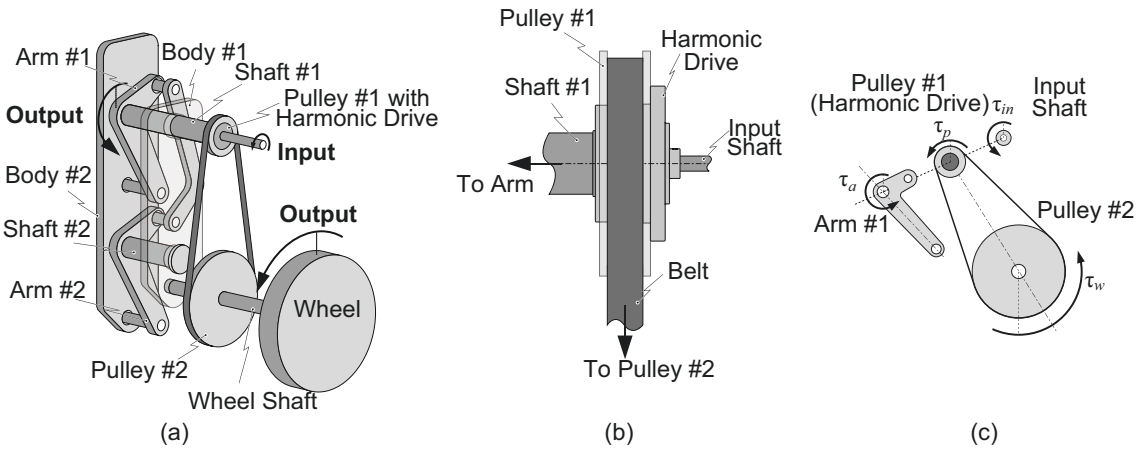


**Figure 3.8: Proposed mechanism.**

Arms #1 and #2 are attached on shafts #1 and #2, respectively. Pulley #1 is attached to the wheel, and they are both mounted on the wheel shaft. The belt is used to transmit the power from pulley #1 to pulley #2. All shafts are mounted on the frame of body #1.

Figure 3.8(b) shows the power transmission configuration using harmonic drive as a floating differential gearing. In the proposed driving mechanism, I define the input shaft as the input, and the parallel arm and wheel as the outputs. The input shaft is installed on the wave generator port to provide the power input. Shaft #1 and pulley #1 are attached to the flex spline and circular spline ports, respectively. This configuration enables the harmonic drive to transmit the power from the input shaft to the two outputs, which are the parallel arm and wheel.

The actual motion of the proposed driving mechanism is explained as follows:

**Driving the wheel on a flat surface:** Figure 3.9(a) shows the motion of the robot moving on a flat surface. I assume that body #2, which is mounted on the parallel arm, is heavy. Thus, the robot requires a high input torque, $\tau_{in}$, to lift body #2. However, when the body has a low inclination, the input torque, $\tau_{in}$, required for maintaining a stable attitude is lower compared to the input torque required for lifting body #2. Under this condition, with the low input torque $\tau_{in}$, the robot can maintain a stable attitude by driving its wheel without moving the parallel arm to lift body #2. This condition corresponds to the operation mode of the harmonic drive with the fixed flex spline, as shown in Figure 3.7(b). Therefore, in this driving mode, the input torque $\tau_{in}$ from the input shaft is transmitted to

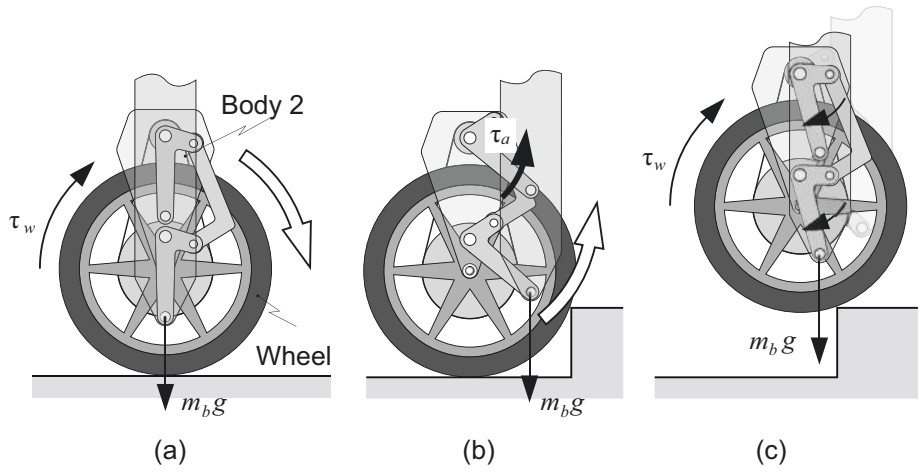


**Figure 3.9: Motion of the proposed mechanism.**

the circular spline for driving the wheel.

**Driving the parallel arm at the base of the step:** Figure 3.9(b) shows the motion of the robot when the wheel contacts the step riser. Under this condition the wheel rotation is constrained by the step. I assume that the $\tau_{in}$ for rotating the wheel to climb the step is higher than the $\tau_{in}$ for lifting body #2. Because the wheel rotation is constrained, it is possible for $\tau_{in}$ to increase without rotating the wheel. As $\tau_{in}$ increases, the parallel arm can rotate to lift body #2. This condition corresponds to the operation mode of the harmonic drive with the fixed circular spline, as shown in Figure 3.7(c). Therefore, in this driving mode, the input torque $\tau_{in}$ from the input shaft is transmitted to the flex spline for driving the arm.

**Climbing a step and recovering stability:** Figure 3.9(c) shows the motion of the robot when it climbs a step and recovers stability after climbing. Under this condition, $\tau_{in}$ tends to drive the wheel to climb over the step than driving the parallel arm to lift the body. This tendency is because $\tau_{in}$ is already sufficient to rotate the wheel over the step, and the required torque for lifting body #2 to a higher angle is higher compared with the required torque for rotating the wheel over the step. This condition corresponds to the operation mode of the harmonic drive with the fixed flex spline, as shown in Figure 3.7(b). Because the parallel arm has already lifted the body before climbing the step, the gravitational force on body #2 pulls the parallel arm, reducing its angle, which returns to

its original position as driving on a flat surface.

By considering these three behaviors, the proposed mechanism can realize the step-climbing motion illustrated in Figure 3.6 by using a single actuator. This also introduces terrain adaptability because the robot can drive either the parallel arm or wheel according to the topography of the ground. In conclusion, the proposed driving mechanism reduces not only the manufacturing cost and complexity of the structure but also the complexity of the controller.

### 3.3.2 Design concept for determining the motor and reduction ratio of the harmonic drive and wheel pulley

The input torque $\tau_{in}$ and the torque transmission between the input shaft, wheel, and parallel arm are essential factors in designing the proposed driving mechanism to achieve step-climbing. They must be designed by determining a compatible motor torque and reduction ratio of the harmonic drive and wheel pulley. In order to do this, I consider the torque balance among the input shaft, wheel, and parallel arm. As shown in Figure 3.8(c), $\tau_a$, $\tau_{in}$, $\tau_p$ and $\tau_w$ denote the torque of the parallel arm, input shaft, pulley #1, and wheel, respectively. Because the torque from pulley #1 is transmitted to the wheel via the belt-pulley system, $\tau_w$ is defined as $\tau_w = R_w\tau_p$, where $R_w$ denotes the reduction ratio of wheel pulley. With the harmonic drive as a floating differential gearing, according to the manufacturer's literature [58], the relationships between $\tau_{in}$, $\tau_a$, and $\tau_w$ is given as follows:

$$\tau_{in} = -\frac{\tau_a}{R_h} = \frac{\tau_p}{R_h + 1} = \frac{\tau_w}{R_w(R_h + 1)}, \tag{3.2}$$

where $R_h$ denotes the reduction ratio of harmonic drive.

I consider two necessary parameters for determining the motor, harmonic drive, and reduction ratio of the wheel pulley, the minimum motor torque required for lifting the body using the parallel arm $\tau_a^{min}$ and for rotating the wheel over the step $\tau_w^{min}$. The descriptions of these two parameters are as follows:

**Minimum required torque for lifting the body using the parallel arm:** Figure

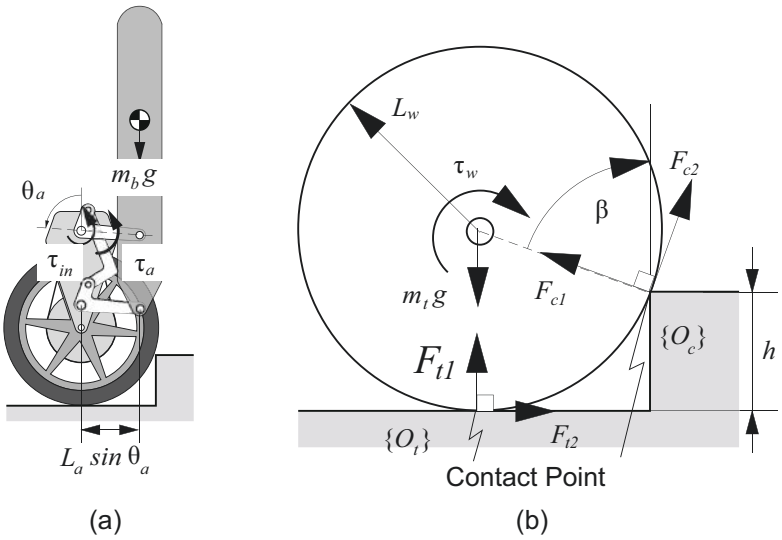


**Figure 3.10: Motion considered for determining the minimum motor torque and reduction ratio of the harmonic drive and wheel pulley.**

3.10(a) shows the free body diagram of the robot when lifting the body. From the static torque equilibrium analysis, the relationship between the torque of the parallel arm $\tau_a$ and the arm angle $\theta_a$ for lifting the body is as follows:

$$\tau_a = m_b g L_a \sin(\theta_a), \tag{3.3}$$

where $m_b, g$, and $L_a$ denote the mass of body #2, gravity acceleration, and length of the arm, respectively.

I define the parameter $\tau_a^{min}$ as the minimum required torque of motor $\tau_{in}$ to rotate the parallel arm at $(1/2)\pi$. This is because the horizontal displacement of body #2 is at maximum when $\theta_a$ equals $(1/2)\pi$. I can also consider $\tau_w$ and $\tau_p$ as zero because the step restrains the rotation of the wheel. Therefore by considering Equation (3.2) and Equation (3.3), I obtain $\tau_a^{min}$ as follows:

$$\tau_a^{min} = \frac{m_b g L_a}{R_h}. \tag{3.4}$$

**Minimum required torque for the wheel to climb a step:** Figure 3.10(b) shows

a free body diagram of the wheel when encountering a step. It has two contact points, $O_c$ and $O_t$, at the corner and at the tread of the step, respectively. According to the free body diagram of the wheel shown in Figure 3.10(b), there are five forces acting on the wheel: the gravitational force that acts on the axle of the wheel, two normal forces $F_{c1}$ and $F_{t1}$ on contact points $O_c$ and $O_t$, respectively, and two tangential forces $F_{c2}$ and $F_{t2}$ resulting from the traction forces on contact points $O_c$ and $O_t$, respectively. Under a static condition, the force equilibrium of the wheel with projections of $f_{c1}$ and $f_{c2}$ are expressed as follows:

$$F_{t1}\cos\beta - F_{t2}\sin\beta + F_{c1} - m_t g\cos\beta = 0, \tag{3.5}$$

$$F_{t1}\sin\beta + F_{t2}\cos\beta + F_{c2} - m_t g\sin\beta = 0, \tag{3.6}$$

where $m_t$ and $g$ are the total mass of the robot and the gravity acceleration, respectively.

The relationship of the wheel torque $\tau_w$, $F_{c2}$, and $F_{t2}$ under a static condition is obtained as follows:

$$\tau_w = (F_{t2} + F_{c2})L_w. \tag{3.7}$$

According to Figure 3.10(b), angle $\beta$ has a relationship with the height of the step riser $h$ and the radius of a wheel $L_w$ as follows:

$$\sin\beta = \frac{1}{L_w}\sqrt{2L_w h - h^2}. \tag{3.8}$$

Here, $\tau_w^{min}$ is considered to be the minimum motor torque $\tau_{in}$ to rotate the wheel just before the wheel lifts off from the tread of a step. In this case, I consider the condition when the contact point $O_t$ becomes unavailable, where $F_{t1}$ and $F_{t2}$ can be considered as equal to zero [59]. Therefore, from Equations (3.5)-(3.7), $F_{c1}$, $F_{c2}$, and $\tau_w$ when the wheel starts to lift off from the tread of the step are obtained as follows:

$$F_{c1} = m_t g \cos\beta, \tag{3.9}$$

$$F_{c2} = m_t g \sin\beta, \tag{3.10}$$

$$\tau_w = L_w F_{c2} = L_w m_t g \sin\beta. \tag{3.11}$$

To obtain $\tau_w^{min}$, I assume that the axis of rotation of the wheel while climbing over a step is located at $O_c$. This assumption holds if no slippage occurs at the contact point $O_c$. The condition to ensure that the wheel is climbing over a step without slip is given as follows:

$$F_{c2} < \mu_s F_{c1}, \tag{3.12}$$

where $\mu_s$ is the static friction coefficient between the wheel and corner of the step. I assume that $\mu_s$ is high enough to satisfy the condition where the wheel is able to climb over a step without slip. If the no-slip condition can be satisfied, I can obtain $\tau_w^{min}$ by considering Equations (3.2), (3.8), and (3.11), as follows:

$$\tau_w^{min} = \frac{m_t g \sqrt{2L_w h - h^2}}{R_w(R_h + 1)}. \tag{3.13}$$

The concept for designing the proposed driving mechanism consists of two steps. The first step is determining the torque of the motor and reduction ratio of the harmonic drive. This is because the options of the motor torque and harmonic drive reduction ratio are limited. They can be determined by considering the minimum required torque for lifting the body $\tau_a^{min}$.

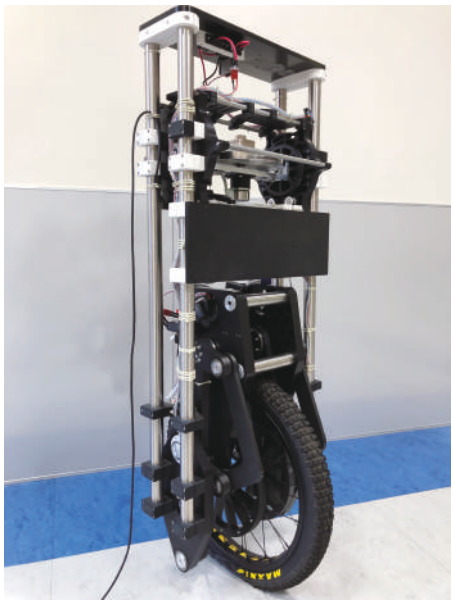

**Figure 3.11: Robot prototype.**

The second step is adjusting the reduction ratio of the wheel pulley based on the selection of the motor torque and the reduction ratio of the harmonic drive. A ratio which ensures that the motor torque satisfies the minimum required torque for rotating the wheel lift-off from the step, $\tau_w^{min}$, must be determined.

## 3.4 Single-wheeled stair-climbing robot prototype

This section describes the prototype robot developed by the authors. The robot is equipped with control moment gyroscope and differential driving mechanism. The following is the description of a control moment gyroscope and the differential driving mechanism equipped in the robot, including the integration of both mechanism in the robot.

### 3.4.1 Control moment gyroscope

The developed robot is equipped with a control moment gyroscope as the roll balance mechanism to produce the lateral balancing torque. Because I are considering the robot to be heavy, I prefer to use this mechanism over an inertial-wheel-based mechanism.

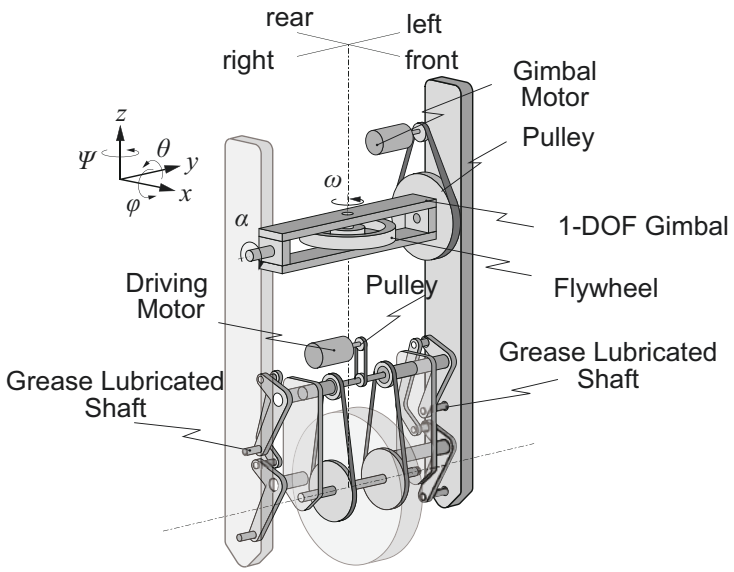


**Figure 3.12: Coordinate system.**

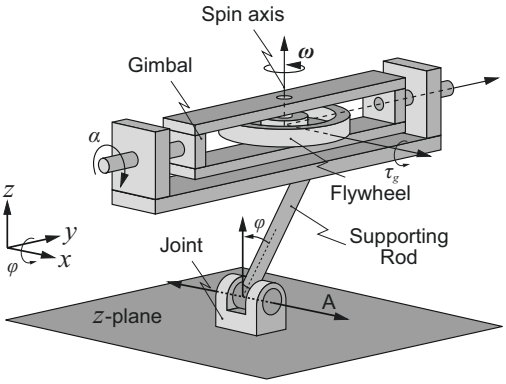


**Figure 3.13: Single gimbal control moment gyroscope concept**

This is because the required torque for spinning the gyroscope and tilting the gimbal to produce balancing torque is lower compared with the inertial-wheel-based balance mechanism [41]. The balancing torque within the inertial-wheel-based balance mechanism depends on the rotational acceleration of the inertial wheel. Thus, if the robot is heavy, the motor torque to drive the inertial wheel must be high.

The control moment gyroscope consists of gimbal frame and spinning flywheel that can be used for generating gyroscopic torque. The gyroscopic torque is generated by the gyroscope precession. The gyroscope precession is a change in the orientation of the

spinning flywheel axis. The relationship between gyroscopic torque $\tau_g$ with the rate of precession angle $\dot{\alpha}$ is governed by the equation as follows.

$$\tau_g = I\omega \times \dot{\alpha}, \tag{3.14}$$

where, $I$ is the moment inertia of spinning flywheel with respect of the spin axis and $\omega$ is the flywheel spinning rate.

The gyroscopic torque yields by control moment gyroscope can be used for balancing mechanism in one direction by using single gimbal to rotate the spinning flywheel [39, 41]. In order to easily understand the concept of balancing, for example, the gyroscope platform with supported rod is mounted on hinge joint that is fixed on plane-$z$ as shown in Figure 3.13. By using this configuration, the gyroscope platform cannot move on longitudinal axis (pitch motion). Additionally, the spinning flywheel rotates on $z$-axis at a rate of $\omega$ and it is mounted on a gimbal that allows the rotation $\alpha$ on $y$-axis. The gyroscope platform can achieve the lateral balance (roll balance) by maintaining the COG of gyroscope platform at above its pivot point. (axis-A). When the platform is slightly inclined, the COG will be displaced from above axis-A, and thus the gravitational torque will act on the platform that inducing the rolling motion. To address the rolling motion on the platform, the gyroscopic torque acting on opposite direction of rolling motion must be generated as below. If the platform lean to the right, the opposing gyroscopic torque is generated by rotating the gimbal clockwise, and if the platform lean to the left, the opposing gyroscope torque is generated by rotating the gimbal counter clockwise. By rotating the spinning flywheel at a sufficient precession rate $\dot{\alpha}$ on $y$-axis, the opposing torque will be sufficient to counter the gravitational torque, and thus the COG of the platform can be returned back to above its pivot point.

The aforementioned concept is adopted in the robot to realize the lateral balance. By assuming that the longitudinal balance is achieved by the wheel driving mechanism, the control moment gyroscope is employed to achieve the lateral balance of the robot.

Figure 3.12 shows the configuration of the control moment gyroscope (CMG) used in the robot. The CMG uses a single degree of freedom (DOF) gimbal that can rotate on

the $y$-axis to provide a precession angle and precession rate of the spinning flywheel. The specification of the CMG is as follows: It uses a flywheel with a mass of 1.78 kg. The diameter and thickness of the flywheel are 199 mm and 16 mm, respectively. The moment of inertia of the spinning flywheel at the spinning axis ($z$-axis) calculated by Computer Aided Design (CAD) is $1.07 \times 10^{-2}$m$^2$kg. The flywheel is driven by a 70 W brushless motor (Maxon, EC-45 flat). The 180 W brushless motor (Maxon, EC-i52), with a torque constant $K$ of 70.6 mNm/A, is used as a gimbal motor. The torque from the gimbal motor is transmitted to drive the gimbal through a belt-pulley system with a reduction ratio of 6:1.

### 3.4.2 Implementation of differential driving mechanism

The structure of the robot consists of two bodies (body #1 and body #2), a pair of parallel arms, and a wheel. A pair of the parallel arms on the left and right side is used to lift the body to provide the structural support on both the left and right sides of body #2. This design is preferable because it can prevent the rotational twisting of body #2. To reduce the swinging motion of both arms when the robot drives on a flat surface (i.e., both arms at low point), a highly viscous grease (Shin-Etsu, G-330) is applied on two shafts, as shown in Figure 3.12. The grease is applied on both shafts to increase the damping coefficient for moving both arms. From the experiment, the grease is determined to have a damping coefficient of 0.002 Nms/rad.

Figure 3.12 shows the configuration of a pair of differential driving mechanisms installed in the robot. A pair of differential driving mechanisms with serially connected inputs is used to drive the wheel and a pair of the parallel arms. A single input shaft is used to connect the wave generators on both differential driving mechanisms serially. This design provides a synchronous movement of the parallel arms on both the left and right sides to prevent rotational twist of body #2. A motor is used to provide the power to the drive mechanism. A pair of driving mechanisms obtain the power from the motor through the belt-pulley system with a reduction ratio of 1. The outputs for driving the wheel from both mechanisms are serially connected by attaching a pair of pulleys (pulleys #2) on the

left and right sides of the wheel.

### 3.4.3 Mechanism integration and system structure

The prototype of the developed single-wheeled robot is shown in Figure 3.11. The control moment gyroscope is mounted on body #2, as shown in Figure 3.12. The dimensions of the robot are 1.22 m in height and 0.45 m in width. The lengths of the arms $L_a$ and the length between the joint in body #1 and #2 $L_p$ are 200 mm and 250 mm, respectively. The size of the wheel (Creepy Crawler, Maxis) is 20x2.0 inches (508x50.8 mm). Table 3.1 describes the masses of each component obtained from CAD software. The coordinate system of the robot is shown in Figure 3.12. The origin of the local coordinate system is located at the center of the wheel shaft. The local coordinates of the COGs of respective parts obtained from CAD software are listed in table 3.2.

A 180 W brushless motor (Maxon, EC-i52) is used as the power source of the differential driving mechanism. All motors (gimbal, flywheel, and differential driving mechanism motors) are controlled by a servo controller (Maxon, ESCON 70/10) that can provide current up to 30 A. Two harmonic drives (Harmonic Drive, CSG-14-50-2UH) are used as the transmission system that enable differential driving mechanism. The reduction ratio of the harmonic drive $R_h$ is 50. The reduction ratio of the wheel (between pulley #1 and pulley #2) $R_w$ is 3. The configuration of the motor, servo controller, and reduction ratios ($R_h$ and $R_w$) in the prototype robot is sufficient to satisfy the minimum required torque $\tau_a^{min}$ and $\tau_w^{min}$, described in section 3.3, for climbing a step with a height up to 20 cm.

The robot is equipped with 2 lithium polymer batteries (Kypom, 35 C) to supply the electrical power for the electronic system. The 9-axis inertial measurement unit (Lp Research, LPMS-CU2) is mounted in the robot to measure the pitch and roll attitude. The robot uses encoders to measure the angle of the arm, gimbal, and wheel. The measurement signals from all encoders is processed by two microcontrollers (Renesas, SH2-7047F). The measurement data from the microcontrollers and Inertial Measurement Unit (IMU) are transmitted to an external laptop computer, by Controller Area Network (CAN)

**Table 3.1: Mass Properties.**

| Parts | Mass [kg] |
|---|---|
| Body 1 | 8.0 |
| Body 2 + CMG | 14.6 |
| Arm 1 Left, Right | 0.2 |
| Arm 2 Arm Left, Right | 0.2 |
| Support Link Left, Right | 0.1 |
| Wheel | 1.7 |
| Total Mass | 25.3 |

**Table 3.2: Local coordinates of COGs of each part (when pitch angle of main body $\theta = 0$ and arm angle $\theta_a = 0$).**

| Parts | (x,y,z) [mm] |
|---|---|
| Wheel | (0,0,0) |
| Body 1 | (16, -6, 250) |
| Body 2 | (-4, 7, 488) |
| Arm 1 Right | (18, -123, 250) |
| Arm 2 Right | (18, -123, 1) |
| Support Link Right | (105, -94, 157) |
| Arm 1 Left | (18, 123, 250) |
| Arm 2 Left | (18, 123, 1) |
| Support Link Left | (105, 94, 157) |

bus transmission, for computations for controlling the robot. The output from the result of computational processing is also transmitted by CAN bus transmission to microcontrollers, which further transmit the signal to the servo controller (Maxon, ESCON 70/10) for controlling all motors. All hardware other than the external computer is installed in the robot.

## 3.5 Dynamic model

### 3.5.1 Longitudinal dynamics

The robot consists of five rigid bodies, namely arm 1, arm 2, body 1, body 2, and wheel, as shown in Figure 3.14. To fully describe the motion, I use the same method as I describe the dynamics of two-wheeled robot in chapter 2. First, the dynamics of the robot

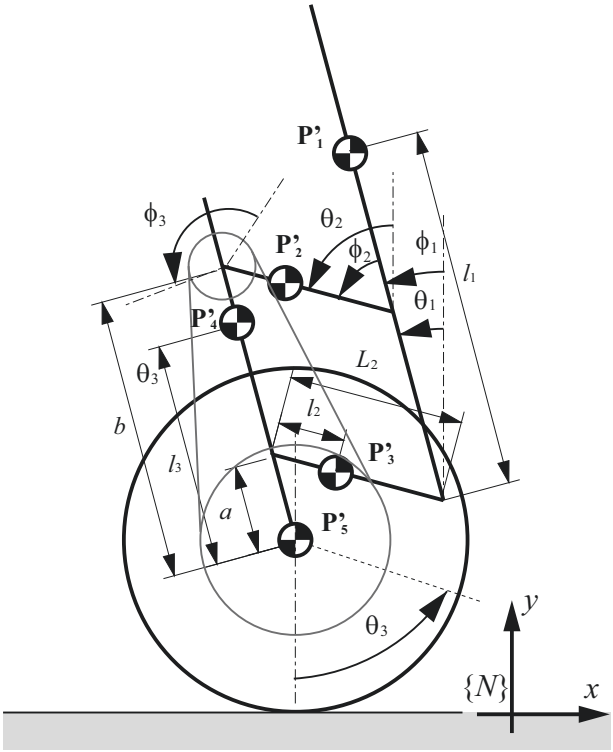


**Figure 3.14: Coordinate of the robot on longitudinal plane.**

is derived by using the generalized coordinates with respect to the global fixed frame that consist of the position coordinate and angle coordinate of each rigid body. The position and angle coordinate of each rigid body in the x and y axes are denoted by $\boldsymbol{P}_i = [P_{xi}\ P_{yi}]$, where index $i$, ($i = 1, 2, 3, 4, 5$), represents the index of body 2, arm 1, arm 2, body 1, and wheel, respectively. Furthermore, $\boldsymbol{\theta} = [\theta_1\ \theta_2\ \theta_3]^T$ consists of the body pitch $\theta_1$, arm angle $\theta_2$, and wheel angle $\theta_3$, represent the generalized coordinate of the robot.

The position coordinate of each rigid body is governed as follows:

$$\boldsymbol{P}_1 = \boldsymbol{P}_5 + b[-\sin\theta_1\ \cos\theta_1]^T + L_2[\sin\theta_2\ -\cos\theta_2]^T + l_1[-\sin\theta_1\ \cos\theta_1]^T, \quad (3.15)$$

$$\boldsymbol{P}_2 = \boldsymbol{P}_5 + b[-\sin\theta_1\ \cos\theta_1]^T + l_2[\sin\theta_2\ -\cos\theta_2]^T, \quad (3.16)$$

$$\boldsymbol{P}_3 = \boldsymbol{P}_5 + a[-\sin\theta_1\ \cos\theta_1]^T + l_2[\sin\theta_2\ -\cos\theta_2]^T, \quad (3.17)$$

$$\boldsymbol{P}_4 = \boldsymbol{P}_5 + l_3[-\sin\theta_1\ \cos\theta_1]^T, \quad (3.18)$$

$$\boldsymbol{P}_5 = L_4[-\theta_3\ 1]^T, \tag{3.19}$$

Let $T$, $U$, and $F$ denote the kinetic, potential, and damping energy of the three rigid bodies, respectively, and $\omega_i$ denotes the torque applied to each rigid body. The Lagrangian equation of motion is as follows:

$$\frac{d}{dt}\left(\frac{\partial T}{\partial \dot{\theta}_i}\right) - \frac{\partial T}{\partial \theta_i} + \frac{\partial F}{\partial \dot{\theta}_i} + \frac{\partial U}{\partial \theta_i} = \omega_i. \tag{3.20}$$

where $T$, $U$, and $F$ are as follows:

$$T = \frac{1}{2}\sum_{i=1}^{5}\left(m_i\left(\dot{P_{xi}}^2 + \dot{P_{zi}}^2\right) + I_i\dot{\theta_i}^2\right), \tag{3.21}$$

$$U = \sum_{i=1}^{5} m_i g p_{zi}, \tag{3.22}$$

$$F = \frac{1}{2}c_1\dot{\theta}_1^2 + \frac{1}{2}c_2\dot{\theta}_2^2 + \frac{1}{2}c_3\dot{\theta}_3^2. \tag{3.23}$$

where $m_i$ and $I_i$ denote the mass and inertia moment of the rigid bodies, respectively; $g$ denotes the gravity acceleration; and $c_1$, $c_2$ and $c_3$ denote the damping friction in each global coordinate.

By using the same method in chapter 2, the dynamic model of the robot is obtained via expanding Equation (3.20) using Equations (3.21)–(3.23) and Equations (3.15)–(3.19). The dynamic model of the robot is arranged as follows:

$$\boldsymbol{M}(\boldsymbol{\theta})\ddot{\boldsymbol{\theta}} + \boldsymbol{C}(\boldsymbol{\theta}, \dot{\boldsymbol{\theta}})\dot{\boldsymbol{\theta}} + \boldsymbol{D}\dot{\boldsymbol{\theta}} + \boldsymbol{G}(\boldsymbol{\theta}) = \boldsymbol{\tau}, \tag{3.24}$$

where $\boldsymbol{M}(\boldsymbol{\theta}) \in \boldsymbol{R}^{3\times3}$, $\boldsymbol{D} \in \boldsymbol{R}^{3\times3}$, and $\boldsymbol{C}(\boldsymbol{\theta}, \dot{\boldsymbol{\theta}}) \in \boldsymbol{R}^{3\times3}$ denote the symmetric inertia, viscosity, and coriolis matrices, respectively, and $\boldsymbol{G}(\boldsymbol{\theta}) \in \boldsymbol{R}^{3\times1}$ and $\boldsymbol{\tau} \in \boldsymbol{R}^{3\times1}$ denote the gravitational force, and torque vectors in generalized coordinates, respectively. The component of each

matrix is given as follows:

$$\boldsymbol{M}(\boldsymbol{\theta}) = \begin{bmatrix} M_{11} & M_{12} & M_{13} \\ M_{21} & M_{22} & M_{23} \\ M_{31} & M_{32} & M_{33} \end{bmatrix}, \tag{3.25}$$

$$\boldsymbol{D} = \begin{bmatrix} d_1 & 0 & 0 \\ 0 & d_2 & 0 \\ 0 & 0 & d_3 \end{bmatrix}, \tag{3.26}$$

$$\boldsymbol{C}(\boldsymbol{\theta}, \dot{\boldsymbol{\theta}}) = \begin{bmatrix} 0 & C_1\dot{\theta}_2 & 0 \\ C_2\dot{\theta}_1 & 0 & 0 \\ C_3\dot{\theta}_1 & C_4\dot{\theta}_2 & 0 \end{bmatrix}, \tag{3.27}$$

$$\boldsymbol{G}(\boldsymbol{\theta}) = \begin{bmatrix} (-m_2 b - m_1 b - m_2 a - m_3 l_3 - m_1 l_1) g s_1 \\ (2m_2 l_2 + m_1 L_2) g s_2 \\ 0 \end{bmatrix}, \tag{3.28}$$

$$\boldsymbol{\tau} = \begin{bmatrix} \tau_1 \\ \tau_2 \\ \tau_3 \end{bmatrix}. \tag{3.29}$$

The components of the matrix $\boldsymbol{M}$ are expressed as follows:

$$M_{11} = m_2b^2 + m_1b^2 + 2m_1l_1b + m_2a^2 + m_3l_3^2 + m_1l_1^2 + I_1 + I_2, \tag{3.30}$$

$$M_{22} = 2m_2l_2^2 + m_1L_2^2 + 2I_2 \tag{3.31}$$

$$M_{33} = m_4L_4^2 + m_3L_4^2 + 2m_2L_4^2 + m_1L_4^2 + I_4 \tag{3.32}$$

$$M_{12} = M_{21} = (-m_2l_2b - m_1L_2b - m_2l_2a - m_1l_1L_2)c_{2\bar{1}}, \tag{3.33}$$

$$M_{13} = M_{31} = (m_2L_4b + m_1L_4b + m_2L_4a + m_3l_3L_4m_1l_1L_4)c_1, \tag{3.34}$$

$$M_{23} = M_{32} = (-2m_2l_2L_4 - m_1L_2L_4)c_2, \tag{3.35}$$

The components of the matrix $\boldsymbol{C}$ are expressed as follows:

$$C_1 = (m_2l_2b + m_1L_2b + m_2l_2a + m_1l_1L_2)s_{2\bar{1}} \tag{3.36}$$

$$C_2 = (m_2l_2b - m_1L_2b - m_2l_2a - m_1l_1L_2)s_{2\bar{1}} \tag{3.37}$$

$$C_3 = (-m_2L_4b - m_1L_4b - m_2L_4a - m_3l_3L_4 - m_1l_1L_4)s_1 \tag{3.38}$$

$$C_4 = (2m_2l_2L_4 + m_1L_2L_4)s_2, \tag{3.39}$$

where, $s_i = \sin\theta_i$, $s_{i\bar{j}} = \sin(\theta_i - \theta_j)$, $c_i = \cos\theta_i$, and $c_{i\bar{j}} = \cos(\theta_i - \theta_j)$.

The generalized torque $\boldsymbol{\tau}$ expressed in Equation 3.29 represents the torque if I assume that each coordinates is driven by a motor. However, the robot only uses a single motor torque $\tau_m$. Therefore, I must obtain the relationship between a single motor torque $\tau_m$ and the generalized torque $\boldsymbol{\tau}$.

Let $\boldsymbol{\phi} = [\phi_1\ \phi_2\ \phi_3]^T$ denote the angle vector with respect to the body frame $\{B\}$, where $\phi_1$, $\phi_2$, and $\phi_3$ denote the angle of the body, angle of pulley 1 relative to the body, and angle of the arm relative to the body, respectively. As shown in Figure 3.14, I obtain the expression of body pitch angle $\theta_1$ and arm angle $\theta_2$ in local coordinate vectors as follows:

$$\theta_1 = \phi_1, \tag{3.40}$$

$$\theta_2 = \phi_1 + \phi_2. \tag{3.41}$$

The relationship between $\theta_1$, $\theta_2$, $\theta_3$, and $\phi_3$ by considering body 1 as a reference is as follows:

$$\frac{\phi_3 + R_h\theta_2}{R_h + 1} - \theta_1 = R_w(\theta_3 - \theta_1). \tag{3.42}$$

Additionally, $\theta_3$ is obtained by substituting Equation (3.41) into Equation (3.42) as follows:

$$\theta_3 = \frac{R_hR_w + R_w - 1}{(R_h + 1)R_w}\phi_1 + \frac{R_h}{(R_h + 1)R_w}\phi_2 + \frac{1}{(R_h + 1)R_w}\phi_3. \tag{3.43}$$

The relationship of $\boldsymbol{\theta}$ and $\boldsymbol{\phi}$ is arranged in a matrix $\boldsymbol{E} \in R^{3\times3}$ form as follows:

$$\boldsymbol{\theta} = \boldsymbol{E}\boldsymbol{\phi}, \tag{3.44}$$

where, the component of the matrix $\boldsymbol{E}$ is obtained by considering Equations (3.40)-(3.43) as follows:

$$\boldsymbol{E} = \begin{bmatrix} 1 & 0 & 0 \\ 1 & 1 & 0 \\ \frac{R_hR_w+R_w-1}{(R_h+1)R_w} & \frac{R_h}{(R_h+1)R_w} & \frac{1}{(R_h+1)R_w} \end{bmatrix}. \tag{3.45}$$

Let the actual applied torque that acted on the robot be $\boldsymbol{\gamma} = [\gamma_1\ \gamma_2\ \gamma_3]^T$. The relationship between $\boldsymbol{\tau}$ and $\boldsymbol{\gamma}$ is obtained through the principle of the virtual work as follows:

$$[\delta\theta_1\ \delta\theta_2\ \delta\theta_3]\boldsymbol{\tau} = [\delta\phi_1\ \delta\phi_2\ \delta\phi_3]\boldsymbol{\gamma}. \tag{3.46}$$

From Equation (3.45), the virtual differential displacements $\delta\theta_1$, $\delta\theta_2$, and $\delta\theta_3$ are ex-

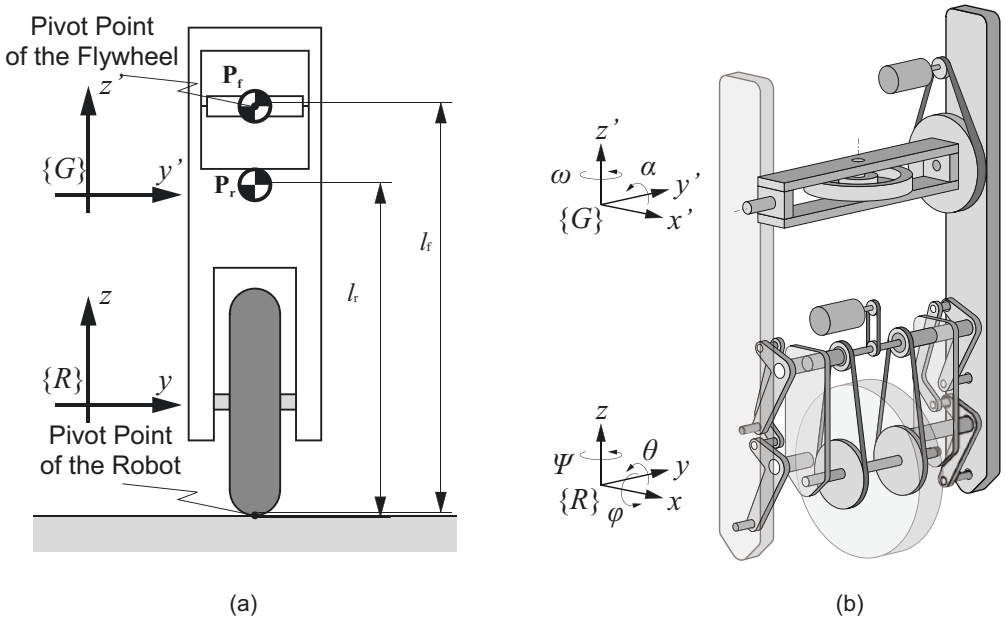


**Figure 3.15: Coordinate of the robot on lateral plane.**

pressed by $\delta\phi_1$, $\delta\phi_2$, and $\delta\phi_3$ as follows:

$$[\delta\theta_1\ \delta\theta_2\ \delta\theta_3]^T = \boldsymbol{E}[\delta\phi_1\ \delta\phi_2\ \delta\phi_3]^T. \tag{3.47}$$

Based on the configuration of the robot, the motor torque $\tau_m$ is applied on the $\phi_2$ coordinate. Additionally, no torque is applied on the $\phi_1$ and $\phi_2$ coordinates. Therefore $\boldsymbol{\gamma} = [0\,0\,1]^T\tau_m$. Subsequently, the relationship between $\boldsymbol{\omega}$ and motor torque $\tau_m$ is obtained from Equations (3.46) and (3.47) as follows:

$$\boldsymbol{\gamma} = (\boldsymbol{E}^T)^{-1}[0\ 0\ 1]^T\tau_m. \tag{3.48}$$

### 3.5.2 Lateral dynamics

The coordinate of the robot to derive the lateral dynamics is shown in Figure 3.15. In this model, the robot consist of two rigid body, namely the robot and the flywheel. To derive the lateral dynamics, first, I consider the rotational behavior of robot and flywheel with respect of global frame $O - xyz$. Let $R_p$ and $R_g$ denote the rotation matrix of robot in reference frame $R - x'y'z'$ and $G - x"y"z"$, respectively. The rotational speed of the robot

under reference frame $R - x'y'z'$ and $G - x"y"z"$ is governed as follows:

$$\Omega_r = R_r^T \omega_r \tag{3.49}$$

where,

$$\boldsymbol{R}_r = \begin{bmatrix} 1 & 0 & 0 \\ 0 & \cos\phi & \sin\phi \\ 0 & -\sin\phi & \cos\phi \end{bmatrix}, \tag{3.50}$$

$$\omega_r = [\dot{\phi}\ 0\ 0]^T. \tag{3.51}$$

where, $\omega_r$ denotes the rotational speed of the robot in reference frame $O - xyz$. The rotational speed of the flywheel under reference frame $G - x"y"z"$ is governed as follows:

$$\Omega_g = R_f^T \omega_r + \omega_g \tag{3.52}$$

where,

$$\boldsymbol{\Omega}_g = \begin{bmatrix} \cos\alpha & 0 & \sin\alpha \\ -\sin\alpha\sin\phi & \cos\phi & \cos\alpha\sin\phi \\ -\sin\alpha\cos\phi & -\sin\phi & \cos\alpha\cos\phi \end{bmatrix}, \tag{3.53}$$

$$\omega_g = [0\ \dot{\alpha}\ \omega]^T, \tag{3.54}$$

where, $\omega_g$ denotes the rotational speed of the flywheel in reference frame $O - xyz$.

The position coordinate of the robot and the flywheel are governed as follows:

$$\boldsymbol{P}_r = [0\ l_r\sin\phi\ l_r\cos\phi]^T, \tag{3.55}$$

$$\boldsymbol{P}_f = [0\ l_f\sin\phi\ l_f\cos\phi]^T, \tag{3.56}$$

where, $\boldsymbol{P}_r$ and $\boldsymbol{P}_g$ denote the coordinate vector of the COG of the robot and the flywheel

with respect of global frame.

Let $T$, $U$, $F$, $\tau_p$ and $\tau_r$ denote the the kinetic, potential, damping energy, the torque applied on the flywheel on axis-$y$" and the robot on axis-$y'$, respectively. $T$, $U$, and $F$ are as follows:

$$T = \frac{1}{2}\Omega_r^T J_r \Omega_r + \frac{1}{2}\Omega_f^T J_f \Omega_f + \frac{1}{2} m_r \dot{\boldsymbol{P}}_r^T \dot{\boldsymbol{P}}_r + \frac{1}{2} m_g \dot{\boldsymbol{P}}_f^T \dot{\boldsymbol{P}}_f, \tag{3.57}$$

$$U = m_r g l_r \cos\phi + m_g g l_f \cos\phi, \tag{3.58}$$

$$F = \frac{1}{2} d_1 \dot{\theta}_1^2 + \frac{1}{2} d_2 \dot{\theta}_2^2. \tag{3.59}$$

where $m_r$, $m_g$ denote the mass of the robot and the flywheel, respectively; $J_r$ and $J_g$ denote the inertia moment of the robot and the flywheel, respectively; $g$ denotes the gravity acceleration; and $d_1$ and $d_2$ denote the damping friction in coordinate $\phi$ and $\alpha$, respectively. The inertia moment of the robot and the flywheel is given as follows:

$$\boldsymbol{J}_r = \begin{bmatrix} J_r x & 0 & 0 \\ 0 & 0 & 0 \\ 0 & 0 & 0 \end{bmatrix}, \tag{3.60}$$

$$\boldsymbol{J}_g = \begin{bmatrix} J_g x & 0 & 0 \\ 0 & J_g y & 0 \\ 0 & 0 & J_g z \end{bmatrix}, \tag{3.61}$$

By using Lagrange equation, the lateral dynamics of the robot is expressed as follows:

$$\begin{aligned}(m_p h_p^2 + m_g h_g^2 + J_g z \sin^2\alpha + J_g x \cos^2\alpha + J_r x)\ddot{\alpha} + 2(J_g z - J_g x \dot{\alpha}\dot{\phi} \sin\alpha \cos\alpha \\ + c_1 \dot{\phi} + J_g z \cos\alpha \dot{\alpha} - (m_g h_g + m_r h_r) \sin\phi = \tau_r,\end{aligned} \tag{3.62}$$

$$J_g x\ddot{\alpha} - J_g z\omega \cos\alpha\dot{\phi} + (J_g x - J_g z)\sin\alpha\cos\alpha\dot{\phi}^2 + c_2\dot{\alpha} = \tau_p \tag{3.63}$$

## 3.6 Control method

The lateral and longitudinal motion of the robot is controlled by using two separate control methods. The lateral control method is employed to control the moment gyroscope for achieving lateral stability. The longitudinal control method is employed to control the proposed differential driving mechanism, described in section 3.3, for achieving longitudinal stability and realizing climbing motion.

**Lateral control method :** The objectives of the lateral control method are to control the roll balance of the robot and to maintain the precession angle so as not to reach the singularity configuration. To achieve these objectives, the conventional method is used: controlling the high-speed spinning flywheel precession angle and its rate using proportional-derivative (PD) control [41, 42, 43]. The feedback inputs for controlling the lateral attitude of the robot are the roll angle of the robot with its rate ($\phi$ and $\dot{\phi}$) and the gyro precession angle with its rate ($\alpha$ and $\dot{\alpha}$). The control law for computing the gimbal motor current, $i_g$, is given as follows:

$$i_g = \frac{f_1\alpha + f_2\dot{\alpha} + f_3\phi + f_4\dot{\phi}}{\cos\alpha} + K_{fg}\mathrm{sgn}(\dot{\alpha}), \tag{3.64}$$

where $f_1, f_2, f_3, f_4$ denote the gain for controlling the lateral attitude of the robot. Specifically, $K_{fg}$ denotes the gain for compensating the static friction on the gimbal motor and belt-pulley system.

**Longitudinal control method :** The objectives of the lateral control method are to control the pitch balance of the robot and to achieve step-climbing motion. To achieve these objectives the same control method is used as in the previous study [53]. The feedback inputs for controlling the longitudinal attitude of the robot are the pitch angle and its rate ($\theta$ and $\dot{\theta}$), arm angle and its rate ($\theta_a$ and $\dot{\theta_a}$), and wheel angle and its rate ($\theta_w$ and $\dot{\theta_w}$).

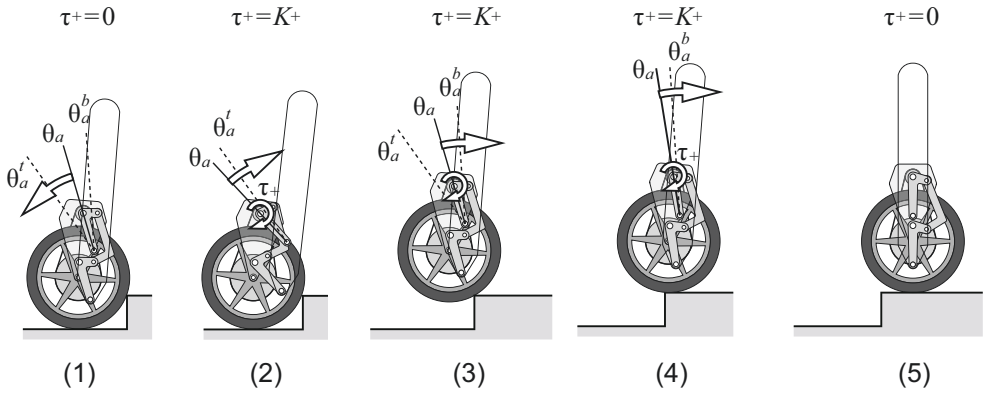


**Figure 3.16: The algorithm of supplemental torque $\tau_+$.**

The control law for computing the current of the driving motor, $i_d$, is given as follows:

$$\begin{aligned} i_d = {} & f_4\theta + f_5\dot{\theta} + f_6\dot{\theta_{in}} + f_7\theta_a + f_8\dot{\theta_a} \\ & + f_9 + K_{fd}\mathrm{sgn}(\dot{\theta_{in}}) + \tau_+ + \tau_-, \end{aligned} \tag{3.65}$$

where $f_4, f_5, f_6, f_7, f_8$, and $f_9$ denote the feedback gains for controlling the longitudinal attitude of the robot and feed-forward gains for controlling the speed of the robot. Additionally, $K_{fd}$ denotes the gain for compensating the total static friction included in driving the motor. The function of sgn($x$) is defined as follows:

$$\mathrm{sgn}(x) = \begin{cases} -1, & x < 0 \\ 1, & x \geq 0 \end{cases} \tag{3.66}$$

$\tau_+$ and $+\tau_-$ denote the supplemental torque for ascending and descending a step, respectively. The algorithm of supplemental torque for ascending a step, $\tau_+$, is described as follows: The robot rotates the parallel arm when encountering the step, as shown in Figure 3.16(1). When $\theta_a$ exceeds the top threshold $\theta_a^t$, $\tau_+$ is set to the magnitude of the supplemental torque $K_+$, as shown in Figure 3.16(2). After the robot climbs a step, $\theta_a$ is expected to decrease, as shown in Figures 3.16(3) and (4). Subsequently, until the arm angle reaches the bottom threshold $\theta_a^b$, the supplemental torque, $\tau_+$, is set to 0, as shown

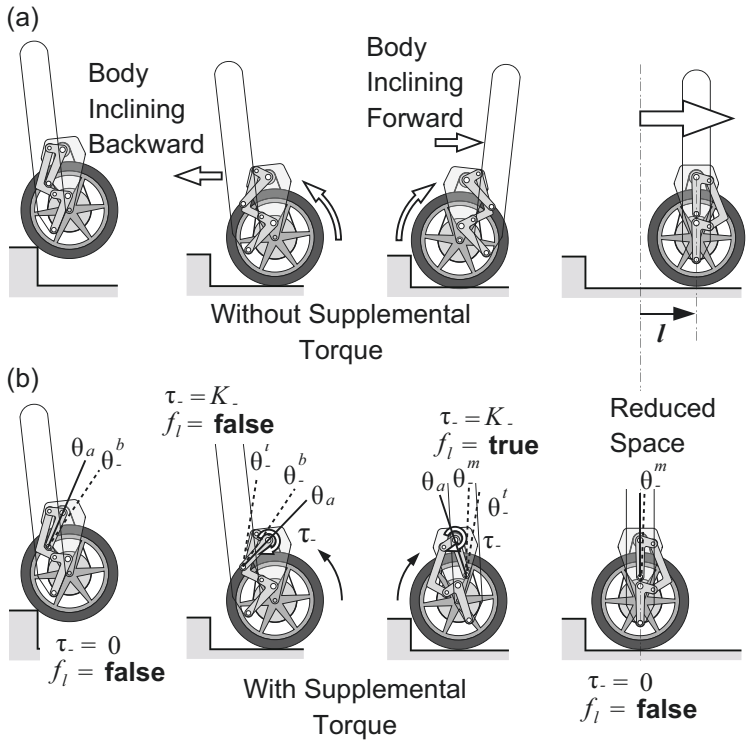


**Figure 3.17: Motion of the robot descending a step.**

in Figure 3.16(5). The update rule of supplemental torque is as follows:

$$\begin{aligned} &\text{if} && (\tau_+ = 0) \wedge (|\theta_a| \geq |\theta_a^t|) \quad \text{then} \quad \text{update} \ \tau_+ \ \text{to} \ K_+. \\ &\text{if} && (\tau_+ = K_+) \wedge (|\theta_a| \leq |\theta_a^b|) \quad \text{then} \quad \text{update} \ \tau_+ \ \text{to} \ 0. \\ &\text{else} && \text{do not update } \tau_+. \end{aligned} \tag{3.67}$$

The details of the supplemental torque for ascending a step is explained in [53]. The application of the supplemental torque is important for the robot to climb a stair. This is because it can reduce the distance of the robot to recover its stability after climbing the step [60]. Thus, the robot will not lose the stability if the next step exists immediately after the robot climbing the step.

The algorithm of supplemental torque for descending a step, $\tau_-$ is described as follows. When descending a step, the robot is expected to incline backwards, and its arms is also expected to swing backward at a high rate. In this case, the regulatory control of the robot will produce a high motor torque for the wheel to rotate backward, as shown

in Figure 3.17(a), and therefore, the backward inclination will be reduced. However, if the inclination angle and the arm angle are high, the control method will compute an extremely high motor torque. Consequently, the wheel will rotate backward very quickly; hence, the robot will incline forwards. This condition increases the distances required for the robot to regain its stability. However, steps in the flight of a staircase typically have narrow treads. If the robot cannot regain its stability before descending the next step, it will fall down.

To address this problem, I considered applying a supplemental torque, $\tau_{-}$, for reducing the acceleration when the robot attempts to regain its stability. The timing of the application of $\tau_{-}$ when the robot descends a stair is shown in Figure 3.17(b).

The update rule of the supplemental torque is as follows:

$$
\begin{aligned}
&\text{if } (\tau_{-} = 0) \wedge (f_l = \textbf{false}) \wedge (\theta_a \geq \theta_{-}^{b}) \\
&\text{then update } \tau_{-} \text{ to } K_{-}. \\
&\text{if } (\tau_{-} = K_{-}) \wedge (f_l = \textbf{false}) \wedge (\theta_a \leq \theta_{-}^{t}) \\
&\text{then update } f_l \text{ to } \textbf{true}. \\
&\text{if } (\tau_{-} = K_{-}) \wedge (f_l = \textbf{true}) \wedge (\theta_a \geq \theta_{-}^{m}) \\
&\text{then update } \tau_{-} \text{ to } 0 \text{ and update } f_l \text{ to } \textbf{false}. \\
&\text{else do not update } \tau_{-} \text{and } f_l,
\end{aligned}
\tag{3.68}
$$

where, $\theta_{-}^{b}, \theta_{-}^{m}$, and $\theta_{-}^{t}$ denote the bottom, middle, and top thresholds of the arm angle, respectively, which denote the timing flag for updating $\tau_{-}$. The relationship between the three thresholds is $\theta_{-}^{b} > \theta_{-}^{m} > \theta_{-}^{m}$. In addition, $\theta_a$, $K_{-}$, and $f_l$ denote the arm angle, the magnitude of the supplemental torque, and the flag signal to indicate that the supplemental torque is still necessary to be applied when $\theta_a$ reaches $\theta_t$. The detail of the update rule described in Equation 3.68 is explained below. When the robot descends, the arms are expected to swing backward, and therefore, when $\theta_a$ reaches $\theta_{-}^{b}$, $\tau_{-}$ is set as $K_{-}$. Under this condition, the $\tau_{in}$ required to rotate the wheel backward is reduced, and thus, the robot will gradually move backward. Subsequent to $\theta_a$ reaching $\theta_{-}^{b}$, the arms are expected to

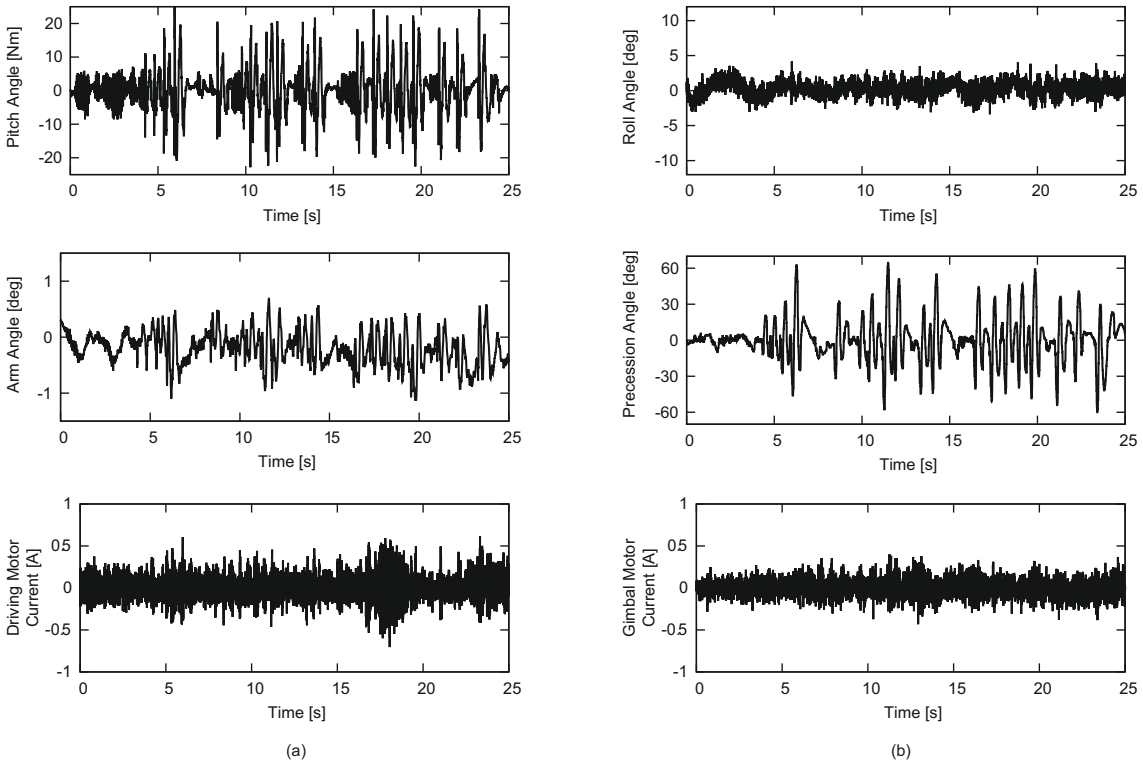


**Figure 3.18: Experimental results of robot stability under longitudinal disturbance. (a) longitudinal motion and (b) lateral motion.**

swing forward. When the robot reaches $\theta^t_-$, $f_l$ is set as **true**, and $\tau_-$ is not updated. Under this condition, $\tau_{in}$ is increased, and therefore, the robot will rapidly move forward to reduce the inclination angle. After $\theta_a$ reaches $\theta^t_-$, the arms are expected to swing backward again. When the robot reaches $\theta^m_-$, $f_l$ is set as **false** and $\tau_-$ is set as zero.

# 3.7 Experiment

## 3.7.1 Stability of the robot under the longitudinal disturbance

In this subsection, the experiment to evaluate the stability of the robot under the longitudinal disturbance is presented. The stability was evaluated by adding impulse force on the wheel. Figures 3.18(a1), (a2), and (a3) show the pitch angle $\theta$, arm angle $\theta_a$, and driving motor current $i_d$, respectively, of the robot during experiment. As shown in Figures 3.18(a1) and (a2), the robot could maintain the pitch angle between $-20^\circ$ to $20^\circ$ and the arm angle between $-1^\circ$ to $1^\circ$. Figures 3.18(b1), (b2), and (b3) show the

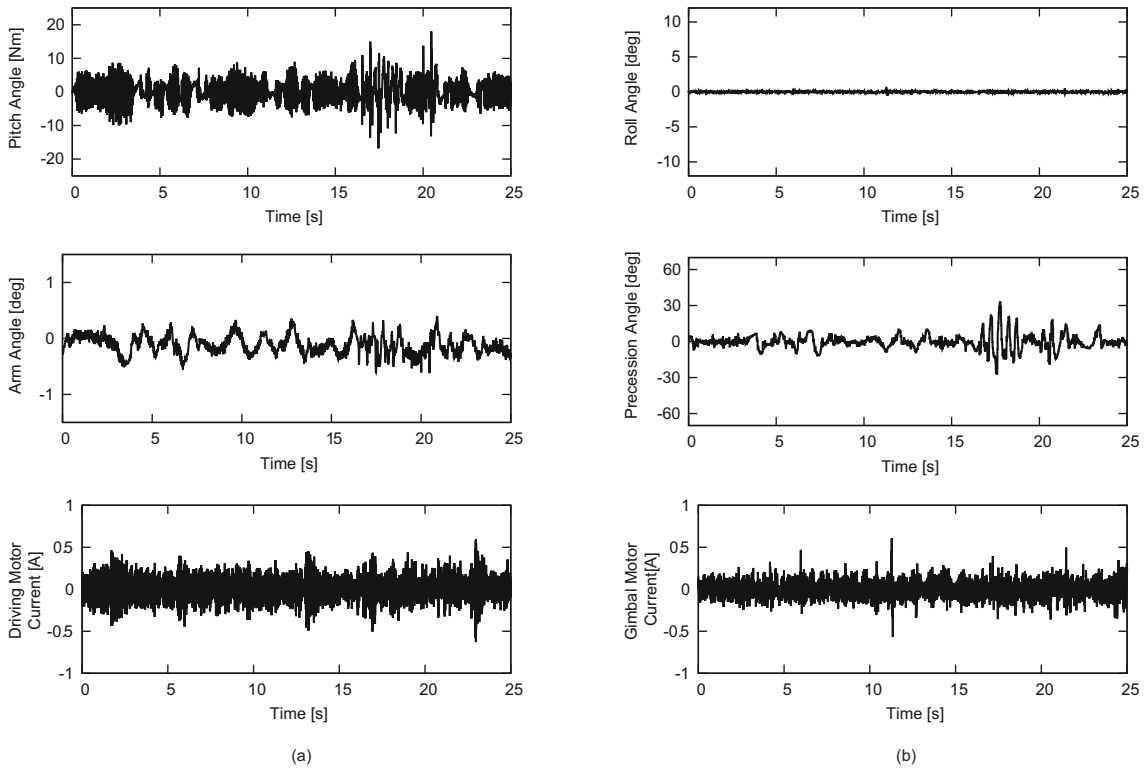


**Figure 3.19: Experimental results of robot stability under lateral disturbance (a) longitudinal motion and (b) lateral motion.**

roll angle $\theta$, precession angle $\theta_a$, and gimbal motor current $i_d$, respectively, of the robot during experiment. As shown in Figures 3.18(b1) and (b2), the robot could maintain the roll angle between $-5^\circ$ to $5^\circ$ and the precession angle between $-60^\circ$ to $60^\circ$. Although the precession angle was abruptly changed to $\pm 60^o$ when the disturbance was given to the robot, the precession angle was maintained at less than $\pm 90^\circ$. Thus the CMG was still able to provide the torque in the lateral direction to stabilize the robot on the lateral direction which is shown by the stability of the roll angle in Figure 3.18(b1). This implies that the robot could maintain the pitch stability even though the robot was given the disturbance on the wheel.

### 3.7.2 Stability of the robot under the lateral disturbance

In this subsection, the experiment to evaluate the stability of the robot under the lateral disturbance is presented. The stability was evaluated by adding impulse force on

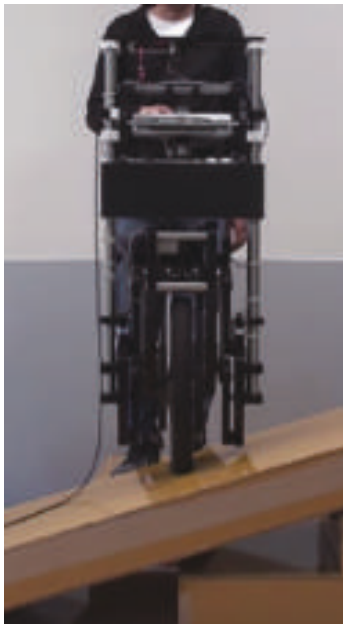

**Figure 3.20: Snapshot of the robot stabilizing on a lateral slope with an angle of** $16^\circ$**.**

side of the body. Figures 3.18(a1), (a2), and (a3) show the pitch angle $\theta$, arm angle $\theta_a$, and driving motor current $i_d$, respectively, of the robot during experiment. As shown in Figures 3.18(a1) and (a2), the robot could maintain the pitch angle between $-20^\circ$ to $20^\circ$ and the arm angle between $-1^\circ$ to $1^\circ$. Figures 3.18(b1), (b2), and (b3) show the roll angle $\theta$, precession angle $\theta_a$, and gimbal motor current $i_d$, respectively, of the robot during experiment. As shown in Figures 3.18(b1) and (b2), the robot could maintain the roll angle between $-2^\circ$ to $2^\circ$ and the precession angle between $-30^\circ$ to $30^\circ$. Although the precession angle was abruptly changed to $\pm 60^\circ$ when the disturbance was given to the robot, the precession angle was maintained at less than $\pm 90^\circ$. Thus the CMG was still able to provide the torque in the lateral direction to stabilize the robot on the lateral direction which is shown by the stability of the roll angle in Figure 3.18(b1). This implies that the robot could maintain the pitch stability even though the robot was given the disturbance on the lateral direction.

### 3.7.3 Stability of the robot on a lateral slope

In this subsection, the experiment of the robot stabilizing on a lateral slope with an angle of $16^\circ$ is presented. Figure 3.20 shows the snapshot of the robot stabilizing on a

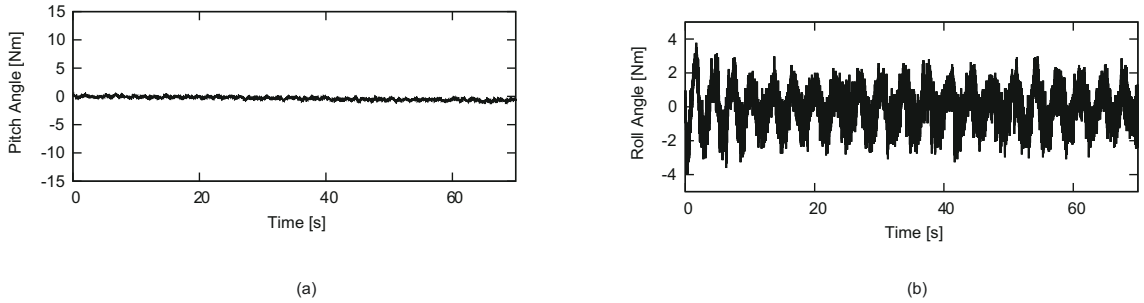


**Figure 3.21: Experimental results of the robot stabilizing on a lateral slope with an angle of** 16° **(a) pitch angle and (b) roll angle.**

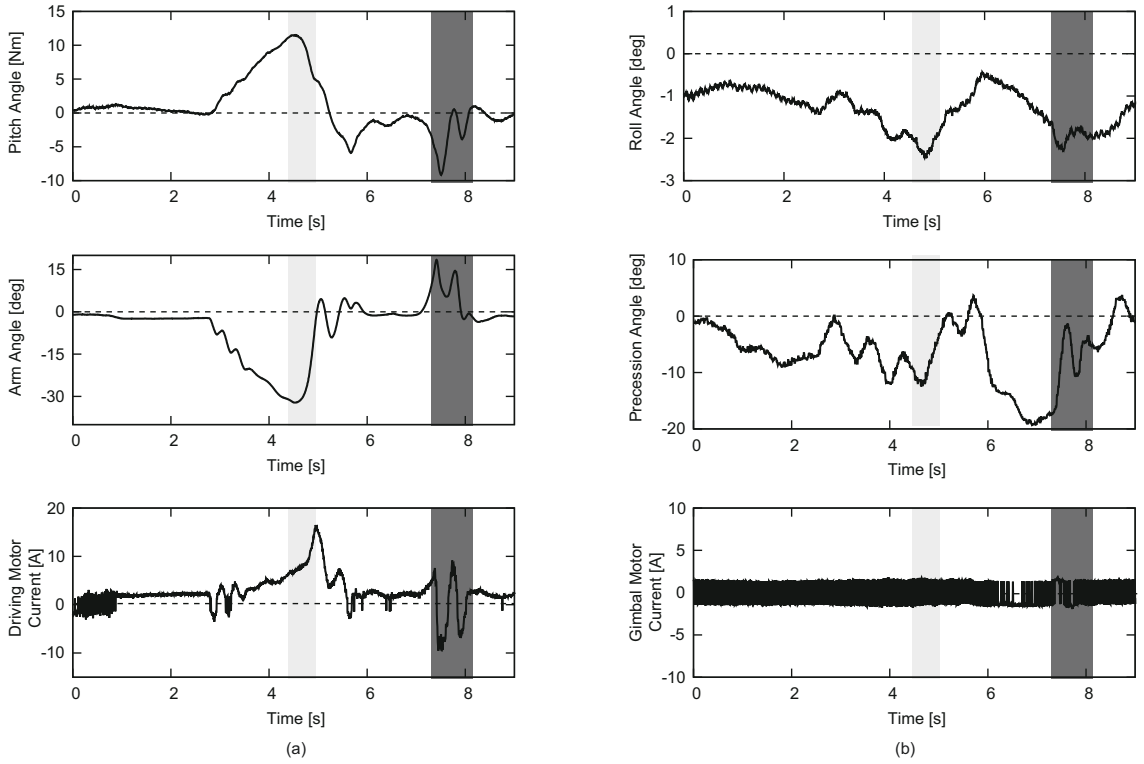


**Figure 3.22: Experimental results of the robot ascending and descending a 6-cm high step.**

lateral slope. Figures 3.21(a) and (b) show the pitch and roll angles of the robot stabilizing on a lateral slope, respectively. From Figures 3.20(a) and (b), the robot could maintain its pitch and roll angles between ±5°. Thus, it can be concluded that the robot can maintain its balance while operating on a lateral slope.

### 3.7.4 Ascending and descending 6 cm step

In this subsection, the experiment of the robot climbing a 6 cm step is presented. Figures 3.22(a1), (a2), and (a3) show the pitch angle $\theta$, arm angle $\theta_a$, and driving motor current $i_d$, respectively, of the robot while climbing the step. The light gray highlights in Figure 3.25 show the condition of the robot when attempting to climb a step. As shown in Figure 3.22(a2) the arm lifts body #2 to shift the COG as indicated by the increment of arm angle $\theta_a$. The maximum arm angle $\theta_a$ required for climbing the step is approximately $-30^\circ$. As shown in Figure 3.22(a1), although the pitch angle of the robot $\theta$ was inclined approximately to $12^\circ$ when climbing each step, the pitch angle returned to a stable attitude after the robot climbed the step. This implies that the stability of the robot is guaranteed, although the robot was inclining when climbing the stairs. As shown in Figure 3.22(a3) the driving motor torque increased and thus provided the torque for the arm to lift the main body. From Figures. 3.22(a2) and (a3), the driving current changes drastically when the arm angle $\theta_a$ reaches the threshold values $\theta_a^t$ and $\theta_a^b$. The maximum current of the driving motor torque for the step is approximately 18 A.

Figures 3.22(b1), (b2), and (b3) show the spinning flywheel precession angle $\alpha$, roll angle of the robot $\phi$, and gimbal motor current $i_g$, respectively. Figure 3.22(b1) shows that the precession angle $\alpha$ varied between $-20^\circ$ to $5^\circ$. The precession angle $\alpha$ abruptly changed from when the robot was attempting to climb a step and after successfully climbing the step, as shown in gray highlights in Figure 3.25(b1). Although the precession angle varied during the experiment, the precession angle was maintained at less than $\pm 90^\circ$. Thus the CMG was still able to provide the torque in the lateral direction because it did not reach a singularity configuration. The roll angle of the robot is shown in Figure 3.22(b2). As shown in Figure 3.22(b2) the roll angle $\phi$ varied between $-3^\circ$ to $-0.7^\circ$. This implies that the lateral balance is guaranteed even though perturbation from the climbing motion was involved. Although the roll angle has a slight offset, the robot could maintain lateral stability by using the control moment gyroscope. The gimbal motor current $i_g$ to control the lateral balance of the robot varied between -2 to 2 A, as shown in Figure 3.22(b3).

The dark gray highlights in Figures. 3.22(a1), (a2), and (a3) display the pitch an-

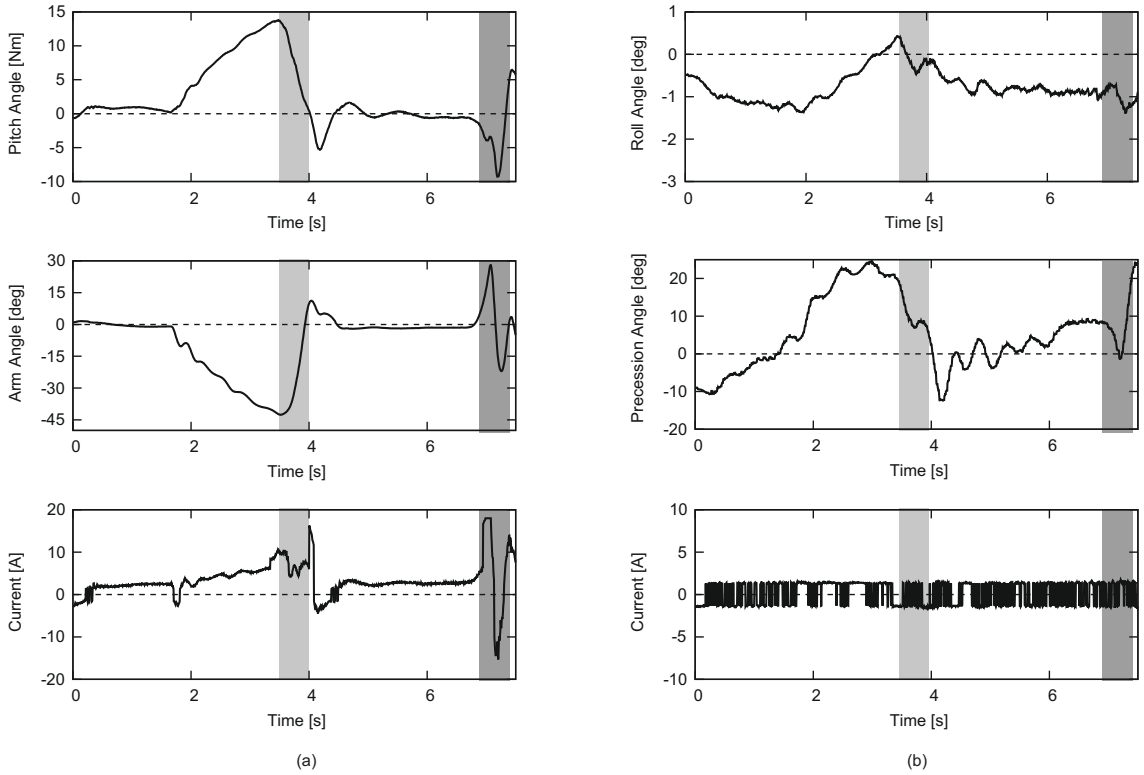


**Figure 3.23: Experimental results of the robot ascending and descending a 12-cm high step.**

gle, $\theta$, arm angle, $\theta_a$, and driving motor current, $i_d$, respectively, while descending the stairs. After the robot descends the stairs, it inclines backward to approximately $-10°$, and the arm angle swings backward to approximately 15°, as shown in Figs. 3.22(a) and (b), respectively. Because the robot inclines backward, the driving motor current changes drastically from approximately 10 A to approximately $-10$ A to compensate for the inclination of the robot, as shown in 3.22(c). The change in the driving motor current is reduced because the supplemental torque is active, and therefore, the acceleration of the robot for moving backward is reduced.

### 3.7.5 Ascending and descending 12 cm step

In this subsection, the experiment of the robot climbing a 12 cm step is presented. Figures 3.23(a1), (a2), and (a3) show the pitch angle $\theta$, arm angle $\theta_a$, and driving motor current $i_d$, respectively, of the robot while climbing the step. The light gray highlights in

Figure 3.23 show the condition of the robot when attempting to climb a step. As shown in Figure 3.23(a2) the arm lifts body #2 to shift the COG as indicated by the increment of arm angle $\theta_a$. The maximum arm angle $\theta_a$ required for climbing the step is approximately $-45°$. As shown in Figure 3.23(a1), although the pitch angle of the robot $\theta$ was inclined approximately to 15° when climbing each step, the pitch angle returned to a stable attitude after the robot climbed the step. This implies that the stability of the robot is guaranteed, although the robot was inclining when climbing the stairs. As shown in Figure 3.23(a3) the driving motor torque increased and thus provided the torque for the arm to lift the main body. From Figures. 3.23(a2) and (a3), the driving current changes drastically when the arm angle $\theta_a$ reaches the threshold values $\theta_a^t$ and $\theta_a^b$. The maximum current of the driving motor torque for the step is approximately 18 A.

Figures 3.23(b1), (b2), and (b3) show the spinning flywheel precession angle $\alpha$, roll angle of the robot $\phi$, and gimbal motor current $i_g$, respectively. Figure 3.23(b1) shows that the precession angle $\alpha$ varied between $-10°$ to 25°. The precession angle $\alpha$ abruptly changed from when the robot was attempting to climb a step and after successfully climbing the step, as shown in gray highlights in Figure 3.23(b1). Although the precession angle varied during the experiment, the precession angle was maintained at less than ±90°. Thus the CMG was still able to provide the torque in the lateral direction because it did not reach a singularity configuration. The roll angle of the robot is shown in Figure 3.23(b2). As shown in Figure 3.23(b2) the roll angle $\phi$ varied between $-1°$ to 0.4°. This implies that the lateral balance is guaranteed even though perturbation from the climbing motion was involved. Although the roll angle has a slight offset, the robot could maintain lateral stability by using the control moment gyroscope. The gimbal motor current $i_g$ to control the lateral balance of the robot varied between -2 to 2 A, as shown in Figure 3.23(b3).

The dark gray highlights in Figures. 3.23(a1), (a2), and (a3) display the pitch angle, $\theta$, arm angle, $\theta_a$, and driving motor current, $i_d$, respectively, while descending the stairs. After the robot descends the stairs, it inclines backward to approximately $-10°$, and the arm angle swings backward to approximately 30°, as shown in Figs. 3.23(a) and (b), respectively. Because the robot inclines backward, the driving motor current changes drastically from approximately 18 A to approximately $-18$ A to compensate for the in-

**Figure 3.24: Snapshots of a single-wheeled robot ascending stairs.**

clination of the robot, as shown in 3.23(c). The change in the driving motor current is reduced because the supplemental torque is active, and therefore, the acceleration of the robot for moving backward is reduced.

### 3.7.6 Ascending and descending 12 cm stairs

Here, the experimental result of the robot climbing stairs is presented. The experiment evaluates the performance of the proposed robot while climbing a staircase with four steps. The tread depth and riser height of each step are 39 cm and 12–13 cm, respectively. In the experiment, the rotational speed of the flywheel is set at a constant rate of 7000 rpm. All controller gains used in the experiment were determined by trial and error. Figure 3.24 shows snapshots of the robot climbing the stairs.

Figures 3.25(a1), (a2), and (a3) show the pitch angle $\theta$, arm angle $\theta_a$, and driving motor current $i_d$, respectively, of the robot while climbing stairs. The gray highlights in Figure 3.25 show the condition of the robot when attempting to climb a step. As shown in Figure 3.25(a2) the arm lifts body #2 to shift the COG as indicated by the increment of arm angle $\theta_a$. The maximum arm angle $\theta_a$ required for climbing each step is approximately 46°. As shown in Figure 3.25(a1), although the pitch angle of the robot $\theta$ was inclined approximately to 12° when climbing each step, the pitch angle returned to a stable attitude after the robot climbed the step. This implies that the stability of the robot is guaranteed, although the robot was inclining when climbing the stairs. As shown in Figure 3.25(a3)

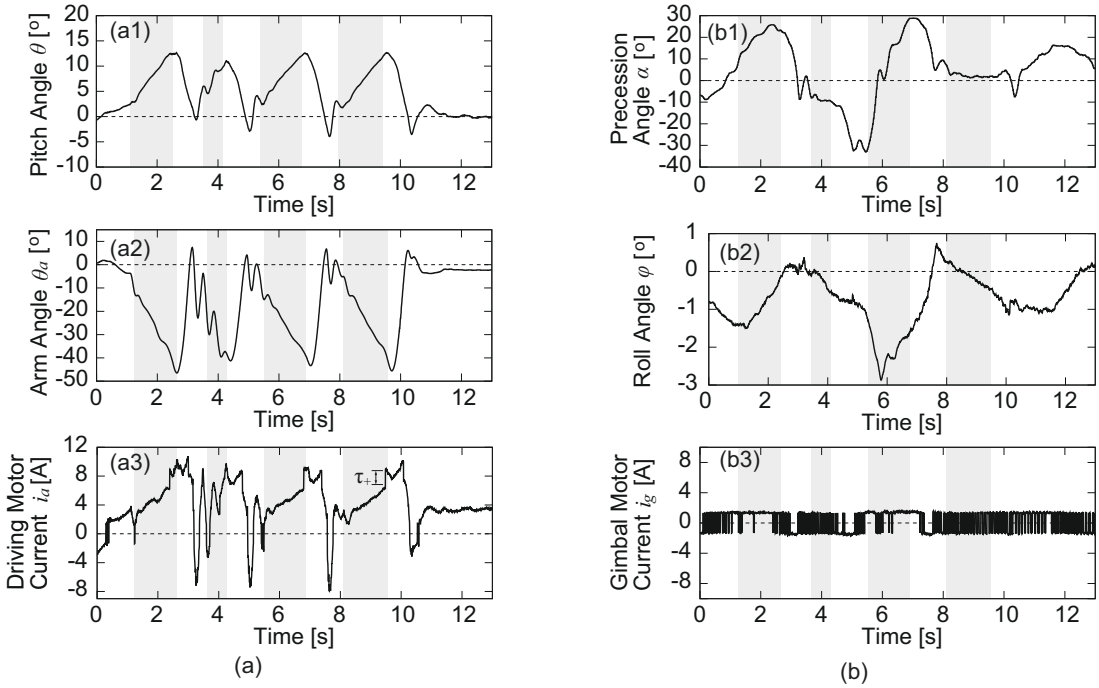


**Figure 3.25: Experimental results of the robot ascending stairs.**

the driving motor torque increased and thus provided the torque for the arm to lift the main body. The parameters of supplemental torque used in this experiment were $\theta_a^t = -37°$, $\theta_a^b = -10°$, and $K_+ = 27$ mNm. From Figures. 3.25(a2) and (a3), the driving current changes drastically when the arm angle $\theta_a$ reaches the threshold values $\theta_a^t$ and $\theta_a^b$. The maximum current of the driving motor torque for climbing each step is approximately 11 A.

Figures 3.25(b1), (b2), and (b3) show the spinning flywheel precession angle $\alpha$, roll angle of the robot $\phi$, and gimbal motor current $i_g$, respectively. Figure 3.25(b1) shows that the precession angle $\alpha$ varied between $-33°$ to $29°$. The precession angle $\alpha$ abruptly changed from when the robot was attempting to climb a step and after successfully climbing the step, as shown in gray highlights in Figure 3.25(b1). Although the precession angle varied during the experiment, the precession angle was maintained at less than $\pm 90°$. Thus the CMG was still able to provide the torque in the lateral direction because it did not reach a singularity configuration. The roll angle of the robot is shown in Figure 3.25(b2). As shown in Figure 3.25(b2) the roll angle $\phi$ varied between $-3°$ to $0.7°$. The roll angle

**Figure 3.26: Snapshots of a single-wheeled robot descending stairs.**

of the robot drastically changed when the robot climbed the second step, yet the control method was still able to gradually reduce the roll angle into a stable state. This implies that the lateral balance is guaranteed even though perturbation from the climbing motion was involved. Although the roll angle has a slight offset, the robot could maintain lateral stability by using the control moment gyroscope. The gimbal motor current $i_g$ to control the lateral balance of the robot varied between $-2$ to 2 A, as shown in Figure 3.25(b3).

In the experiment, the robot successfully climbed four steps without losing its balance, both in the pitch and roll directions. The climbing rate of each step was approximately 2 to 3 s. For the reference, the reader is invited to view the video recording of this experiment. I also performed an experiment with the robot descending the stairs, which can also be viewed in the video recording. When the robot descended the stair, the robot used the same control method that was described in section 3.6. However, the supplemental torque was applied every time the robot descended a single step to reduce the inclination of the robot. By using this method, the robot can complete descending four steps without losing its stability.

To evaluate the effectiveness of the method, I performed an experiment in which the robot descended a staircase consisting of four steps. The tread depth and the riser height of each step were 39 cm and 12–13 cm, respectively. Figure 3.26 shows the snapshots of

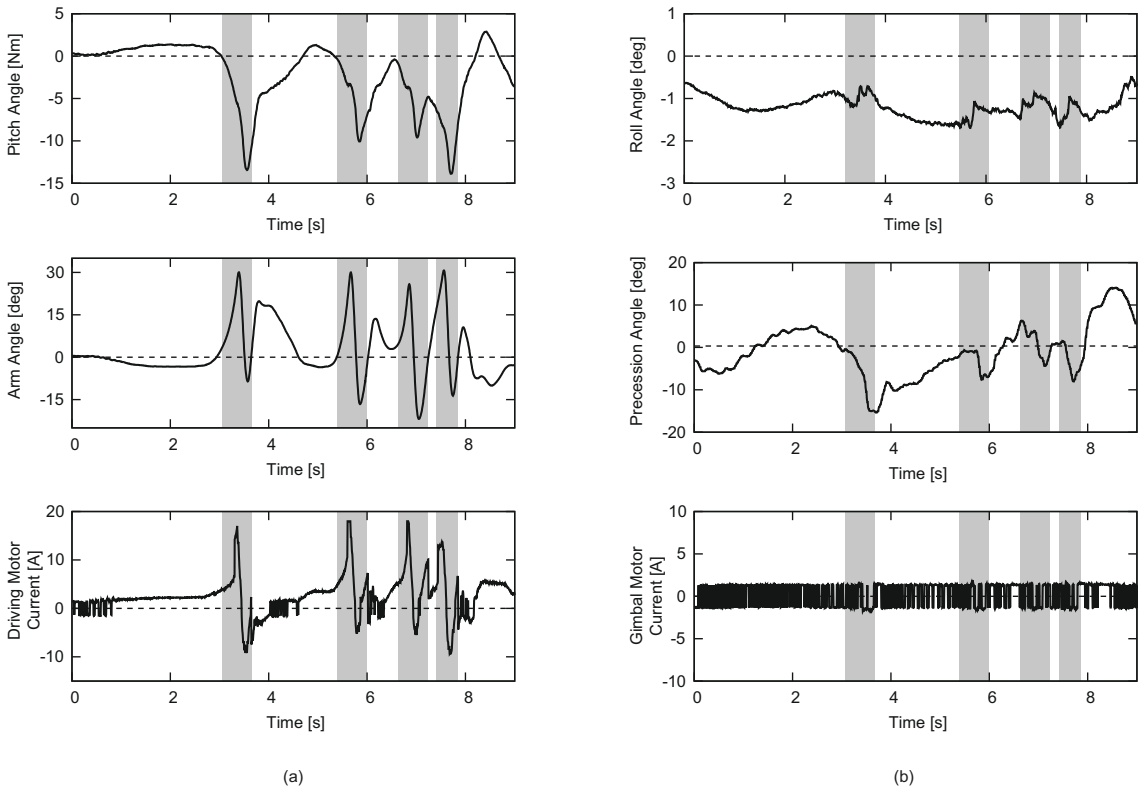


**Figure 3.27: Experimental results of the robot descending stairs.**

the robot descending the stairs.

Figs. 3.27(a), (b), and (c) display the pitch angle, $\theta$, arm angle, $\theta_a$, and driving motor current, $i_d$, respectively, while descending the stairs. The gray highlights in Figs. 3.27(a), (b), and (c) indicate the timing when the supplemental torque is active while descending the stairs. After the robot descends the stairs, it inclines backward to approximately $-10°$–$-14°$, and the arm angle swings backward to approximately $30°$, as shown in Figs. 3.27(a) and (b), respectively. Because the robot inclines backward, the driving motor current changes drastically from approximately 15 A to approximately $-8$ A to compensate for the inclination of the robot, as shown in 3.27(c). The change in the driving motor current is reduced because the supplemental torque is active, and therefore, the acceleration of the robot for moving backward is reduced. Using this method, the robot could descend four steps consecutively without losing stability, because the pitch angle could be returned to a stable attitude before descending the next step. For the reference, the reader is recommended to view the video recording of this experiment.

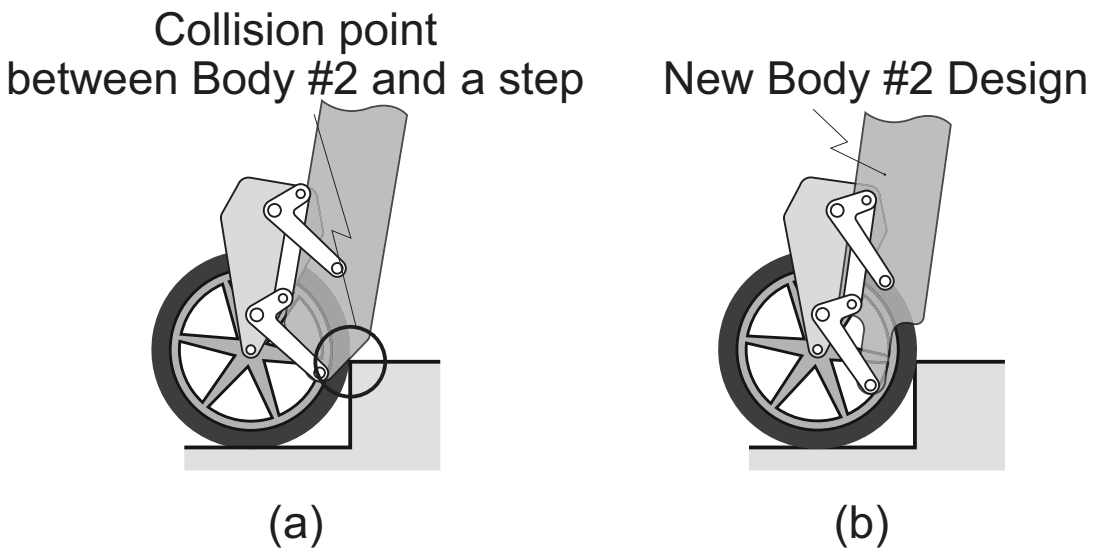


**Figure 3.28: The single-wheeled robot problem when climbing stairs with a high step's rise and the future body #2 design to overcome the problem.**

## 3.8 Concluding Remarks

In this chapter, a single-wheeled inverted pendulum robot capable of climbing stairs was developed. The design and control method of the robot is described in this paper. The experimental results demonstrate that the robot is capable of climbing stairs with a riser height of 12–13 cm and the climbing rate of each step varied from approximately 2 to 3 s. Although two controllers separately control the pitch and roll motion, the experimental results indicate that the robot could climb the stairs without losing its balance. The prototype robot currently cannot climb a staircase with a riser height of more than 13 cm. This problem occurs because the shape of body #2 is wide, and thus body #2 can collide with the corner of a step, as illustrated in Figure 3.28(a). To cope with this problem, I will redesign the shape of body #2 to ensure that it is appropriate for climbing stairs with high step-risers, such as in the example, as shown in Figure 3.28(b). Therefore, currently, the robot is applicable to traversing stairs with low step-riser heights (maximum 13 cm) and a deep step treads (39 cm). In the future, I will also consider develop a coupled control method to control pitch and roll motion to increase the performance and robustness of the robot. I have also planned to analytically determine the controller gains to increase the performance and robustness of the robot.

# Chapter 4

# Conclusion

With the vast development of robotics technology, many researchers have developed robots that can work alongside people. However, most of the developed robots cannot appropriately operate in a human environment because of their limitation in responding to objects and obstacles that commonly exist in the human environment. The robot, which is suitable to operate in a human environment, must have the following essential abilities: climbing stairs unassisted, moving through narrow passages, and reaching top of the desk or tables. There are some developed robots that are built to address the stairs and narrow passages problem such as multiped walking robots, wheel-leg robots, crawler robots, and tracked robots. However, they mostly have a short structure, and thus they cannot reach the top of the desk. To address the vertical structure, some researchers also developed humanoid robots that are built resembling the human body. They are considered ideal for working in a human environment because they can effectively traverse stairs, can move through narrow passages, and can reach the top of the desk. Despite these reasons, their design is complex and excessively expensive.

In this study, to address the problem with most of the robot in a human environment, I focused on two inverted pendulum type stair-climbing robots. These two robots have the capability to climb stairs, which is an essential ability to move in a human environment. Due to these two robots has slim and tall structures, they can move through narrow passages and can reach the top of the desk.

In the first part of this study, I concentrated on the two-wheeled stair-climbing inverted pendulum robot. The robot uses the control method based on the state-feedback

controller with a feed-forward constant. Although the control method is simple, it can be used for stabilizing the body while moving on a flat surface and achieving stair-climbing motion. The method to adjust the parameter of the controller is composed of two considerations: the motion on a flat surface and motion on a step. As the initial step, the control parameter is determined based on the linearized dynamic model of the robot on a flat surface. On the latter, the compatibility of the control parameter is verified to ensures that it satisfies the condition for climbing. By using the proposed method, the robot can achieve to climb a step. The result from the experiment indicated that the step-climbing motion completed by the robot using the proposed control method is stable. In the experiment, the robot successfully climbed four steps with the climbing rate of a single step is approximately 1.8 s.

In the second part of this study, I proposed the design of a single-wheeled inverted pendulum robot that capable of climbing stairs. The robot employed a wheel and an intermediate arm that enable the robot to climb stairs while maintaining a stable attitude. The robot uses a differential mechanism to drive the dedicated mechanism for climbing, using only a single actuator to drive the wheel and the intermediate arm. With this mechanism, the robot can self-distribute the torque, both on the wheel and intermediate arm depends on the topography of the ground. Thus, the robot can automatically move the intermediate arm when climbing the step without using an additional actuator and control method. The robot is equipped with the control moment gyroscope is used to control the lateral attitude of the robot. The experimental results demonstrate that the robot is capable of climbing stairs with a riser height of 12–13 cm and the climbing rate of each step varied from approximately 2 to 3 s. Although two controllers separately control the pitch and roll motion, the experimental results indicate that the robot could climb the stairs without losing its balance. In this robot, the control method for controlling the lateral and longitudinal motion is still based on trial and error, and thus the performance of the robot is still not robust. To increase the robustness of the robot, in the future, we will consider the use of different control methods.

# Bibliography

[1] Hodoshima R, Fukumura Y, Amano H, et al. Development of track-changeable quadruped walking robot TITAN X: Design of leg driving mechanism and basic experiment. In: Proceedings of the IEEE/RSJ 2010 International Conference of intelligent robot and systems; Taipei, Taiwan; 2010. p. 3340-3345.

[2] Hirose S, Fukuda Y, Yoneda K, et al. Quadruped walking robots at tokyo institute of technology. IEEE Robot. Automat. Mag. 2009;16(2):104-114.

[3] Semini C, Barasuol V, Goldsmith J, et al. Design of the hydraulically actuated, torque-controlled quadruped robot HyQ2Max. IEEE/ASME Trans. Mech. 2017;22(2):635-646.

[4] Zhong G, Chen L, Deng H. A performance oriented novel design of hexapod robots. IEEE/ASME Trans. Mech. 2017;22(3):1435-1443.

[5] Chen SC, Huang KJ, Li CH, et al. Trajectory planning for stair climbing in the leg-wheel hybrid mobile robot quattroped. In: Proceedings of the IEEE 2011 International Conference on Robotics and Automation; Shanghai, China; 2011. p. 1229-1234.

[6] Chen SC, Huang KJ , Chen WH, et al. Quattroped: a leg-wheel transformable robot. IEEE/ASME Trans. Mech. 2014;19(2):730-742.

[7] Moore EZ, Campbell D, Grimminger F, et al. Reliable stair climbing in the simple hexapod ‘RHex,’. In: Proceedings of IEEE 2002 International Conference on Robotics and Automation; Washington DC, USA; 2002. p. 2222-2227.

[8] Herbert SD, Drenner A, Papanikolopoulos N, Loper: a quadruped-hybrid stair climbing robot, In: Proceedings of IEEE 2008 International Conference on Robotics and Automation; Pasadena, California, USA; 2008 p. 799-804.

[9] Arai M, Tanaka Y, Hirose S, et al. Development of ‘Souryu-IV’ and ‘Souryu-V’: serially connected crawler vehicles for in-rubble searching operations. J. F. Robot. 2008;25(1-2):31-65

[10] Morozovsky N, Bewley T. Stair climbing via successive perching. IEEE/ASME Trans. Mech. 2015;20(6):2973-2982.

[11] Li N, Ma S, Li B, et al. An online stair-climbing control method for a transformable tracked robot. In: Proceedings of IEEE 2012 International Conference on Robotics and Automation; St. Paul, MN, USA; 2012. p. 923-929.

[12] Stoeter SA, Papanikolopoulos N. Autonomous stair-climbing with miniature jumping robots. IEEE Trans. Syst. Man, Cybern. Part B Cybern. 2015;35(2):313-325.

[13] Kikuchi K, Sakaguchi K, Sudo T, et al. A study on a wheel-based stair-climbing robot with a hopping mechanism. Mech. Syst. Signal Process. 2008;22(6):1316-1326.

[14] Kashki M, Zoghzoghy J, Hurmuzlu Y. Adaptive control of inertially actuated bouncing robot. IEEE/ASME Trans. Mech. 2017;22(5):2196-2207.

[15] Choi, H.D., Woo, C.K., Kim, S. et al. Independent traction for uneven terrain using stick-slip phenomenon: application to stair climbing robot Auton. Robot. 2007;23: 3-18

[16] Sun Y, Yang Y, Ma S et al. Modeling paddle-aided stair-climbing for a mobile robot based on eccentric paddle mechanism. In: Proceedings of IEEE 2015 International Conference on Robotics and Automation; Seattle, Washington, USA; 2015. p. 4153-4158.

[17] Turlapati SH, Shah M, Teja SP, et al. Stair climbing using a compliant modular robot. In: Proceedings of IEEE 2015 International Conference on Robotics and Automation; Seattle, Washington, USA; 2015. p. 3332-3339.

[18] Michel P, Chestnutt J, Kagami S, et al. GPU-accelerated real-time 3D tracking for humanoid locomotion and stair climbing. In: Proceedings of the IEEE/RSJ 2007 International Conference of intelligent robot and systems; San Diego, CA, USA; 2007. p. 463-469.

[19] Hirukawa H, Kajita S, Kanehiro F, et al. The human-size humanoid robot that can walk, lie down and get up. Int. J. Robot. Research. 2005;24(9):755-769.

[20] Aoyama T, Sekiyama K, Hasegawa Y, et al. PDAC-based 3-D biped walking adapted to rough terrain environment. J. Robot. Mech. 2012;24(1):37-46.

[21] Tonneau S, Del Prete A, Pettré J, et al. An Efficient acyclic contact planner for multiped robots. IEEE Trans. Robot. 2018;34(3): 586-601.

[22] Atkeson CG, Babu BPW, Banerjee N, et al. No falls no resets: Reliable humanoid behavior in the DARPA robotics challenge. In: Proceedings of 2015 IEEE-RAS International Conference on Humanoid Robots; Madrid, Spain; 2015. p. 623-630.

[23] Brandao M, Hashimoto K, Santos-Victor J, et al. Foot-step planning for slippery and slanted terrain using human-inspired models. IEEE Trans. Robot. 2016;32(4):868-879.

[24] Siciliano B, Khatib O. Handbook of Robotics. 1st ed. New York (NY); Springer-Verlag Berlin Heidelberg; 2008

[25] Roxo delivery robot. Available from: https://www.fedex.com/en-us/innovation/roxo-delivery-robot.html

[26] iBot wheelchair. Available from: https://mobiusmobility.com

[27] Li J, Gao X, Huang Q, et al. Mechanical design and dynamic modeling of a two-wheeled inverted pendulum mobile robot. In: Proceedings of IEEE 2007 International Conference on Automation and Logistics; Jinan, China; 2007. p. 1614-1619.

[28] Jeong, S, Takahashi T. Wheeled inverted pendulum type assistant robot: Design concept and mobile control. Intel. Serv. Robot. 2008;1(4):313-320.

[29] Kim S, Kwon SJ. Nonlinear optimal control design for underactuated two-wheeled inverted pendulum mobile platform. IEEE/ASME Trans. Mech. 2017;22(5):2803-2808.

[30] Kim Y, Kim SH, Kwak YK, Dynamic analysis of a nonholonomic two-wheeled inverted pendulum robot. J. Intel. Robot. Syst. Theory Applicat. 2005;44(1):25-46.

[31] Segway. Available from: http://www.segway.com

[32] Schoowinkel A. Design and test of a computer-stabilized unicycle [dissertation]. Stanford: Stanford University; 1987.

[33] Okumura J, Takei T, Tsubouchi T. Navigation in indoor environment by an autonomous unicycle robot with wide-type wheel. In: Proceedings of 2010 IEEE/RSJ International Conference of Intelligent Robot and System; Taipei, Taiwan; 2010. p. 154-159.

[34] Nagarajan U, Kim B, Hollis R. Planning in high-dimensional shape space for a single-wheeled balancing mobile robot with arms. In: Proceedings of 2012 IEEE International Conference on Robotics and Automation; St. Paul, MN, USA; 2012 p. 130-135.

[35] Han SI, Lee JM. Balancing and velocity control of unicycle robot based on the dynamic model. IEEE Trans. Ind. Electron. 2015;62(1);405-413.

[36] Jin H, Zhao J, Fan J, et al. Gain-scheduling control of a 6-DOF single-wheeled pendulum robot based on DIT parameterization. In: Proceedings of 2011 IEEE

International Conference on Robotics and Automation; Shanghai, China; 2011 p. 3511-3516.

[37] Jin H, Hwang J, Lee J. A balancing control strategy for a one-wheel pendulum robot based on dynamic model decomposition: Simulations and experiments. IEEE/ASME Trans. Mech. 2011;16(4);763-768.

[38] Rizal Y, Ke CT, Ho MT. Point-to-point motion control of a unicycle robot: Design implementation and validation. In: Proceedings of 2015 IEEE International Conference on Robotics and Automation; Seattle, Washington DC, USA; 2015 p. 4379-4384.

[39] Zhu Y, Gao Y, Xu C, et al. Adaptive control of a gyroscopically stabilized pendulum and its application to a single-wheel pendulum robot IEEE/ASME Trans. Mech. 2015;20(5);2095-2106.

[40] Au K, Xu Y. Decoupled dynamics and stabilization of single wheel robot. In: Proceedings of 1999 IEEE/RSJ International Conference of Intelligent Robot and System; Kyongju, Korea; 1999 p. 197-203.

[41] Jin H, Wang T, Yu F, et.al. Unicycle robot stabilized by the effect of gyroscopic precession and its control realization based on centrifugal force compensation. IEEE/ASME Trans. Mech. 2016;21(6);2737-2745.

[42] Au K, Xu Y. Stabilization and path following of a single wheel robot. IEEE/ASME Trans. Mech. 2004;9(2);407-419.

[43] Park J, Jung S. Development and control of a single-wheel robot: practical mechatronics approach. Mechatronics. 2013;23(6);594-606.

[44] Chen T, Hazelwood P, Stol KA. Step ascent modeling of a two-wheeled robot. In: Proceedings of 2012 19th International Conference on Mechatronics and Machine Vision in Practice (M2VIP); Auckland, New Zealand; 2012. p. 310-315.

[45] Strah B, Rinderknecht S. Autonomous stair climbing of a wheeled double inverted pendulum. In: Proceedings of 2013 6th IFAC Symposium on Mechatronic Systems; Hangzhou, China; 2013. p. 670-677.

[46] Luo RC, Hsiao M, Liu CW. Descending stairs locomotion and somatosensory control for an erect wheel-legged service robot. In: Proceedings of 2014 IEEE International Conference on Robotics and Automation; Hongkong, China; 2014 p. 6356-6361.

[47] Luo RC, Hsiao M, Lin TW. Erect wheel-legged stair climbing robot for indoor service applications. In: Proceedings of 2013 IEEE International Conference on Robotics and Automation; Karlsruhe, Germany; 2013. p. 2731-2736

[48] Yang D, Bewley T. A minimalist stair climbing robot (SCR) formed as a leg balancing & climbing Mobile Inverted Pendulum (MIP). In: Proceedings of 2018 IEEE/RSJ International Conference of Intelligent Robot and System; Madrid, Spain; 2018 p. 2464-2469.

[49] Matsumoto O, Kajita S, Komoriya K. Flexible locomotion control of a self-contained biped leg-wheeled system. In: Proceedings of 2002 IEEE/RSJ International Conference on Intelligent Robots and Systems; Lausanne, Switzerland; 2002 p. 2599-2604.

[50] Bannwarth JXJ, Munster C, Stol KA. Step ascension of a two-wheeled robot using feedback linearisation. In: Proceedings of 6th International Conference on Automation, Robotics and Application; Queenstown, New Zealand; 2015. p. 161-166.

[51] Tomokuni N, Shino M. Wheeled inverted-pendulum-type personal mobility robot with collaborative control of seat slider and leg wheels. In: Proceedings of 2012 IEEE/RSJ International Conference on Intelligent Robots and Systems; Vilamoura, Algerve, Portugal; 2012 p. 5367-5372.

[52] Handle. Available from: http://www.bostondynamics.com/handle

[53] Takaki T, Aoyama T, Ishii I. Development of inverted pendulum robot capable of climbing stairs using planetary wheel mechanism. In: Proceedings of 2013 IEEE International Conference on Robotics and Automation; Karlsruhe, Germany; 2013. p. 5598-5604.

[54] Karl JA, Richard MM. Feedback Systems: An Introduction for Scientist and Engineer. Princeton (NJ): Princeton University Press; 2008.

[55] Goswami A, Espiau B, Keramane A. Limit cycles in a passive compass gait biped and passivity-mimicking control laws. Auton. Robot, 1997;4:273-286.

[56] Spong MW, Block D. The Pendubot: A mechatronic system for control research and education. In: Proceedings of 1995 34th IEEE Conference on Decision and Control; New Orleans, LA, USA; 1995 p. 555-557.

[57] IFToMM, Standardization of terminology. in IFToMM Dictionaries, International Federation for the Promotion of Mechanism and Machine Science, 2007.

[58] Harmonic Drive. Available from: http://www.harmonicdrive.net

[59] Thomas G, Vantsevich VV. Wheel-terrain-obstacle interaction in vehicle mobility analysis. Vehicle Syst. Dyn, 2010;48(1);139-156.

[60] Wardana AA, Takaki T, Aoyama T, et al. Dynamic modelling and step-climbing analysis of a two-wheeled stair-climbing inverted pendulum robot. Adv. Robot. 2020;34(5);313-327.

# Acknowledgement

Firstly, I would like to express my sincere gratitude towards my advisor, Prof. Takeshi Takaki, for providing me an opportunity to pursue the doctoral degree in Robotics Laboratory, Hiroshima University and led me into academic research during past six years. He has introduced me brand new experiences in the robotics field that I have not experienced in my life. His advice, direction, encouragement and continuous support have been an excellent guidance for me during my doctoral research.

I would like to acknowledge, Prof. Idaku Ishii and Assist. Prof. Mingjun Jiang who provided me precious support during my doctoral research in the robotics laboratory. Their invaluable support, suggestion, discussion, and comment have helped me in all the time of doctoral research. I would also like to express my sincere gratitude to Ms. Yukari Kaneyuki and Ms. Michiko Kanzaki (educational administrator), and Ms. Rumi Horiuchi and Ms. Arisa Tomura in Robotics Laboratory, who helped the author in many ways during my doctoral study.

I would also like to express my sincere thanks to the bachelor, master and doctoral students in Robotics Laboratory for their friendly discussion and help in both life and my research.

Finally, I would like to express my deepest gratitude to my family, who have encouraged me throughout my doctoral research even in hard times. Without their encouragement, I could never have reached this point.

July, 2020

Ananta Adhi Wardana